International Hydrological Programme

Guide to Remote Sensing

— The Textbook for the Eighth IHP Training Course in 1999 —

Editor: Kenji Nakamura

Institute for Hydrospheric-Atmospheric Sciences, Nagoya University

United Nations Educational Scientific and Cultural Organization

Prepared for the 8th IHP Training Course on Remote Sensing,
8-21 March 1999, Nagoya, Tokyo and Chiba, Japan

Working Group, IHP Training Course,
Sub-Committee for IHP,
Japan National Commission for UNESCO

Chairperson:	Hiroshi Tanaka
Secretary:	Masayoshi Nakawo
Members:	T. Takeuchi, K. Matsui, Y. Shimamura, S. Kishi, K. Yokoyama, T. Koike, T. Kozu, H. Shimoda, Y. Honda, M. Nakamura, M. Sakamoto, T. Okino, Y. Fukushima, K. Nakamura, and H. Terai

Published in March 1999
by the Institute for Hydrospheric-Atmospheric Sciences, Nagoya University and United Nations Educational Scientific and Cultural Organization

Cover: Toropical Rainfall Measurement Mission (TRMM) satellite and measured rain distribution in Feb. 1998. By courtesy of the National Space Development Agency of Japan (NASDA).

Preface

This training course, as one of the activities of the International Hydrological Programme (IHP), has been supported by a large number of university professors and institute researchers who are devoted to the hydrological education for young scientists and engineers from the Asia-Pacific region. Substantial efforts have been also made by those who are involved in some committees; Japan National Commission for UNESCO, Sub-committee for IHP, and Working Group for IHP Training Course. In addition, contributions from governmental organizations and institutions have been essential for the training course to be successful. Very soon in March this year we are going to undertake the eighth IHP Training Course. Last year a new trial was planned for the schedule of the training course. Firstly, we put a clearly defined study target every year for the training students, Snow Hydrology last year and Remote Sensing this year. Secondly, we established an experimental programme to allow the students to better understand the target.

For this purpose we need to edit a textbook. The textbook of this year is titled Remote Sensing and is composed of selected contents from which students can obtain introductory knowledge of remote sensing in a short period. We express our gratitude to the authors for their dedication to prepare this textbook. Especially, we must extend our appreciation to Professor Kenji Nakamura of the Institute for Hydrospheric-Atmospheric Sciences, Nagoya University, for his long-standing leadership.

12 January, 1999

Hiroshi Tanaka
Chairman of Working Group of IHP Training Course
Director of Institute for Hydrospheric-Atmospheric Sciences,
Nagoya University

Acknowledgements

I would like to take this opportunity to thank all the authors for their many contributions to this textbook. Without their efforts, this textbook would never have been published. The editing work was done with great helps from Dr. Ichiro Tamagawa, Dr. David A. short and Ms. Yoko Sawada. Thanks are extended to Prof. H. Tanaka, the Chairperson of the Working Group of the IHP Training Course and the Director of the Institute for Hydrospheric-Atmospheric Sciences, Nagoya University and Prof. M. Nakawo, the Secretary of the Working Group of the IHP Training Course. The IHP Training Course is under continuous support from the Ministry of Education, Science, Sports and Culture in Japan and special thanks will go to Mr. T. Noda, Programming Officer in the Ministry.

The typesetting was done by LaTeX on FreeBSD.

February 1999
Kenji Nakamura
Editor

Contents

Part I

Textbook

Chapter 1

Fundamentals of Remote Sensing

Yoshiaki Honda
Center for Environmental Remote Sensing, Chiba Univ.
1-33 Yayoi, Inage-ku, Chiba, 263-8522, JAPAN
Phone: +81-43-290-3835, fax: +81-43-290-3857
E-mail: yhonda@rsirc.cr.chiba-u.ac.jp

This part of the text is extracted from Remote Sensing Note which was published by Japan Association on Remote Sensing (JARS).

1.1 Concept of Remote Sensing

Remote Sensing is defined as the science and technology by which the characteristics of objects of interest can be identified, measured or analyzed the characteristics without direct contact. Electro-magnetic radiation which is reflected or emitted from an object is the usual source of remote sensing data. However any media such as gravity or magnetic fields can be utilized in remote sensing.

The technical term "remote sensing" was first used in the United States

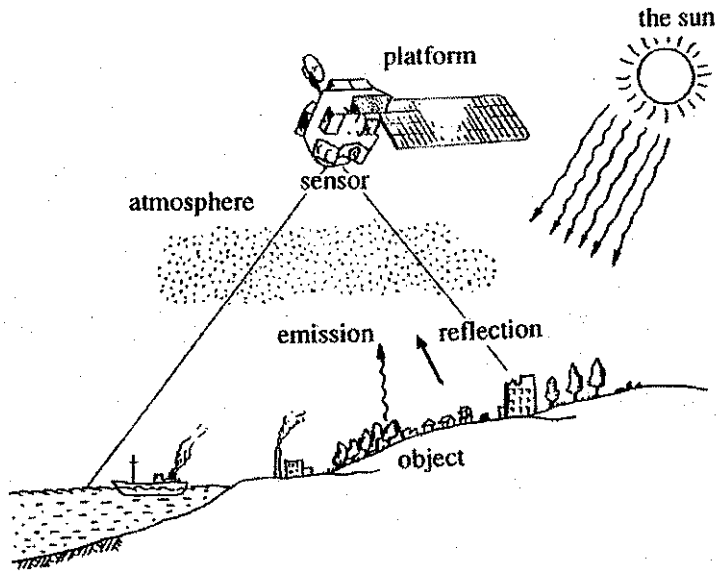

Figure 1.1: Data collection by remote sensing

in the 1960's, and encompassed photogrammetry, photo-interpretation, photo-geology etc. Since Landsat-1, the first earth observation satellite was launched in 1972, remote sensing has become widely used.

The characteristics of an object can be determined, using reflected or emitted electro-magnetic radiation, from the object. That is, "each object has a unique and different characteristics of reflection or emission if the type of object or the environmental condition is different." Remote sensing is a technology to identify and understand the object or the environmental condition through the uniqueness of the reflection or emission.

This concept is illustrated in Fig. 1.1 while Fig. 1.2 shows the flow of remote sensing, where three different objects are measured by a sensor in a limited number of bands with respect to their, electro-magnetic characteristics after various factors have affected the signal. The remote sensing data

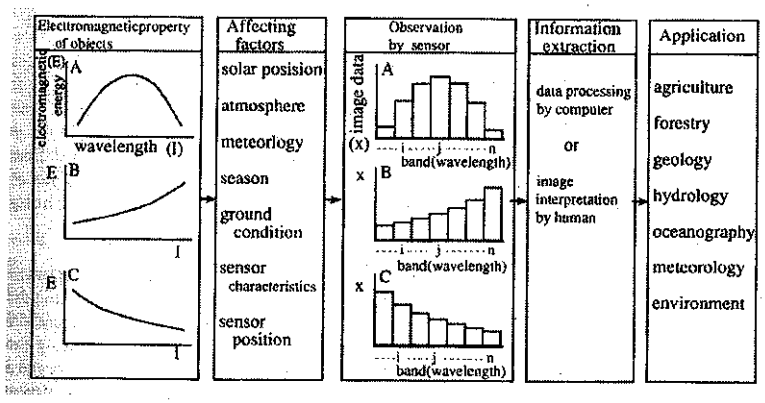

Figure 1.2: Flow of remote sensing

will be processed automatically by computer and/or manually interpreted by humans, and finally utilized in agriculture, land use, forestry, geology, hydrology, oceanography, meteorology, environment etc.

In this chapter, the principles of electro-magnetic radiation are described in sections 1.2–1.3, the types of remote sensing with respect to the spectral range of the electro-magnetic, radiation in section 1.4, the definition of radiometry in section 1.5, black body radiation in section 1.6, electro-magnetic characteristics in sections 1.7 and 1.8, solar radiation in section 1.9 and atmospheric behavior in sections 1.10 and 1.11.

1.2 Interactions between Matter and Electro-magnetic waves

All matter reflects, absorbs, penetrates and emits electro-magnetic radiation in a unique way. For example, the reason why a leaf looks green is that the chlorophyll absorbs blue and red spectra and reflects the green spectrum (see 1.8). The unique characteristics of matter are called spectral characteristics (see 1.5).

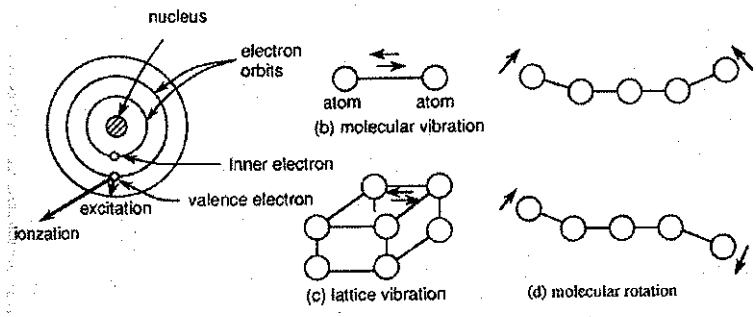

Figure 1.3: Schematics of characteristic states associated with electromagnetic radiation

All matter is composed of atoms and molecules with a particular composition. Therefore, matter will emit or absorb electro-magnetic radiation at a particular wavelength with respect to the inner state.

The types of inner state are classified into several classes, such as ionization, excitation, molecular vibration, molecular rotation etc. as shown in Fig. 1.3 and Table 1.1, which will radiate the associated electro-magnetic radiation. For example, visible light is radiated by excitation of valence electrons, while infrared is radiated by molecular vibration or lattice vibration.

1.3 Wavelength Regions of Electro-magnetic Radiation

Wavelength regions of electro-magnetic radiation have different names ranging from γ ray, Xray, ultraviolet (UV), visible light, infrared (IR) to radio wave, in order from the shorter wavelengths. The shorter the wavelength is, the more the electro-magnetic radiation is characterized as particle motion with more linearity and directivity.

Table 1.2 shows the names and wavelength region of electro-magnetic

Characteristic state	energy (eV)	associated electromagnetic wave
Nuclear transmission and disintegrations	$10^7 \sim 10^5$	γ - ray
Ionization by inner electron removal	$10^4 \sim 10^2$	X - ray
Ionization by outer electron removal	$10^2 \sim 4$	Ultra - violet
Excitation of valence electrons	$4 \sim 1$	Visible
Molecular vibration, Lattice vibration	$10 \sim 10^{-5}$	Infrared
Molecular rotations, electron spin resonance	$10^{-4} \sim 10^{-5}$	Microwave
Nuclear spin resonance	10^{-7}	Meter wave

[unit] energy of 1eV = 1.60219×10^{-19} Joule wavelength of 1eV light = 1.23985 μm

Table 1.1: Relation between characteristic state and electro magnetic radiation

class				wavelength	frequency
ultraviolet				100A ~ 0.4 μm	750 ~ 3,000THz
visible				0.4 ~ 0.7 μm	430 ~ 750THz
infrared	near infrared			0.7 ~ 1.3 μm	230 ~ 430THz
	short wave infrared			1.3 ~ 3 μm	100 ~ 230THz
	intermediate infrared			3 ~ 8 μm	38 ~ 100THz
	thermal infrared			8 ~ 14 μm	22 ~ 38THz
	far infrared			14 μm ~ 1mm	0.3 ~ 22THz
radio wave	submillimeter			0.1 ~ 1mm	0.3 ~ 3THz
	micro wave	millimeter	(EHF)	1 ~ 10mm	30 ~ 300GHz
		centimeter	(SHF)	1 ~ 10cm	3 ~ 30GHz
		decimeter	(UHF)	0.1 ~ 1m	0.3 ~ 3GHz
	very short wave		(VHF)	1 ~ 10m	30 ~ 300MHz
	short wave		(HF)	10 ~ 100m	3 ~ 30MHz
	medium wave		(MF)	0.1 ~ 1km	0.3 ~ 3MHz
	long wave		(LF)	1 ~ 10km	30 ~ 300kHz
	very long wave		(VLF)	10 ~ 100km	3 ~ 30kHz

Table 1.2: Classification of electromagnetic radiations

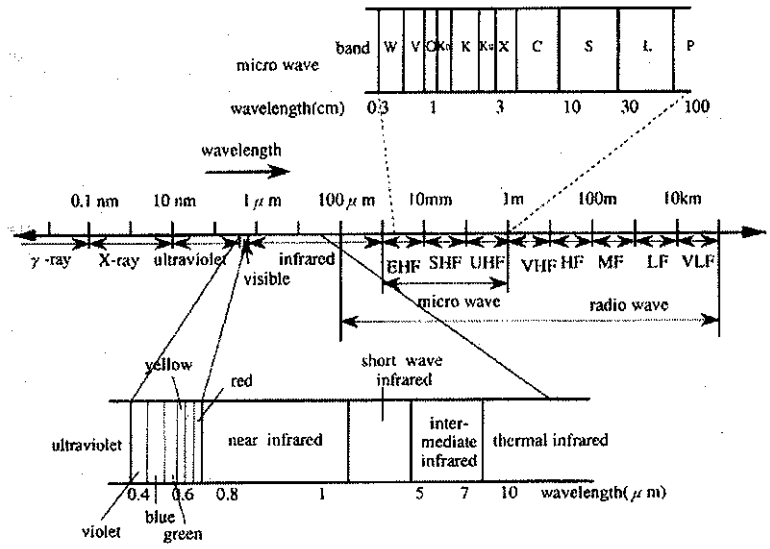

Figure 1.4: The bands used in remote sensing

radiation. One has to note that classification of infrared and radio radiation may vary according to the scientific discipline. The table shows an example which is generally used in remote sensing.

The electro-magnetic radiation regions used in remote sensing are near UV(ultra-violet) (0.3–0.4 μm), visible light(0.4–0.7 μm), near shortwave and thermal infrared (0.7–14 μm) and micro wave (1 mm–1 μm).

Figure 1.4 shows the spectral bands used in remote sensing. The spectral range of near IR and short wave infrared is sometimes called the reflective infrared (0.7 3 μm) because the range is more influenced by solar reflection rather than the emission from the ground surface (see 1.4). In the thermal infrared region, emission from the ground's surface dominates the radiant energy with little influence from solar reflection (see 1.4 and 1.6).

Visible light corresponds to the spectral colors. They are, in order from

the longer wavelengths in the visible region, the so called rainbow colors; red, orange, yellow, green, blue, indigo and violet are located with respect to the wavelength.

Short wave infrared has more recently been used for geological classification of rock types. Thermal infrared is primarily used for temperature measurement (see 1.6), while micro wave is utilized for radar and micro wave radiometry. A special naming of K band, X band, C band, L band etc. is given to the micro wave region as shown in Fig. 1.4.

1.4 Types of Remote Sensing with Respect to Wavelength

Remote sensing is classified into three types with respect to the wavelength regions; (1) Visible and Reflective Infrared Remote Sensing, (2) Thermal Infrared Remote Sensing and (3) Microwave Remote Sensing, as shown in Fig. 1.5.

The energy source used in the visible and reflective infrared remote sensing is the sun. The sun radiates electro-magnetic energy with a peak wavelength of 0.5 μm (see 1.6 and 1.9). Remote sensing data obtained in the visible and reflective infrared regions mainly depends on the reflectance of objects on the ground surface (see 1.7). Therefore, information about objects can be obtained from the spectral reflectance. However laser radar is exceptional because it does not use the solar energy but the laser energy of the sensor.

The source of radiant energy used in thermal infrared remote sensing is the object itself, because any object with a normal temperature will emit electro-magnetic radiation with a peak at about 10 μm (see 1.6), as illustrated in Fig. 1.5.

One can compare the difference of spectral radiance between the sun (a) and an object with normal earth temperature (about 300 K), as shown in Fig. 1.5. However it should be noted that the figure neglects atmospheric absorption (see 1.10), for simplification, though the spectral curve varies with respect to the reflectance, emittance and temperature of the object.

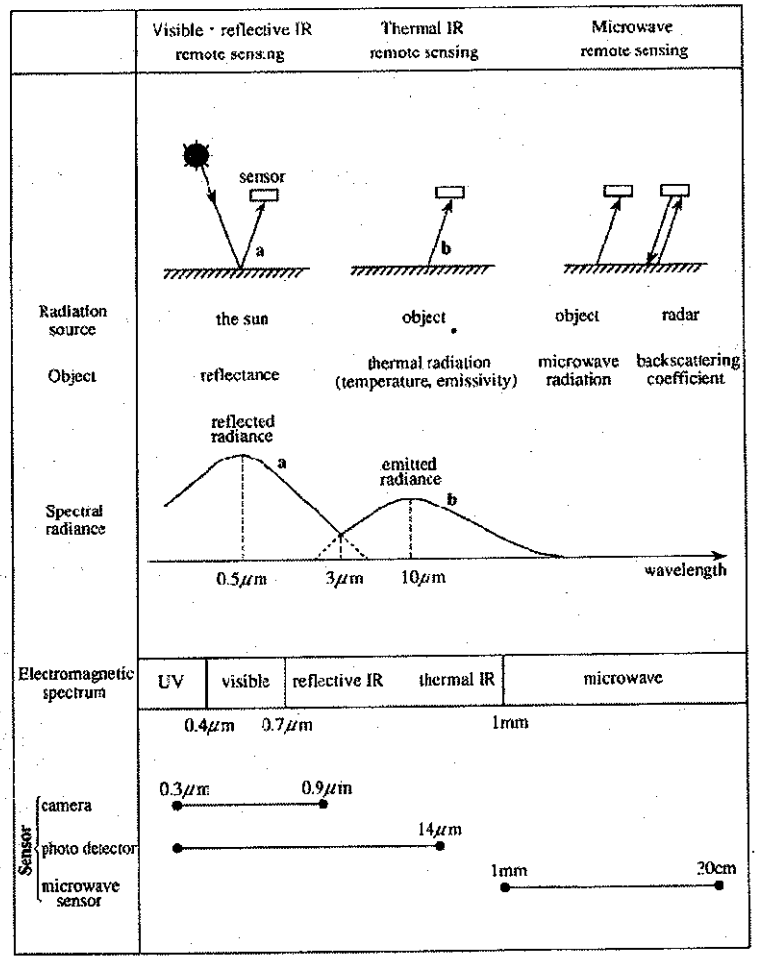

Figure 1.5: Three types of remote sensing with respect to wavelength regions

The curves of (a) and (b) cross at about 3.0 μm. Therefore in the wavelength region shorter than 3.0 μm, spectral reflectance is mainly observed, while in the region longer than 3.0 μm, thermal radiation is measured.

In the microwave region, there are two types of micro wave remote sensing, passive microwave remote sensing and active remote sensing. In passive microwave remote sensing, the microwave radiation emitted from an object is detected, while the back scattering coefficient is detected in active micro wave remote sensing.

Remarks: the two curves (a) and (b) in Fig. 1.5 show the black body's spectral radiances of the sun at a temperature of 6,000 K and an object with a temperature of 300 K, without atmospheric absorption.

1.5 Definition of Radiometry

In remote sensing, electro-magnetic energy reflected or emitted from objects is measured. The measurement is based on either radiometry or photometry, with different technical terms and physical units.

Radiometry is used for physical measurement of a wide range of radiation from x-ray to radio wave, while photometry corresponds to the human perception of visible light based on the human eye's sensitivity as shown in Fig. 1.6.

One can add an adjective "Spectral" before the technical terms of radiometry when defined as per unit of wavelength. For example, one can use spectral radiant flux ($W\mu m^{-1}$) or spectral radiance ($Wm^{-2}sr^{-1}\mu m$).

Radiant energy is defined as the energy carried by electro-magnetic radiation and expressed in the unit of joule (J).

Radiant flux is radiant energy transmitted as a radial direction per unit time and expressed in a unit of watt (W). Radiant intensity is radiant flux radiated from a point source per unit solid angle in a radiant direction and expressed in the unit of Wsr^{-1}. Irradiance is radiant flux incident upon a surface per unit area and expressed in the unit of Wm^{-2}. Radiant emittance is radiant flux radiated from a surface per unit area, and expressed in a unit of Wm^{-2}. Radiance is radiant intensity per unit projected area in a radial

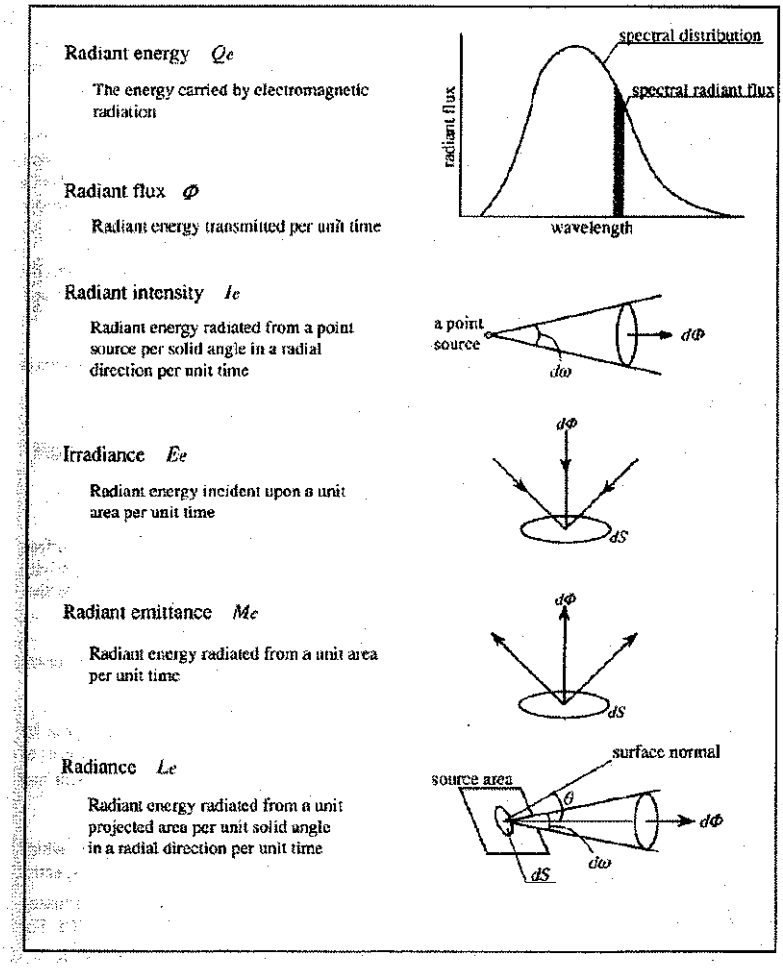

Figure 1.6: Summary of radiometric definitions

spectral radiance of black body $B\lambda$ is given as follows.

$$B\lambda = \frac{2hc^2}{\lambda^5} \cdot \frac{1}{exp(hc/k\lambda T) - 1}$$

$B\lambda$	:	black body spectral radiance ($W \cdot m^{-2} \cdot sr^{-1} \cdot \mu m^{-1}$)	
T	:	absolute temperature of Black body (K)	
λ	:	wavelength (μm)	
c	:	velocity of light	2.998×10^8 ($m \cdot s^{-1}$)
h	:	plank's constant	6.626×10^{-34} ($J \cdot s$)
k	:	Boltzmann's constant	1.380×10^{-23} ($J \cdot K^{-1}$)

Table 1.3: Plank's law of radiation

direction and expressed in the unit of $Wm^{-2}sr^{-1}$.

1.6 Black Body Radiation

An object radiates unique spectral radiant flux depending on the temperature and emissivity of the object. This radiation is called thermal radiation because it mainly depends on temperature. Thermal radiation can be expressed in terms of black body theory.

A black body is matter which absorbs all electro-magnetic energy incident upon it and does not reflect nor transmit any energy. According to Kirchhoff's law the ratio of the radiated energy from an object in thermal static equilibrium, to the absorbed energy is constant and only dependent on the wavelength and the temperature T. A black body shows the maximum radiation as compared with other matter. Therefore a black body is called a perfect radiator.

Black body radiation is defined as thermal radiation of a black body, and can be given by Plank's law as a function of temperature T and wavelength as shown in Fig. 1.7 and Table 1.3.

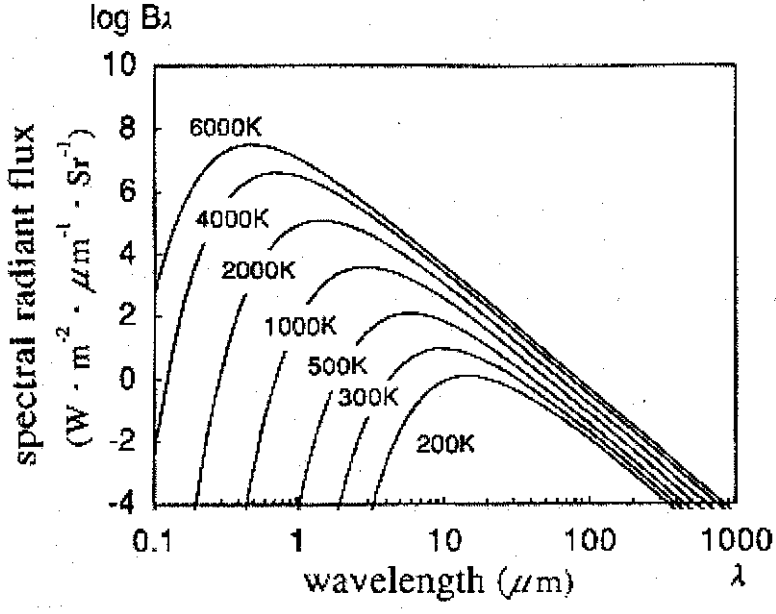

Figure 1.7: Plank's law of radiation

In remote sensing, a correction for emissivity should be made because normal observed objects are not black bodies. Emissivity can be defined by the following formula:

$$\text{Emissivity} = \frac{\text{Radiant energy of an object}}{\begin{array}{l}\text{Radiant energy of a black body}\\ \text{with the same temperature as the object}\end{array}} \tag{1.1}$$

Emissivity ranges between 0 and 1 depending on the dielectric constant of the object, surface roughness, temperature, wavelength, look angle etc. Figure 1.8 shows the spectral emissivity and spectral radiant flux for three objects that are a black body, a gray body and a selective radiator.

The temperature of the black body which radiates the same radiant energy as an observed object is called the brightness temperature of the object.

Stefan-Boltzmann's law is obtained by integrating the spectral radiance given by Plank's law, and shows in that the radiant emittance is proportional to the fourth power of absolute temperature (T^4). This makes the radiant energy very sensitive to temperature.

Wien's displacement law is obtained by differentiating the spectral radiance, which shows that the product of wavelength (corresponding to the maximum peak of spectral radiance) and temperature, is approximately 3,000 (μmK). This law is useful for determining the optimum wavelength for temperature measurement of objects with a temperature of T. For example, about 10 μm is the best for measurement of objects with a temperature of 300 K.

1.7 Reflectance

Reflectance is defined as the ratio of incident flux on a sample surface to reflected flux from the surface as shown in Fig. 1.9. Reflectance ranges from 0 to 1. Reflectance was originally defined as a ratio of incident flux of white light to reflected flux in a hemisphere direction. Equipment to measure reflectance are called spectrometers (see 5.3).

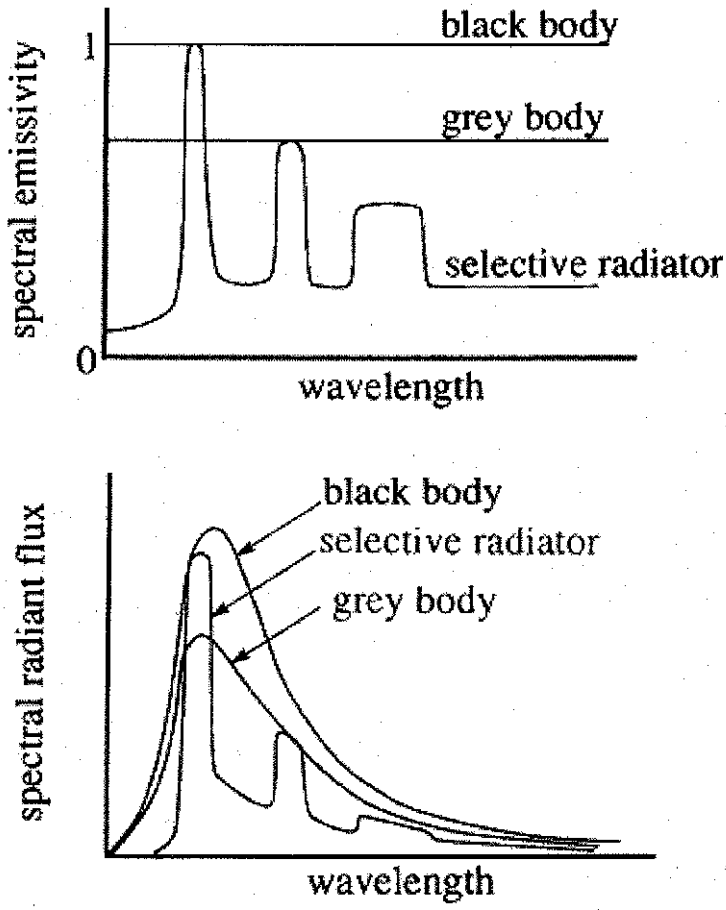

Figure 1.8: Radiators

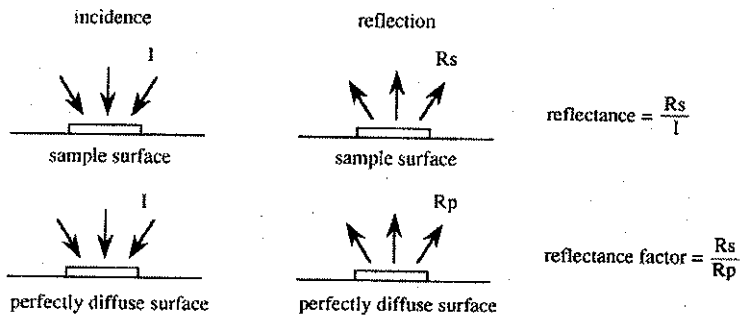

Figure 1.9: Reflectance and reflectance factor

Albedo is defined as the reflectance using the incident light source from the sun. Reflectance factor is sometime used as the ratio of reflected flux from a sample surface to reflected flux from a perfectly diffuse surface.

Reflectance with respect to wavelength is called spectral reflectance as shown for a vegetation example in Fig. 1.10. A basic assumption in remote sensing is that spectral reflectance is unique and different from one object to an unlike object.

Reflectance with a specified incident and reflected direction of electromagnetic radiation or light is called directional reflectance. The two directions of incident and reflection have can be directional, conical or hemispherical making nine possible combinations.

For example, if incident and reflection are both directional, such reflectance is called bidirectional reflectance as shown in Fig. 1.11. The concept of bidirectional reflectance is used in the design of sensors.

Remarks: A perfectly diffuse surface is defined as a uniformly diffuse surface with a reflectance of 1, while the uniformly diffused surface, called a Lambertian surface, reflects a constant radiance regardless of look angle.

The Lambert cosine law which defines a Lambertian surface is as follows:

$$I(\theta) = I_n \cos\theta \tag{1.2}$$

where

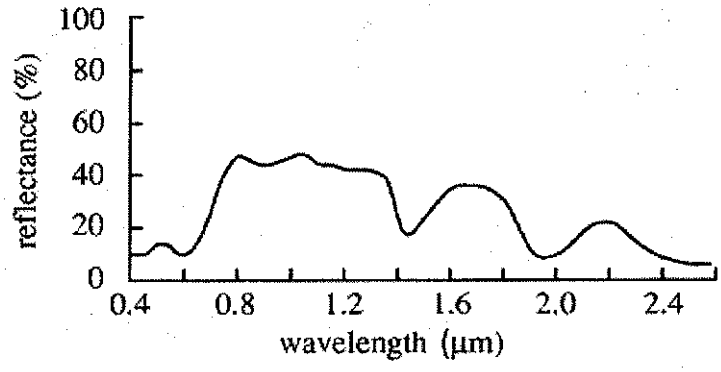

Figure 1.10: Spectral reflectance of vegetation

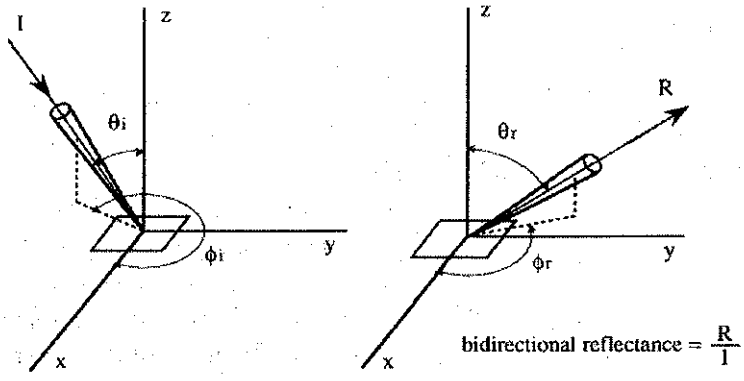

Figure 1.11: Bidirectional reflectance

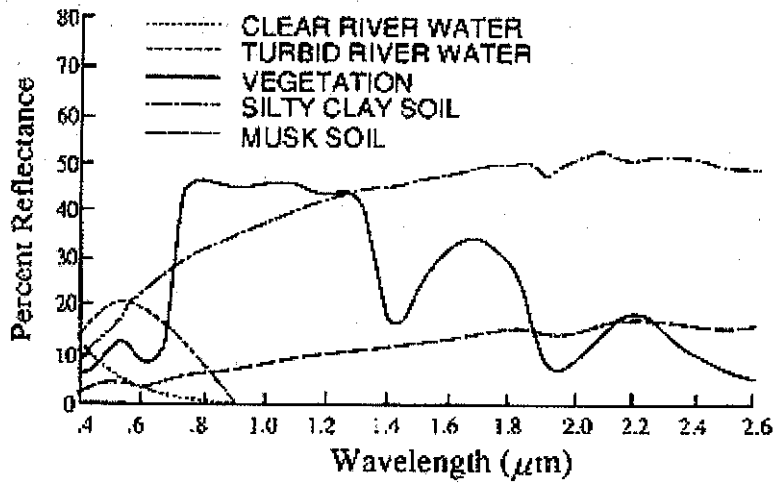

Figure 1.12: Spectral reflectance of vegitation, soil and water

$I(\theta)$: luminous intensity at an angle of θ from the normal to the surface
I_n : luminous intensity at the normal angle

1.8 Spectral Reflectance of Land Covers

Spectral reflectance is assumed to be different with respect to the type of land cover, as explained in 1.3 and 1.8. This is the principle that in many cases allows the identification of land covers with remote sensing by observing the spectral reflectance or spectral radiance from a distance far removed from the surface.

Vegetation has a very high reflectance in the near infrared region, though there are three low minima due to absorption. Soil has rather higher values for almost all spectral regions. Water has almost no reflectance in the infrared region. Chlorophyll, contained in a leaf, has strong absorption at 0.45 μm and 0.67 μm, and high reflectance at near infrared (0.7–0.9 μm). This results in a small peak at 0.5–0.6 (green color band), which makes veg-

etation green to the human observer. Near infrared is very useful for vegetation surveys and mapping because such a steep gradient at 0.7–0.9 μm is produced only by vegetation. Because of the water content in a leaf, there are two absorption bands at about 1.5 μm and 1.9 μm. This is also used for surveying vegetation vigor.

Figure 1.13 shows various patterns of spectral reflectance with respect to different rock types in the short wave infrared (1.3–3.0 μm). In order to classify such rock types with different narrow bands of absorption, a multiband sensor with a narrow wavelength interval is to be developed. Imaging spectrometers have been developed for rock type classification and ocean color mapping.

1.9 Spectral Characteristics of Solar Radiation

The sun is the energy source used to detect reflective energy of ground surfaces in the visible and near infrared regions. Sunlight will be absorbed and scattered by ozone, dust, aerosols, etc., during the transmission from outer space to the earths surface. Therefore, one has to study the basic characteristics of solar radiation.

The sun constant that is obtained by integrating the spectral irradiance for all wavelength regions is normally taken as 1.37 Wm^{-2}. Figure 1.14 shows four observation records of solar spectral irradiance. The values of the curves correspond to the value at the surface perpendicular to the normal direction of the sun light. To convert to the spectral irradiance per m^2 on the Earth surface with a latitude of ϕ, multiply the following coefficient by the observed values in Fig. 1.14.

$$\alpha = (L_0/L)^2 \cos z \cos z = \sin\phi \sin\delta + \cos\phi \cos\delta \cos h \qquad (1.3)$$

where

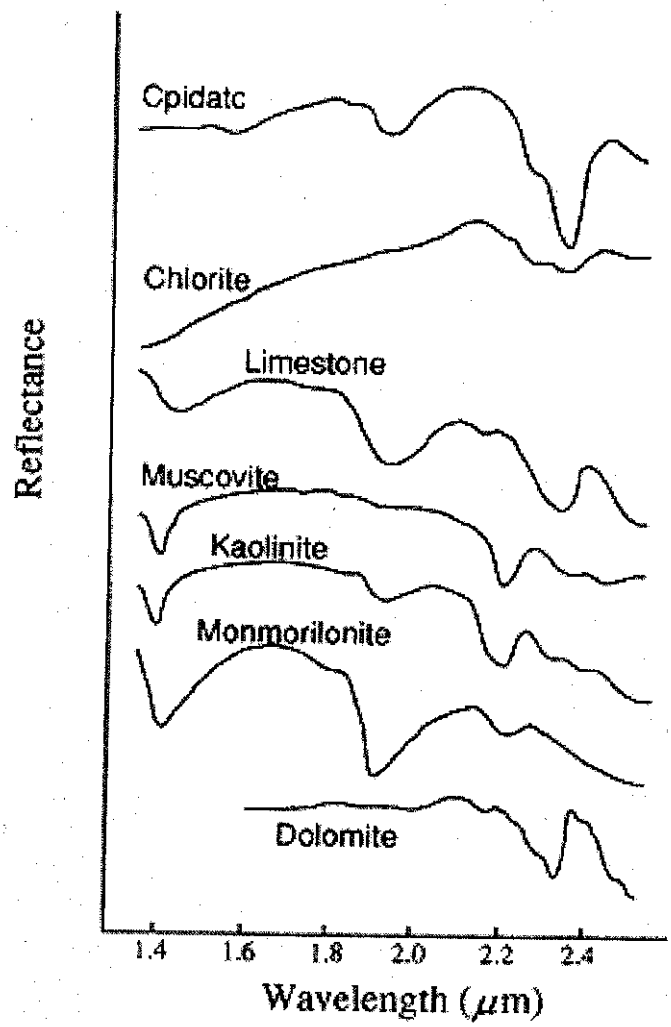

Figure 1.13: Spectral reflectance of rocks and minerals

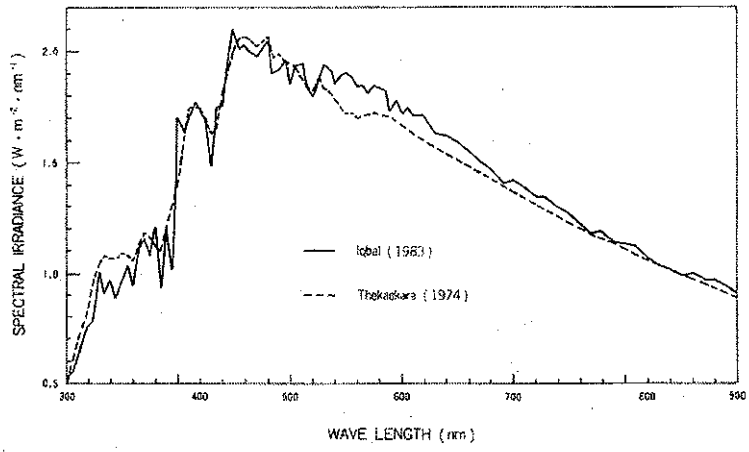

Figure 1.14: Solar irradiance at the top of atmosphere (annual mean)

z : solar zenith angle
δ : declination
h : hour angle
L : real distance between the sun and the earth
L_0: average distance between the sun and the earth

The incident solar radiation at the earth's surface is very different to that at the top of the atmosphere due to atmospheric effects, as shown in Fig. 1.15, which compares the solar spectral irradiance at the earth's surface to black body irradiance from a surface of temperature 5900 K.

The solar spectral irradiance at the earth's surface is influenced by the atmospheric conditions and the zenith angle of the sun. Beside the direct sunlight falling on a surface, there is another light source called sky radiation, diffuse radiation or skylight, which is produced by the scattering of the sunlight by atmospheric molecules and aerosols.

The skylight is about 10 percent of the direct sunlight when the sky is clear and the sun's elevation angle is about 50 degrees. The skylight has a

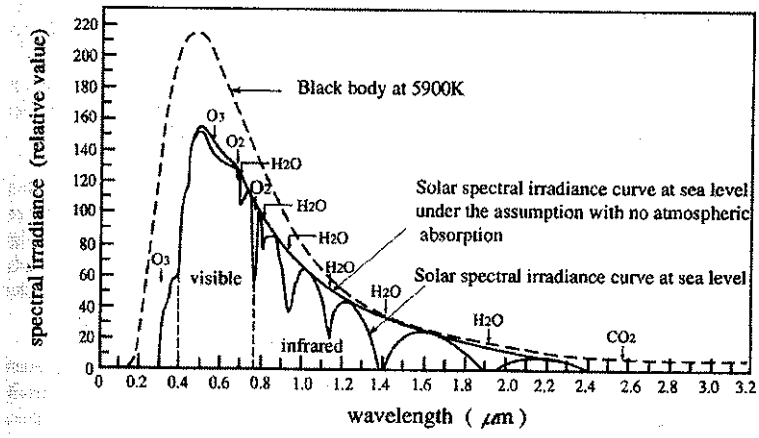

Figure 1.15: Comparison of spectral irradiance of solar light at sea level woth black body radiation

peak in its spectral characteristic curve at a wavelength of 0.45 μm.

1.10 Transmittance of the Atmosphere

The sunlight's transmission through the atmosphere is affected by absorption and scattering of atmospheric molecules and aerosols. The reduction of sunlight intensity is called extinction. The rate of extinction is expressed as extinction coefficient (see 1.11). The optical thickness of the atmosphere corresponds to the integrated value of the extinction coefficient at each altitude by the atmospheric thickness. The optical thickness indicates the magnitude of absorption and scattering of the sunlight. The following elements will influence the transmittance of the atmosphere.

a. **Atmospheric molecules (smaller size than wavelength):** carbon dioxide, ozone, nitrogen gas, and other molecules

b. **Aerosols (larger size than wavelength):** water drops such as fog

and haze, smog, dust and other particles with a bigger size

Scattering by atmospheric molecules with a smaller size than the wavelength of the sunlight is called Raleigh scattering. Raleigh scattering is inversely proportional to the fourth power of the wavelength. The contribution of atmospheric molecules to the optical thickness is almost constant spatially and with time, although it varies somewhat depending on the season and the latitude.

Scattering by aerosols with larger size than the wavelength of the sunlight is called Mie scattering. The source of aerosols is suspended particles such as sea water or dust in the atmosphere blown from the sea or the ground, urban garbage, industrial smoke, volcanic ashes etc., which varies to a great extent depending upon the location and the time. In addition, the optical characteristics and the size distribution also chang with respect to humidity, temperature and other environmental conditions. This makes it difficult to measure the effect of aerosol scattering.

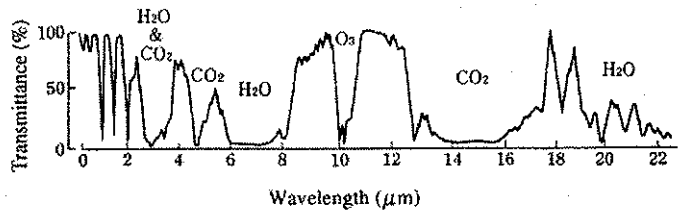

Figure 1.16: Characteristic of atmospheric spectral transmittance

Scattering, absorption and transmittance of the atmosphere are different for different wavelengths. Fig. 1.16 shows the spectral transmittance of the atmosphere. The low parts of the curve show the effect of absorption by the molecules described in the figure. Figure 1.17 shows the spectral transmittance, or conversely absorption, with respect to various atmospheric molecules. The open region with higher transmittance called an "atmospheric window".

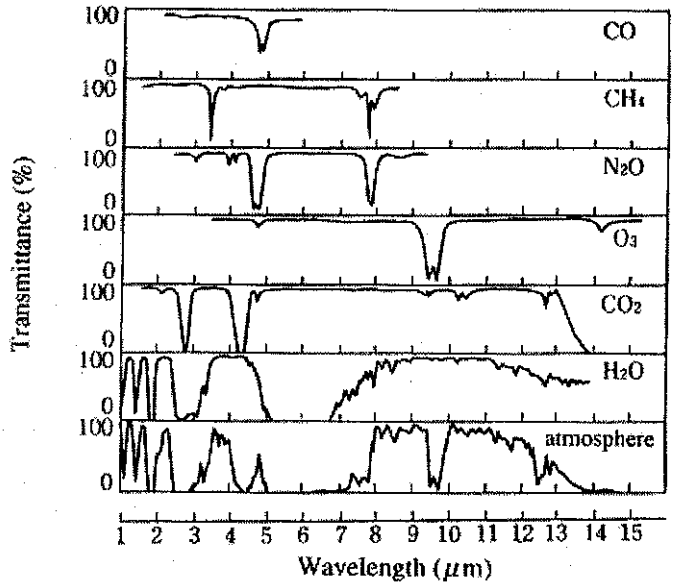

Figure 1.17: Characteristic of absorption in infrared region by atmospheric molecules

As the transmittance partially includes the effect of scattering, the contribution of scattering is larger in the shorter wavelengths. Figure 1.18 shows a result of simulation for resultant transmittance multiplied by absorption and scattering which would be produced for a standard "clean atmospheric model" in the U.S.A. The contribution by scattering is dominant in the region less than 2 mm and proportional to the wavelength in shoter wavelength. The contribution by absorption is not constant but depends on the specific wavelength.

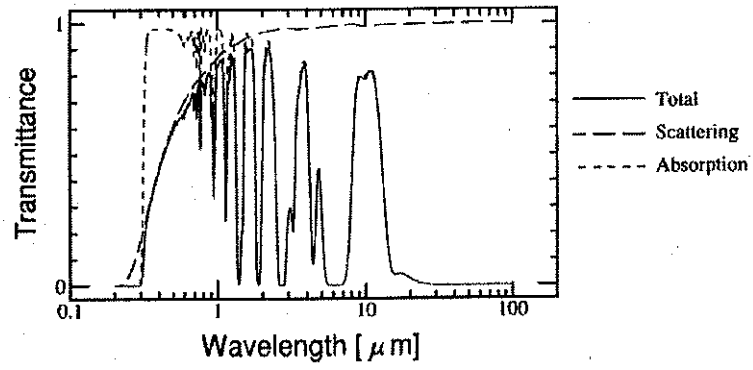

Figure 1.18: Atmospheric transmittance with contributions of absorption and scattering for "Clean" U.S. standard atmospheric model

1.11 Radiative Transfer Equation

Radiative transfer is defined as the process of transmission of the electromagnetic radiation through the atmosphere, and the influence of the atmosphere. The atmospheric effect is classified into multiplicative effects and additive effects as shown in Table 1.4.

The multiplicative effect comes from the extinction by which incident energy from the earth to a sensor will reduce due to the influence of absorption and scattering. The additive effect comes from the emission produced by thermal radiation from the atmosphere and atmospheric scattering, which is incident energy on a sensor from sources other than the object being measured. Absorption will occur at specific wavelengths (see 1.10) when the electro-magnetic energy converts to thermal energy. On the other hand, scattering is remarkable in the shorter wavelength region when energy conversion does not occur but only the direction of the path changes.

Additional energy by emission and scattering of the atmosphere is incident upon a sensor. The thermal radiation of the atmosphere which is characterized by Plank's law (see 1.6), is uniform in all directions. The

Effects	Mechanism	Wavelength	Related physical variables
Multiplitive	Absorption	All region	Absorption coefficient, Absorber amount, Temperature Pressure
(Extinction)	Scattering	Visible & near IR	Scattering coefficient, Scatterer amount, Phase function
Additive	Thermal radiation	Thermal IR	Absorption coefficient, Absorber amount, Temperature Pressure
(Emission)	Scattering	Visible & near IR	Scattering coefficient, Scatterer amount, Phase function

Table 1.4: Atmospheric effects

emission and scattering of the atmosphere incident on the sensor, is indirectly input from other energy sources of scattering than those on the path between a sensor and an object.

Generally, as extinction and emission occur at the same time, both effects should be considered together in the radiative transfer equation as indicated in the formula in Table 1.5.

Definition of extinction coefficient K

$$\mathbf{dI} = \rho \cdot \mathbf{K} \cdot \mathbf{I} \cdot \mathbf{ds}$$

I : Incident radiance
dI : Increment of radiance
ρ : Absorber / Scatterer density
ds : Path length

Definition of emission coefficient j

$$\mathbf{dI} = \rho \cdot \mathbf{j} \cdot \mathbf{ds}$$

(1) Thermal radiation

$$\mathbf{j} = \rho \cdot \mathbf{B(T)}$$

ρ : Absorber density
B : Planck function
T : Temperature [K]

(2) Scattering

$$\mathbf{j} = \omega_0 \frac{\mathbf{K}}{4\pi} \rho \int_{\Omega} \mathbf{P}(\Omega, \Omega)\, \mathbf{I}\,(\Omega')\, d\Omega$$

ω_0 : Albedo for single scattering
ρ : Scatterer density
P : Phase function
Ω : Solid angle of incidence
Ω' : Solid angle of scattering
K : Extinction coefficient

Table 1.5: Radiative transfer equation

Chapter 2

Utilization of Remote Sensing for Atmospheric Sciences

Kenji Nakamura
Institute for Hydrospheric-Atmospheric Sciences, Nagoya University
Furocho, Chikusa-ku, Nagoya 464-8601, Japan
Phone: +81-52-789-5439, fax: +81-789-3436
E-mail: nakamura@ihas.nagoya-u.ac.jp

2.1 Introduction

Recently, environmental problems have attracted attention. Spatial scales of the problems range from very local to global. Environmental problems have close connections to atmospheric phenomena and phenomena in the atmosphere have very rapid variations with three-dimensional distributions. For the atmospheric sciences, remote sensing is very useful and essential because of its ability to observe a big volume of the atmosphere in a quasi-continuous manner.

Remote sensing techniques may be divided into two categories: one is

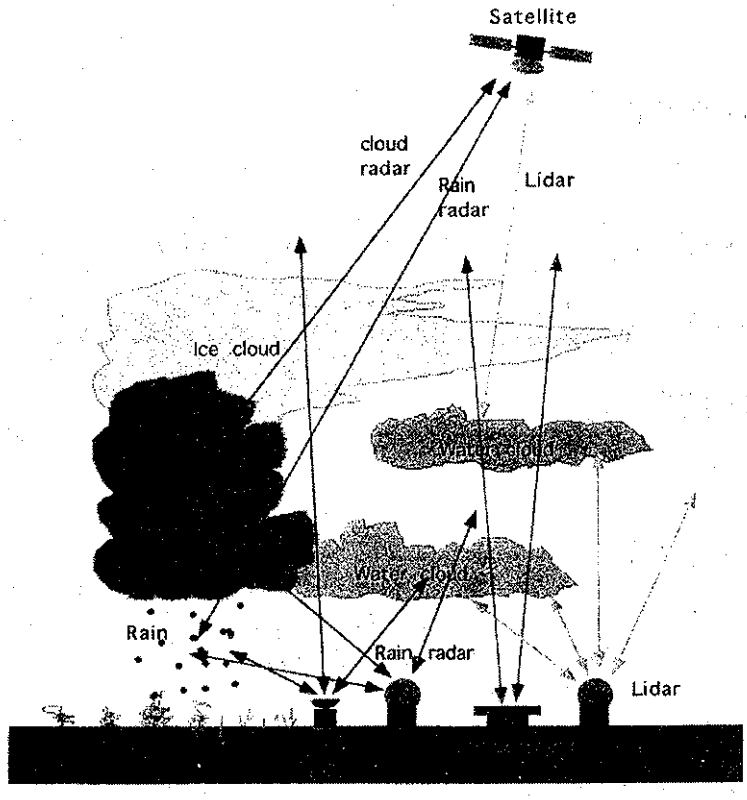

Rain radar: rain area
Lidar: blocked by water clouds
Cloud radar: cloud area, strong attenuation in water cloud
Windprofiler: poor scanning capability

Figure 2.1: Active remote sensing of the atmosphere

active remote sensing and the other is passive remote sensing. Active remote sensing includes radars, lidars and sodars. Radiowaves, optical waves or acoustic waves are transmitted and the backscattered waves are received. The instruments are usually big and expensive. Passive remote sensing includes radiometric measurement using visible/infrared and microwave radiometers. It is very difficult to give range resolution capability. Even if it is possible by inversion techniques, the resolution is often very poor. However, the instruments are usually lighter, simpler and less expensive for one channel. Recent microwave radiometers have many channels to provide a lot of information regarding the atmosphere, land surface and ocean surface conditions.

Here, we would like to concentrate on the active remote sensing technique, especially radars, such as spaceborne rain radars, airborne rain radars, airborne imaging radar and windprofiler radars.

2.2 Active remote sensing of the atmosphere

Active remote sensors usually transmit pulses of radio, optical or acoustic waves and receive the scattered ones from targets (Fig. 2.1). The range of the target from the remote sensor can be measured from the time difference between the transmission and reception. Thanks to the range resolution capability, active remote sensors can provide the distribution of the scatterers, such as, raindrops. Using the Doppler function, they can also detect the radial component of the velocity of the scatterers. From this, the wind distribution can be estimated.

A well know instrument is the rain radar. The rain radar uses microwaves at 3 GHz (S-band), 5 GHz (C-band) and 10 GHz (X-band). It detects the backscattered radiowaves from hydrometeors. The observation range reaches more than 500 hundred kilometers for S-band radar. However, the rain radar does not generally detect very small particles like cloud droplet or aerosols.

A cloud radar is now being developed in several countries. The radar transmits much higher frequency radiowaves than those for the rain radar,

since the backscattering cross section of the particles is proportional to the 6th power of the diameter of the scattering particles in the Rayleigh regime where the radiowave wavelength is much larger than the diameter of the scattering particles. The radiowave frequencies are around 75 GHz or 95 GHz. The microwave technology in these bands is not mature and the radar needs technological development.

A windprofiler radar uses lower frequencies than those of rain radars. The scatterer for the windprofiler radar is atmospheric turbulence. Since the intensity of the component of the turbulence contributing to the radiowave scattering is weaker for the higher frequency radiowaves, windprofiler radars use lower frequencies than those for rain radars. Atmospheric turbulence is very common in the atmosphere, and the radar works even in the clear sky condition. It does not, however, have the volume scanning capability because of the long detection time to attain required sensitivity to detect very weak scattering radiowaves from the atmospheric turbulence.

Lidars use optical waves. Thanks to the very short wavelength of the optical waves, it can detect the backscattered waves from cloud particles and aerosols. However, the attenuation of the optical waves in water clouds is so big that it cannot penetrate water clouds.

Rain radars, cloud radars and lidars can operate not only on the ground but also on an aircraft and even on satellites. So, far, no rain radar or cloud radar have been in orbit, but the Tropical Rainfall Measuring Mission (TRMM) satellite equipped with a 14 GHz rain radar has been launched in 1997. A space lidar experiment has already been performed using the Shuttle.

Since any instrument does not always have the capability to observe all the atmosphere quantities, a combination of remote sensors is needed for comprehensive observation of the atmosphere. For example, a system using a UHF windprofiler, microwave radiometer, radiosonde receiver, and ground meteorological instruments has been developed in the U. S. A. (Parsons *et al.*, 1994, Wolfe *et al.*, 1995).

2.3 Rain observation from space

Environmental problems now have global scales. Global warming, the ozone hole, long range transport of pollutants and acid rains are very wide scale instead of local phenomena. Earth observation from space is a new technology which has a unique capability for observing these global scale phenomena. Since satellite observations are inherently on a global scale, they are very suitable for global scale phenomena. Since satellites observe Earth from space, the remote sensing technique is essential.

Global scale rain climatology is one of the objectives of Earth observation from space. Rain, especially tropical rain, is the major driving force of the atmospheric general circulation. Big spatial and temporal variations of rain make it difficult to obtain the climatology of rain on a global scale. Satellite observation has a possibility to overcome this obstacle.

The TRMM radar is the first spaceborne rain radar. TRMM is a collaborative venture between Japan and the U. S. A. and dedicated to the rain measurement in tropical and sub-tropical regions. The major product expected is the rain total in one month over an area of 5 degrees by 5 degrees. The orbit inclination of the satellite is 35 degrees and is non-sun synchronous. The non-sun synchronous orbit was chosen in order to eliminate biases in estimated rain totals due to the diurnal variation. The diurnal variation of rainfall is very big in tropical regions.

The frequency of the radar is 14 GHz which is slightly higher than conventional rain radars. The required spatial resolution is about 4 km at nadir. The radar antenna size is determined by the frequency and beam width. Narrow beam width which results in good spatial resolution requires a large antenna size, and the higher frequency allows the smaller antenna size. The antenna size is limited by the size of the rocket fairing. Thus, a higher frequency is more preferable. However, high frequency radiowaves suffer from rain attenuation. Therefore, the frequency of 14 GHz is determined from the trade-offs.

The radar applies an active phased array system. This system gives the radar very fast scanning capability without any mechanical movement. The radar consists of 128 sets of slotted waveguides, solid state transmitters and

receivers. This configuration gives more tolerance to the malfunctioning of the components. In other words, the radar has good redundancy.

Since long-term observations are required for global scale climate change, a TRMM follow-on is desirable to be launched without long interruption of the observations. According to the discussions so far, the inclination of the TRMM follow-on satellite is about 50–55 degrees to observe rain over mid-latitude regions. The satellite should be equipped with a radar with better sensitivity than TRMM to measure weaker rain than in the tropical region. Snow/raindrop discrimination may also be required. A multi-parameter radar is proposed, and a dual-wavelength radar may be most feasible.

2.4 Airborne rain radar

Airborne rain radars has been developed not only for TRMM but also for the study of future spaceborne rain radars. The first ambitious one was developed in the Communications Research Laboratory (CRL), Japan using two wavelengths, that is 10 GHz and 35 GHz. The antennas were designed to have the same beam width for the two wavelengths. This antenna configuration allowed direct comparison of the received signals at two wavelength. At 35 GHz, the rain attenuation is severe. For example, typical two way rain attenuation for 1 km range in a rain of 10 mm/h is about 5 dB. On the other hand, the rain attenuation for a 10 GHz radiowave is small. The difference of the attenuation can be used to estimate the rain intensity. The conventional method to estimate rain intensity is to convert the backscattering cross section or radar reflectivity to rain intensity using a semi-empirical formula. One of the advantages of the rain intensity estimation using rain attenuation is that the rain intensity has much better correlation to rain attenuation than to radar reflectivity. However, this method has a much narrower dynamic range and is more sensitive to noise.

So-called multi-parameter radars are expected to be in space. One of the candidates for the future spaceborne rain radar is the dual-wavelength radar. Another multi-parameter radar is the polarization radar. Ground-

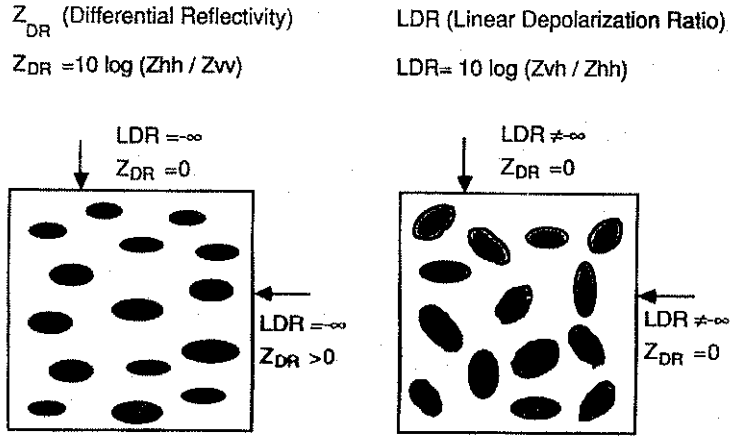

Figure 2.2: Polarization radar observation of precipitation particles. Left is for raindrops, and right is for ice particles.

based polarization radar is expected to be useful. But it may not be so suitable for a spaceborne one (Figs. 2.2 and 2.3). So-called Zdr measurement does not work in the near nadir direction and so-called LDR measurement needs much sensitivity improvement.

So far, two airborne rain radars for the study of TRMM and future spaceborne rain radars have been developed. They are ARMAR (Airborne Rain MApping Radar) developed in JPL (Burden *et al.*, 1994) , the U. S. A. and CAMPR (CRL's Airborne Multi-parameter Precipitation Radar) developed in CRL, Japan. Both apply the same frequency as the TRMM radar with Doppler function and polarization capability.

Another interesting airborne rain radar is a Doppler radar for quasi-dual Doppler measurement. It is now a conventional method to observe the wind field in rain areas using two or more Doppler radars on the ground. From the two Doppler radars, the two components of the radial velocity of the hydrometeors can be measured. From the two components, horizontal wind vectors can be estimated. This technique can be applied to an

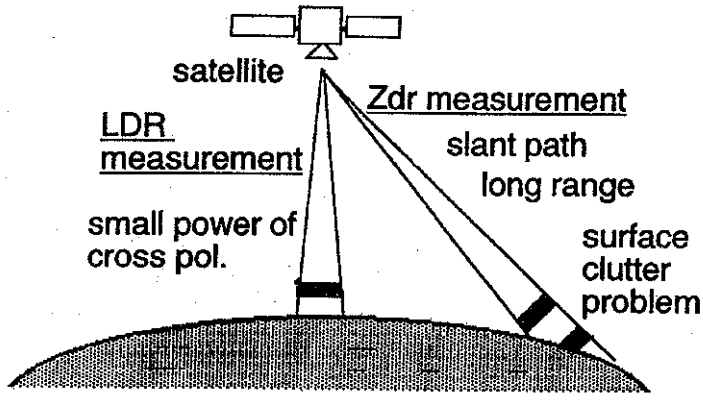

Figure 2.3: Difficulties of spaceborne polarization rain radar.

airborne Doppler rain radar. One radar called ELDORA/ASTRAIA has two plane antennas and observes rain with two directions. This configuration make a dual-Doppler radar measurement possible even during straight flight (Hildebrand *et al.*, 1994).

2.5 Airborne imaging radar

Airborne imaging radar is another application of radars aboard aircraft. The SLAR (Side-Looking Airborne Radar) is an imaging radar. Below shows an example of the SLAR developed in the CRL.

The SLAR is a real aperture X-band radar instead of a synthetic aperture one. The radar has a fan beam in the plane perpendicular to the flight direction and measures backscattered radiowaves from a large surface area. This gives SLAR an imaging capability without antenna scanning. The SLAR was originally developed to perform observations of an artificial oil slick. The oil surface suppresses small water waves and reduces the normalized backscattering cross section of the ocean surface for the off-nadir incidence microwaves. The oil slick appears as a dark area surrounded by

bright clean ocean in radar images. The capability was confirmed in an artificial oil slick observation experiment (T. Kozu *et al.*, 1987).

Spaceborne SAR is a well-know imaging radar and a simultaneous ocean observation was performed with the SLAR. The reduction of the scattering cross section was apparent in both images.

Drift ice observation was also perfomed simultaneously with a spaceborne SAR. There, the difference between backscattering cross sections of ocean and drift ice was clearly shown.

The SLAR can also be used for the land surface monitoring. CRL's SLAR was used to obtain a picture of the Unzen Volcano. Since microwave images do not suffer from clouds or rain, they produce more information than a visible image does, under adverse conditions.

2.6 Cloud radar

Clouds attract attention recently because the ambiguity of cloud effect on the global climate is recognized as one of the biggest obstacle for climate research. Visible or infrared observations from space provide only the horizontal distribution of clouds. However, the vertical structure is also very important to estimate the radiative effect of clouds. For this purpose, a cloud radar is now being developed (R. E. McIntosh *et al.*, 1988, A. Pazmany, 1994).

Since the cloud droplets are much smaller than raindrops, the frequency of the radar is very high. This means that new development of microwave technology is required.

The cloud radar is expected to be aboard satellites in the future.

2.7 Windprofiler radar

The windprofiler radar is a kind of a high sensitivity Doppler radar. The target is turbulence in the atmosphere. Since the turbulence is blown by the wind, the component along the antenna beam direction of the wind vector aloft can be measured. By shifting the antenna beam at least in

three directions and making an assumption of the uniformity of wind, three dimensional wind vectors can be estimated.

The advantages of the windprofiler radars may be summarized as desicribed below:

a. The windprofiler radar measures the wind in a pseudo continuous manner,

b. The sampling volume can be specified. This is contrary to the raw-insonde observation. The sonde is blown by wind,

c. The vertical air velocity can be measured. The vertical velocity is as important as the horizontal velocity but is difficult to directly measure by other than the windprofiler radar, and

d. The windprofiler radar can be operated unattended.

The advantages of a, b, and c are unique features as a wind sensor. The advantage of d is important, since the labor cost is expected to rise, and the operation cost is one of the major factors for operational use.

Turbulence in the atmosphere scatters radiowaves. The wavelength of the wave component in the turbulence which has half of the radiowave wavelength contributes to the scattering. This is so-called Bragg scattering.

The molecular viscosity is enhanced in the upper atmosphere because the mean free path length is long. Since small scale turbulence is suppressed by the molecular viscosity in the upper atmosphere, a longer wavelength radiowave is required for observation of the turbulence. The antenna beamwidth should be narrow enough for measuring the Doppler velocity and the large aperture is required for reception of very weak scattered radiowaves. Thus, the radar for observation of the upper atmosphere needs low frequency, a large aperture antenna, and high power. Typical upper atmosphere windprofiler radars use 50 MHz radiowaves and a 100 m by 100 m antenna with 1 MW peak power. This radar can measure the wind in the lower and upper stratosphere. For the troposphere wind observation, 400 MHz windprofilers are conventional. For the lower troposphere

and planetary boundary layer observation, 1 GHz windprofiler radars are usually used.

Not only wind observation, but also temperature profile observation is possible by a Radio Acoustic Sounding System (RASS) by adding an acoustic sound generator to the windprofiler radar. By following the acoustic wave by radar, acoustic velocity can be measured. Since the acoustic velocity depends on the temperature, the air temperature aloft can be estimated. RASS has the same advantages as the windprofiler radars, such that it can be operated in a psuedo continuous manner. The RASS is still in the developing phase but temperature is one of the major observables of the atmosphere, and the RASS gives another advantage to the windprofiler radar.

The windprofiler radar at around 50 MHz receives backscattered radiowaves by the turbulence and measures the wind in the region from 500 m to about 25–30 km height. For the region above 60 km the backscattering is again enhanced and the wind observation is possible up to 100 km. This radar measures the wind continuously up to 25–30 km height and can be an alternative for wind observation to the routine rawin sonde which observes the atmosphere up to about 30 km.

The windprofiler at 400 MHz may be the most important for the routine weather observation. This radar measures the wind up to about 15 km and covers all the troposphere. The size of the radar is typically 10 m by 10 m and the transmitting power is a few tens kW, which has little technological difficulty.

1000 MHz windprofiler radars measure wind in the lower atmosphere. The lower atmosphere including the boundary layer has a direct influence on human activities. Pollution is one example. Observation around airports is expected to be more common in the future.

2.8 Lidars

Lidars seems to have a bright future. Optical technology is progressing rapidly even now, and new laser sources are continuously found. The system

may be much smaller than radars. Lidars can not only detect small particles in the atmosphere but also can measure wind velocity which transports the small particles using the Doppler function. One very ambitious plan is the Laser Atmospheric Wind Sounder (LAWS) proposed by NASA. LAWS is a powerful Doppler lidar and dedicated to measure wind distribution in the troposphere. Unfortunately, the proposal has not yet been approved but the technological development is continuing (Baker *et al.*, 1995).

Observation of the distribution of water vapor is very difficult. Radiosondes measure humidity in the atmosphere directly, but it is very limited in space and time domains. Satellite observation using microwave radiometers applies inversion techniques, but it has only poor range resolution. Some attempt have been performed to deduce water vapor profiles from windprofiler radar data using the fact that strong scattering occurs in a big humidity gradient region. This technique is, however, still in the experimental phase. Lidar techniques are expected to be the most suitable. The so-called Raman lidar detects backscattering optical waves with a frequency shift from the transmitted optical wave due to water vapor. So-called DIAL lidars use the difference of the attenuation by water vapor in slightly different wavelengths.

2.9 Remarks

Earth's atmosphere is a complex system. Since environment problems are closely connected to phenomena in the atmosphere, the technology to observe the atmosphere becomes more and more important. Radio and optical remote sensing technology is now applied not only on the ground but also on aircraft and satellites. The capability of four-dimensional observations is essential for atmospheric studies. For remote areas, the capability of unattended operation is a big advantage. Global scale observations are now performed by sensors aboard satellites, and remote sensing techniques are essential for the satellite observation.

Even though the remote sensing technique has many advantages, it also has disadvantages. The very basic disadvantage is that remote sensing

does not directly provide physical quantities required. Many sophisticated algorithms to deduce required data from remote sensing data are needed. Combining of data measured by many kinds of remote sensors becomes common. Ground truth data are also important to validate the products which remote sensors provide.

References

[1] Baker, W. E. *et al.*, 1995, Lidar-measured winds from space: A key component for weather and climate prediction, *Bul. Amer. Meteor. Soc.*, **76** (6), 869–888.

[2] Burden, S. L., E. Im, F. K. Li, W. Ricketts, A. Tanner, and W. Wilson, 1994: ARMAR: An airborne rain-mapping radar, *J. Atmos. Oceanic Technol.*, **11**, 727–737.

[3] Hildebrand, P. H., C. A. Walther, C. L. Frush, J. Testud and F. Baudin, 1994: The ELDORA/ASTRAIA airborne Doppler weather radar: Goals, design, and first field tests, *Proc. IEEE*, **82**, 1873–1890.

[4] Kozu, T., T. Umehara, T. Ojima, T. Suitsu, H. Masuko and H. Inomata, 1987, Observation of oil slicks on the ocean by X-band SLAR, *Proc. IGARSS* '87.

[5] McIntosh, R. E., R. M. Narayanan, J. B. Mead and D. H. Schaubert, 1988: Design and performance of a 215 GHz pulsed radar system, *IEEE Trans. Microwave Theory Technol.*, **36**, 994–1001.

[6] Parsons, D. *et al.*, 1994: The integrated sounding system: Description and preliminary observations from TOGA-COARE., *Bull. Amer. Meteor. Soc.*, **75**, 553–567.

[7] Pazmany, A., J. Mead and R. McIntosh, 1994: 95-GHz polarimetric radar measurements of orographic cap clouds, *J. Atmos. Oceanic Technol.*, **11**, 14–153.

REFERENCES

[8] Wolfe, D. *et al.*, 1995: An overview of the mobile profiler system: Preliminary results from field tests during the Los Angeles free-radical study. *Bull. Amer. Meteor. Soc.*, **76**, 523–534.

Chapter 3

Doppler Radar Measurements of a Kinematic Wind Field

Kazuhisa Tsuboki
Institute for Hydrospheric-Atmospheric Sciences, Nagoya University
Furo-cho, Chikusa-ku, Nagoya, 464-8601, Japan
Phone: +81-52-789-3493, fax: +81-52-789-3436
E-mail: tsuboki@ihas.nagoya-u.ac.jp

3.1 Introduction

Meteorological Doppler radar is an instrument to measure velocity of a moving target by the Doppler effect of electro-magnetic waves. Meteorological observations with Doppler radars have been carried out since the 1970s. Technical development of Doppler radar observations have been significant in the United States in 1980s. Doppler radar is one of the most effective instruments for observations of severe rain and snow storms.

Since a single Doppler radar measures the radial component of velocity, a simultaneous observation with two or three Doppler radars is necessary to

determine a detailed flow field in a convective storm. On the other hand, some methods to determine the wind field from a single Doppler radar observation have been also developed. One analysis method using Doppler velocity to determine the wind field is the Velocity Azimuth Display (VAD) method. This method will provide a profile of kinematic properties of the wind field above the radar such as velocity, divergence and deformation.

If two or three Doppler radars are used for observations simultaneously, it is possible to determine a detailed 3-dimensional wind field in a storm. In order to investigate kinematic and dynamic structures of storm, this type of observation is necessary.

In this text, two elementary methods of Doppler velocity analysis will be introduced; one is the VAD method (Tsuboki and Wakahama, 1988[5]) and the other a dual Doppler measurement method (Satoh and Wakahama, 1991[6]). Detailed descriptions of these methods will be presented and some examples obtained from these methods will be shown in this text.

3.2 VAD with least-square-fitting method

The Velocity Azimuth Display (VAD) is a scanning mode of the Doppler radar, in which the radar antenna is rotated about a vertical axis at a constant elevation (Fig. 3.1). Consider a Cartesian coordinate system with x positive toward the east, y positive toward the north and z positive upward. A Doppler radar is located at the origin of the coordinate. The azimuth variation of Doppler velocity $V_R(\theta)$ along a scanned circle will be given by

$$V_R(\theta) = -V_H \cos(\theta_e)\cos(\phi - \theta) + V_F \sin(\theta_e) \tag{3.1}$$

where V_H is horizontal wind speed, ϕ wind direction, θ azimuth angle from the north, θ_e elevation angle of antenna, and V_F fall speed of precipitation. Conventionally $V_R(\theta)$ is taken to be positive toward the radar and V_F is positive downward. The north and east components of horizontal wind V_X and V_Y are

$$V_X = \quad V_H \sin(\phi), \tag{3.2}$$

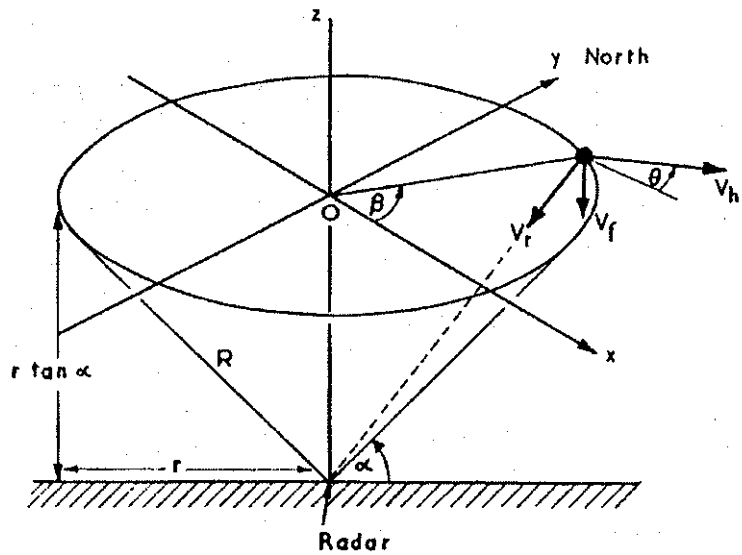

Figure 3.1: Geometry of VAD radar scan. (After Browning and Wexler, 1968[1])

$$V_Y = V_H \cos(\phi). \tag{3.3}$$

The Taylor series expansion of V_X, V_Y with respect to the center of the scanned circle, ignoring higher order terms, is

$$V_X = V_{X0} + \frac{\partial V_X}{\partial x} x + \frac{\partial V_X}{\partial y} y, \tag{3.4}$$

$$V_Y = V_{Y0} + \frac{\partial V_Y}{\partial x} x + \frac{\partial V_Y}{\partial y} y, \tag{3.5}$$

where the subscript 0 means the value at the center. The horizontal distances of x and y directions are

$$x = r \sin(\theta), \tag{3.6}$$

$$y = r\cos(\theta), \tag{3.7}$$

where r is the radius of the scanned circle. Assuming the fall speed V_F is horizontally homogeneous and introducing (3.2)~(3.7) into (3.1) give

$$\begin{aligned} V_R(\theta) = & -\frac{1}{2}r\cos(\theta_e)\left(\frac{\partial V_X}{\partial x}+\frac{\partial V_Y}{\partial y}\right)+V_F\sin(\theta_e) \\ & - V_{X0}\cos(\theta_e)\sin(\theta) \\ & - V_{Y0}\cos(\theta_e)\cos(\theta) \\ & - \frac{1}{2}r\cos(\theta_e)\left(\frac{\partial V_X}{\partial y}+\frac{\partial V_Y}{\partial x}\right)\sin(2\theta) \\ & - \frac{1}{2}r\cos(\theta_e)\left(\frac{\partial V_Y}{\partial y}-\frac{\partial V_X}{\partial x}\right)\cos(2\theta). \end{aligned} \tag{3.8}$$

On the other hand let us consider an approximation of $V_R(\theta)$ with the function

$$V_R(\theta) = A_1 + A_2\sin(\theta) + A_3\cos(\theta) + A_4\sin(2\theta) + A_5\cos(2\theta). \tag{3.9}$$

Equation (3.9) expresses zeroth, first and second harmonics of the Fourier expansion of $V_R(\theta)$. Each component has a physical meaning as shown in Fig. 3.2. The zeroth component is related to the divergence at the center of the scanned circle. The first harmonic is horizontal velocity and the second harmonics deformation. Comparing (3.8) and (3.9), the coefficients A_1~A_5 will be

$$A_1 = -\frac{1}{2}r\cos(\theta_e)\left(\frac{\partial V_X}{\partial x}+\frac{\partial V_Y}{\partial y}\right)+V_F\sin(\theta_e), \tag{3.10}$$

$$A_2 = -V_{X0}\cos(\theta_e), \tag{3.11}$$

$$A_3 = -V_{Y0}\cos(\theta_e), \tag{3.12}$$

$$A_4 = -\frac{1}{2}r\cos(\theta_e)\left(\frac{\partial V_X}{\partial y}+\frac{\partial V_Y}{\partial x}\right), \tag{3.13}$$

$$A_5 = -\frac{1}{2}r\cos(\theta_e)\left(\frac{\partial V_Y}{\partial y}-\frac{\partial V_X}{\partial x}\right). \tag{3.14}$$

Browning and Wexler (1968)[1] obtained the coefficients $A_1 \sim A_5$ by Fourier integration as

$$A_1 = \frac{1}{360}\Sigma V_R(\theta_i), \tag{3.15}$$

$$A_2 = \frac{1}{180}\Sigma V_R(\theta_i)\sin(\theta_i), \tag{3.16}$$

$$A_3 = \frac{1}{180}\Sigma V_R(\theta_i)\cos(\theta_i), \tag{3.17}$$

$$A_4 = \frac{1}{180}\Sigma V_R(\theta_i)\sin(2\theta_i), \tag{3.18}$$

$$A_5 = \frac{1}{180}\Sigma V_R(\theta_i)\cos(2\theta_i), \tag{3.19}$$

where Σ is summation with respect to $i = 1 \sim 360$.

This method is very effective for determining kinematic properties of the wind field. However, errors will become large when Doppler velocity data along the scanned circle become inhomogeneous and the number of data is small. Another method is a least squares fitting of V_R by (3.9). This method will give a more accurate result even when the number of data is small.

The calculation of $A_1 \sim A_5$ of (3.9) by the least square fitting is as follows. Summation of squared differences between the observed non-zero Doppler velocity V_{Ri} and (3.9) is

$$R = \sum_i [V_{Ri} - A_1 - A_2\sin(\theta_i) - A_3\cos(\theta_i) - A_4\sin(2\theta_i) - A_5\cos(2\theta_i)]^2 \tag{3.20}$$

In order to find the best fitting curve, the partial derivatives of R by $A_1 \sim A_5$ are set to be zero.

$$\frac{\partial R}{\partial A_1} = -2\Sigma(V_{Ri} - P_i) = 0, \tag{3.21}$$

$$\frac{\partial R}{\partial A_2} = -2\Sigma(V_{Ri} - P_i)\sin(\theta_i) = 0, \tag{3.22}$$

$$\frac{\partial R}{\partial A_3} = -2\Sigma(V_{Ri} - P_i)\cos(\theta_i) = 0, \tag{3.23}$$

$$\frac{\partial R}{\partial A_4} = -2\Sigma(V_{Ri} - P_i)\sin(2\theta_i) = 0, \tag{3.24}$$

$$\frac{\partial R}{\partial A_5} = -2\Sigma(V_{Ri} - P_i)\cos(2\theta_i) = 0, \tag{3.25}$$

where P_i is

$$P_i = A_1 + A_2\sin(\theta_i) + A_3\cos(\theta_i) + A_4\sin(2\theta_i) + A_5\cos(2\theta_i). \tag{3.26}$$

The system of equations (3.21)$\sim$(3.25) are normal with respect to the unknown variables $A_1 \sim A_5$. They can be written in a matrix form as

$$\mathrm{SA} = \mathrm{V}, \tag{3.27}$$

where

$$\mathrm{S} = (S_{ij}), \tag{3.28}$$

$$\mathrm{A} = (A_1, A_2, A_3, A_4, A_5)^T, \tag{3.29}$$

$$\mathrm{V} = (V_i)^T. \tag{3.30}$$

The variables $A_1 \sim A_5$ will be determined as

$$\mathrm{A} = \mathrm{S}^{-1}\mathrm{V}, \tag{3.31}$$

where components of the matrix S are

$$\begin{aligned}
S_{11} &= \Sigma \quad i, \\
S_{22} &= \Sigma \quad \sin 2(\theta_i), \\
S_{33} &= \Sigma \quad \cos 2(\theta_i), \\
S_{44} &= \Sigma \quad \sin 2(2\theta_i), \\
S_{55} &= \Sigma \quad \cos 2(2\theta_i),
\end{aligned}$$

$$
\begin{aligned}
S_{12} = \quad S_{21} &= \Sigma \sin(\theta_i), \\
S_{13} = \quad S_{31} &= \Sigma \cos(\theta_i), \\
S_{14} = \quad S_{41} &= \Sigma \sin(2\theta_i), \\
S_{15} = \quad S_{51} &= \Sigma \cos(2\theta_i), \\
S_{23} = \quad S_{32} &= \Sigma \sin(\theta_i)\cos(\theta_i), \\
S_{24} = \quad S_{42} &= \Sigma \sin(\theta_i)\sin(2\theta_i), \\
S_{25} = \quad S_{52} &= \Sigma \sin(\theta_i)\cos(2\theta_i), \\
S_{34} = \quad S_{43} &= \Sigma \cos(\theta_i)\sin(2\theta_i), \\
S_{35} = \quad S_{53} &= \Sigma \cos(\theta_i)\cos(2\theta_i), \\
S_{45} = \quad S_{54} &= \Sigma \sin(2\theta_i)\cos(2\theta_i).
\end{aligned}
$$

Components of the vector V are

$$
\begin{aligned}
V_1 &= \Sigma V_i, \\
V_2 &= \Sigma V_i \sin(\theta_i), \\
V_3 &= \Sigma V_i \cos(\theta_i), \\
V_4 &= \Sigma V_i \sin(2\theta_i), \\
V_5 &= \Sigma V_i \cos(2\theta_i).
\end{aligned}
$$

Equation (3.31) will give the coefficients $A_1 \sim A_5$.

From these coefficients $A_1 \sim A_5$ of (3.9), using (3.10)$\sim$(3.14), the kinematic properties of a wind field above the radar are determined as follows;

Horizontal divergence: DivV_H

$$
\begin{aligned}
\mathrm{Div}V_H &= \left(\frac{\partial V_X}{\partial x} + \frac{\partial V_Y}{\partial y}\right) \\
&= \frac{2}{r} V_F \tan(\theta_e) - \frac{2}{r}\frac{A_1}{\cos(\theta_e)}
\end{aligned} \tag{3.32}
$$

Horizontal wind velocity : V_H

$$
\begin{aligned}
V_H &= (V_{X0}^2 + V_{Y0}^2)^{\frac{1}{2}} \\
&= \frac{(A_2^2 + A_3^2)^{\frac{1}{2}}}{\cos(\theta_e)}
\end{aligned} \tag{3.33}
$$

Wind direction:ϕ

$$\phi = \tan^{-1}\left(\frac{A_2}{A_3}\right) \qquad : A_3 > 0 \tag{3.34}$$

$$\phi = \tan^{-1}\left(\frac{A_2}{A_3}\right) + \pi \qquad : A_3 < 0 \tag{3.35}$$

Deformation:Def V_H

$$\begin{aligned} \mathrm{Def}V_H &= \left[\left(\frac{\partial V_X}{\partial y} + \frac{\partial V_Y}{\partial x}\right)^2 + \left(\frac{\partial V_Y}{\partial y} - \frac{\partial V_X}{\partial x}\right)^2\right]^{\frac{1}{2}} \\ &= \frac{2}{r}\frac{(A_4^2 + A_5^2)^{\frac{1}{2}}}{\cos(\theta_e)} \end{aligned} \tag{3.36}$$

Orientation of the axis of dilatation : δ

$$\delta = \frac{1}{2}\tan^{-1}\left(\frac{A_4}{A_5}\right) \qquad : A_5 > 0 \tag{3.37}$$

$$\delta = \frac{1}{2}\tan^{-1}\left(\frac{A_4}{A_5}\right) + \frac{1}{2}\pi \qquad : A_5 < 0 \tag{3.38}$$

Another important kinematic property is the vorticity. It is, however, impossible to determine vorticity with respect to the center, because a Doppler radar does not measure the tangential component of velocity.

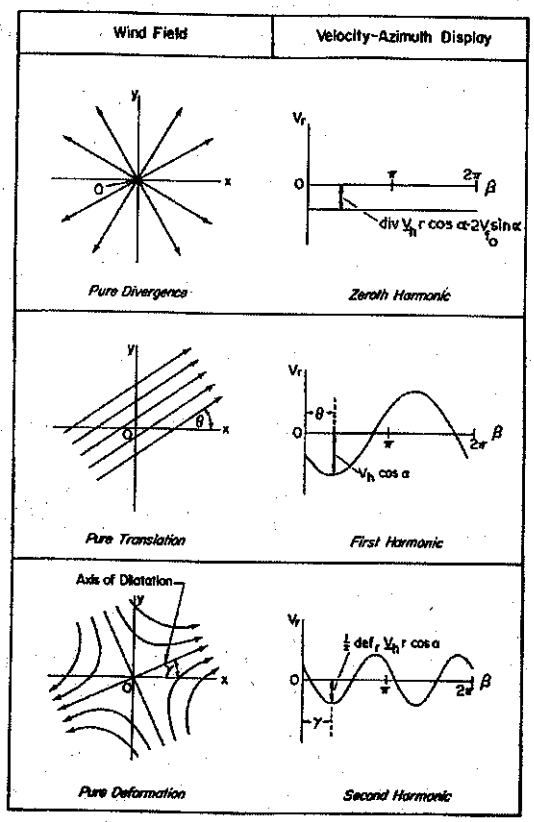

Figure 3.2: Three simple wind fields and Fourier components of VAD curves. (After Browning and Wexler, 1968[1])

3.3 Calculation of vertical velocity

Since the vertical velocity is not measured directly by the VAD method, we integrate an equation of continuity to find the vertical velocity. The equation of continuity in the anelastic system (Ogura and Philips, 1962[3]) is

$$\frac{\partial V_X}{\partial x} + \frac{\partial V_Y}{\partial y} + \frac{\partial W}{\partial z} = -\frac{W}{\rho}\frac{\partial \rho}{\partial z} \tag{3.39}$$

The vertical velocity W(Z) at a height of Z is

$$W(Z) = \frac{\rho_0}{\rho}W_0 - \frac{1}{\rho}\int_{Z_0}^{Z} \rho(\zeta)\mathrm{Div}V_H(\zeta)d\zeta \tag{3.40}$$

where ρ_0 and W_0 are the air density and vertical velocity at a height of $z = Z_0$, respectively.

If we use the scale height H, then (3.40) is can be rewritten as

$$W(Z) = W_0 \exp\left(\frac{Z}{H}\right) - \exp\left(\frac{Z}{H}\right)\int_{Z_0}^{Z} \exp\left(\frac{-\zeta}{H}\right)\mathrm{Div}V_H(\zeta)d\zeta \tag{3.41}$$

or in a finite difference form as

$$W(Z) = W_0 \exp\left(\frac{Z}{H}\right) - \exp\left(\frac{Z}{H}\right)\sum_i \exp\left(\frac{-Z_i}{H}\right)\mathrm{Div}V_H(Z_i)\Delta Z \tag{3.42}$$

If we take $T = 273$, $H = RT/g$ is$\sim$8 km, where R is the gas constant of dry air, g acceleration due to gravity, and T temperature.

3.4 Extended VAD methods

3.4.1 VAD with two elevation angles

In the calculation of VAD, the fall speed of precipitation is determined empirically. If the precipitation is snow, the fall speed is assumed to be a constant -1 m s^{-1}. If the precipitation is rain, it is estimated from the

radar reflectivity. The extended VAD method, on the contrary, determines both divergence and fall speed directly.

Assume we have the coefficients A_1 of (3.9) at a height of h from two VAD scans at two different elevation angles θ_{e1} and θ_{e2}: A_{11} and A_{12}. Since $r = h\cot(\theta_e)$,

$$A_{11} = -\frac{1}{2}h\mathrm{Div}V_H\cos(\theta_{e1})\cot(\theta_{e1}) + V_F\sin(\theta_{e1}) \tag{3.43}$$

$$A_{12} = -\frac{1}{2}h\mathrm{Div}V_H\cos(\theta_{e2})\cot(\theta_{e2}) + V_F\sin(\theta_{e2}) \tag{3.44}$$

From these two equations, $\mathrm{Div}V_H$ and V_F are given by

$$\mathrm{Div}V_H = \frac{2[A_{11}\sin(\theta_{e2}) - A_{12}\sin(\theta_{e1})]\sin(\theta_{e1})\sin(\theta_{e2})}{h\sin(\theta_{e1}+\theta_{e2})\sin(\theta_{e1}-\theta_{e2})} \tag{3.45}$$

$$V_F = \frac{A_{11}\sin(\theta_{e1})\cos^2(\theta_{e2}) - A_{12}\sin(\theta_{e2})\cos^2(\theta_{e1})}{\sin(\theta_{e1}+\theta_{e2})\sin(\theta_{e1}-\theta_{e2})} \tag{3.46}$$

If we make this calculation at each height, we obtain the profile of divergence and fall speed. Equations (3.45) and (3.46) indicate if the difference of the two elevation angles is small, the error is large.

3.4.2 Multi-elevation VAD

Srivastava *et al.* (1986)[4] developed a method to calculate horizontal divergence and fall speed from a multi-elevation VAD.

Assume N VAD scans give N coefficients of A_1. Equation (3.10) of A_{1i} of the ith VAD at a height of h will be

$$A_{1i} = -\frac{1}{2}h\mathrm{Div}V_H\cos(\theta_{ei})\cot(\theta_{ei}) + V_F\sin(\theta_{ei}) \tag{3.47}$$

where $r = h\cot(\theta_e)$. The equation (3.47) will be rewritten as

$$A_{1i}\mathrm{cosec}(\theta_{ei}) = -\frac{1}{2}h\cot^2(\theta_{ei})\mathrm{Div}V_H + V_F \tag{3.48}$$

If we take

$$Y_i = A_{1i}\mathrm{cosec}(\theta_{ei}) \tag{3.49}$$

$$X_i = -\frac{1}{2}h\cot^2(\theta_{ei}) \tag{3.50}$$

Equation (3.48) will be

$$Y_i = \mathrm{Div}V_H X_i + V_F \tag{3.51}$$

From N VAD scans, we obtain N sets of (X_i, Y_i). A regression line of the sets is calculated by a least square method. Its gradient gives horizontal divergence and the intercept is the fall speed of precipitation.

3.5 Example VAD analysis

This section presents an example of VAD analysis. Data was obtained by the Doppler radar of the Institute of Low Temperature Science, Hokkaido University when a synoptic scale cyclone brought a snow storm to Hokkaido on 23 January 1988. Precipitation was in the form of snow. Therefore the fall speed was assumed to be a constant -1m s^{-1}. The elevation angle of the Doppler radar was 20 degrees.

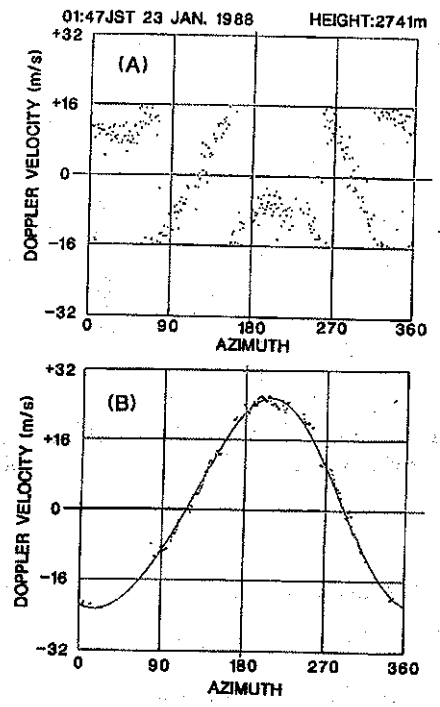

Figure 3.3: (a) Azimuth variation of Doppler velocity at a height of 2741 m at 0147 JST, 23 January 1988. (b) Doppler velocity with a best fitting curve after corrections of Nyquist velocity and noise.

Figure 3.3a shows the azimuth variation of Doppler velocity at a height of 2741 m. Since the Nyquist velocity of the Doppler radar is 16 m s^{-1}, the Doppler velocity lager than $\pm$ 16 m s^{-1} is expressed as $V_R \mp 32$ m s^{-1}. After corrections of the Nyquist velocity and noise, the least squares fitting of (3.9) was performed (Fig. 3.3b). The best fitted curve represents the azimuth variation of V_R. The correlation coefficient of the curve to V_R was 0.9969.

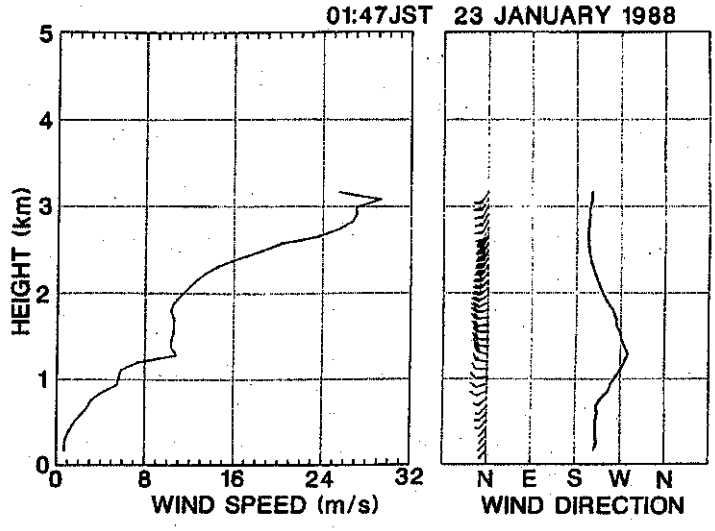

Figure 3.4: Profiles of wind velocity and direction obtained from VAD at 0147 JST, 23 January 1988.

The vertical profile of the horizontal wind speed and wind direction at 0147 JST, 23 January 1988 are shown in Fig. 3.4. A detailed structure of the wind profile is clear. The wind speed was small below a height of 1.5 km and veered with height below this altitude. Above this height the wind backed with height and wind speed had significant shear. The profile of wind speed between 2 and 3 km of height is hyperbolic tangent shaped.

This suggests the occurrence of a disturbance due to the shear instability.

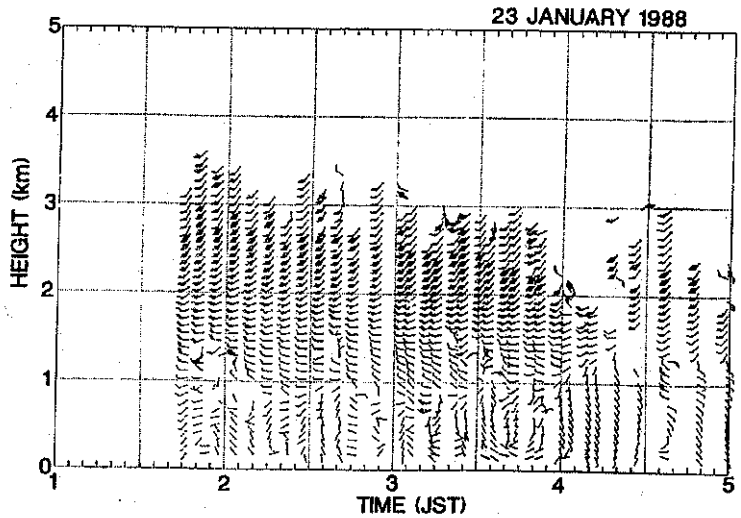

Figure 3.5: Time-height cross section of wind obtained from VAD on 23 January 1988.

If we make successive VAD scans, we can obtain the detailed structure of the variation of the wind. An example of a time-height cross section is shown in Fig. 3.5. The wind was backing above 1.5 km in height and veering below the height during the observation. This corresponds to upper-level cold advection and lower-level warm advection, which resulted in an unstable stratification. There was a layer in which the vertical shear was intense between 2 and 3 km in height. Below 1 km, the wind speed was small while a southeasterly wind was present after 4 JST, 23 January 1988.

3.6 Dual Doppler radar measurement

In order to obtain detailed structure of the flow field in a storm, dual or triple Doppler radar observation is necessary, because the 3-dimensional flow field in a precipitation system is complex and varies with time and space. In this section, a fundamental of dual Doppler analysis will be described and an example will be presented.

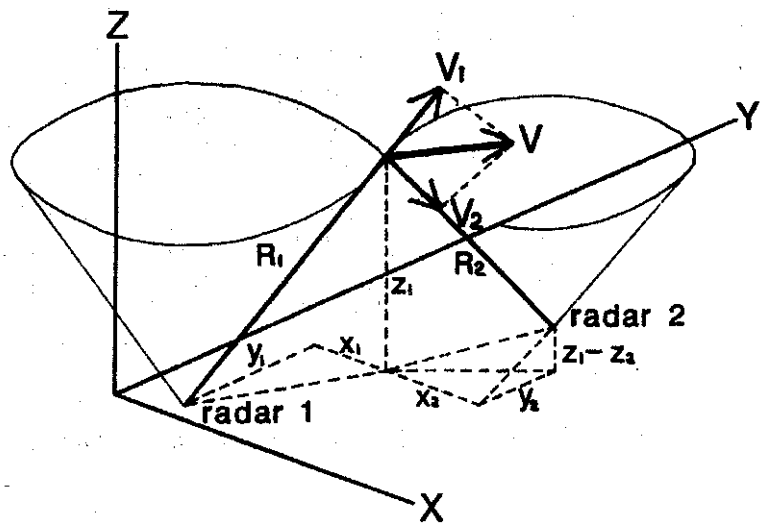

Figure 3.6: Setting of dual Doppler radars. (After Satoh and Wakahama, 1991[6])

We consider again a Cartesian coordinate system with x positive toward the east, y positive toward the north and z positive upward. Two Doppler radars are assumed to be located at the origin (Radar 1) of the coordinates and at a point (X_2, Y_2, Z_2) (Radar 2). The radars observe a velocity of (u, v, W) at a point of (x, y, z) and obtain Doppler velocities V_{R1} and V_{R2} (Fig. 3.6). Where $W = w + V_F$. Then, we have relations of

$$R_1 V_{R1} = ux + vy + Wz \tag{3.52}$$
$$R_2 V_{R2} = u(x - X_2) + v(y - Y_2) + W(z - Z_2) \tag{3.53}$$

This equations will be rewritten in a matrix form as

$$\mathbf{PV} = \mathbf{R} \tag{3.54}$$

where

$$\mathrm{P} = \begin{pmatrix} x & y \\ x - X_2 & y - Y_2 \end{pmatrix} \tag{3.55}$$

$$\mathbf{V} = \begin{pmatrix} u \\ v \end{pmatrix} \tag{3.56}$$

$$\mathbf{R} = \begin{pmatrix} R_1 V_{R1} - Wz \\ R_2 V_{R2} - W(z - Z_2) \end{pmatrix} \tag{3.57}$$

Vertical velocity is calculated from the equation of continuity (3.39) or its integral form (3.40). The fall velocity of precipitation is determined empirically from the radar reflectivity. From (3.40) and (3.54), the three components of velocity (u, v, w) are determined. Since (3.40) and (3.54) are complex, the calculation is carried out iteratively.

In dual Doppler analysis, the accuracy of velocity fields and area of observation is determined by the locations of the two Doppler radars. Lhermitte and Miller (1970)[2] showed a relationship between the variances of Doppler velocity σ_1^2, σ_2^2 and variance of (u, v), σ_u^2, σ_v^2 is

$$\frac{\sigma_u^2 + \sigma_v^2}{\sigma_1^2 + \sigma_2^2} = \mathrm{cosec}^2\beta \tag{3.58}$$

where β is the angle formed by the two Doppler radars and target. If $\beta = 90°$, calculated (u, v) is as accurate as the variances of Doppler velocities. As β departs from 90°, the accuracy becomes lower.

3.7 Example of dual Doppler analysis

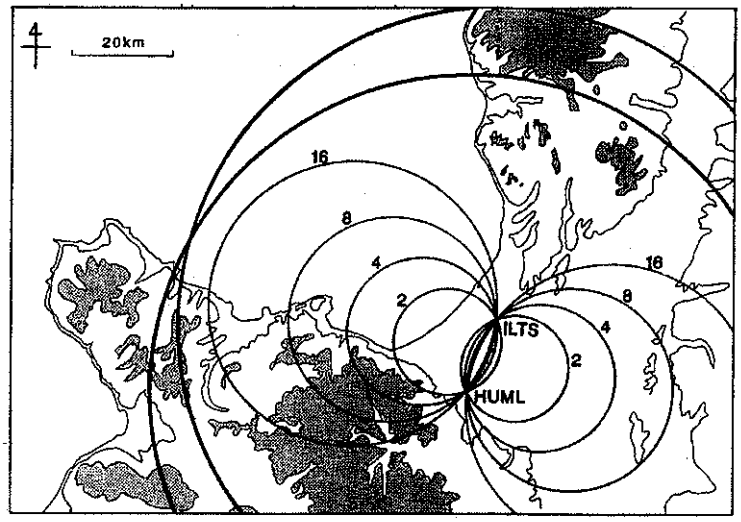

Figure 3.7: Topography and locations of two Doppler radars of Hokkaido University in the Ishikari Plain. The numbers in the figure are values of $\mathrm{cosec}^2\beta$. (After Satoh and Wakahama, 1991[6])

In this section, we present an example of dual Doppler radar analysis. Two Doppler radars of Hokkaido University observed a band cloud formed off the west coast of Hokkaido on 23 January 1990. Figure 3.7 shows topography and locations of the Doppler radars. Figure 3.8 shows a flow field and reflectivity at a height of 250 m. The velocity field clearly showed a convergence zone which is oriented from the north to south. On the west side of the convergence zone, there was a monsoon northwesterly wind with a relatively large wind speed. On the east side, a land breeze came from the land of Hokkaido. The convergence line is considered to be a land breeze front. The band cloud was developed alone the land breeze front. It is also

clear that a vortex disturbance developed along the convergence zone.

A vertical cross section along AB in Fig. 3.8 is shown in Fig. 3.9. One problem in the calculation of vertical velocity is uncertainty of the boundary conditions. There are two fundamental methods of calculation; one is upward integration of (3.40) with zero velocity at the lowest level and the other downward integration with zero velocity at the top of echo. Figure 3.9a shows a result obtained from the former method and Fig. 3.9b from the latter method. Both results show a land breeze front around a distance of -18 km and a shallow land breeze was present below the northwesterly monsoon wind. The upward motion at the front is clear. On the other hand, the distributions of vertical velocity are slightly different. This is attributed to the errors of divergence and boundary conditions. For an improvement of this discrepancy, some correction will be necessary.

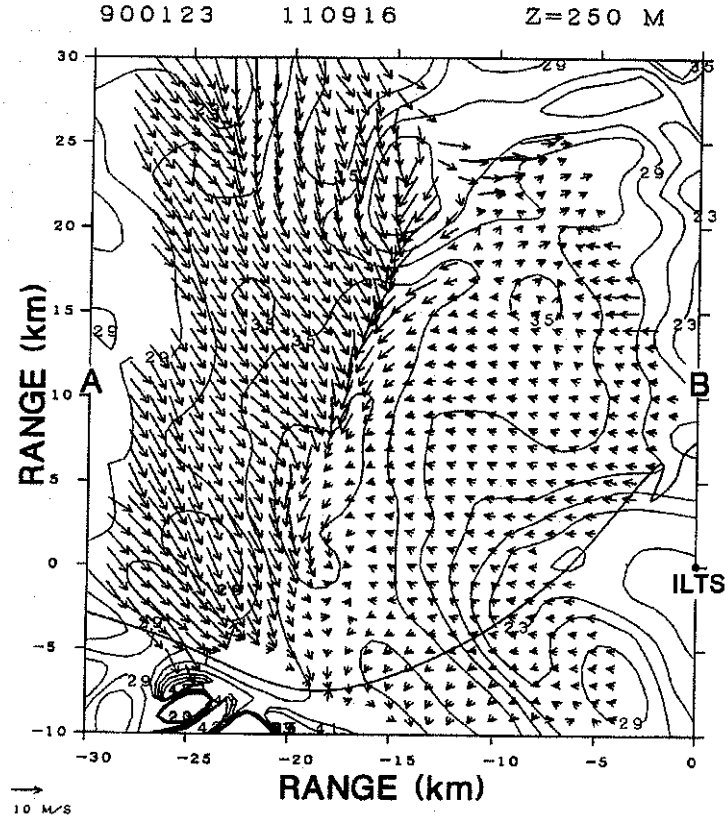

Figure 3.8: Horizontal wind field and radar reflectivity obtained from dual Doppler radar analysis at 1109 JST, 23 January 1990. (After Satoh and Wakahama, 1991[6])

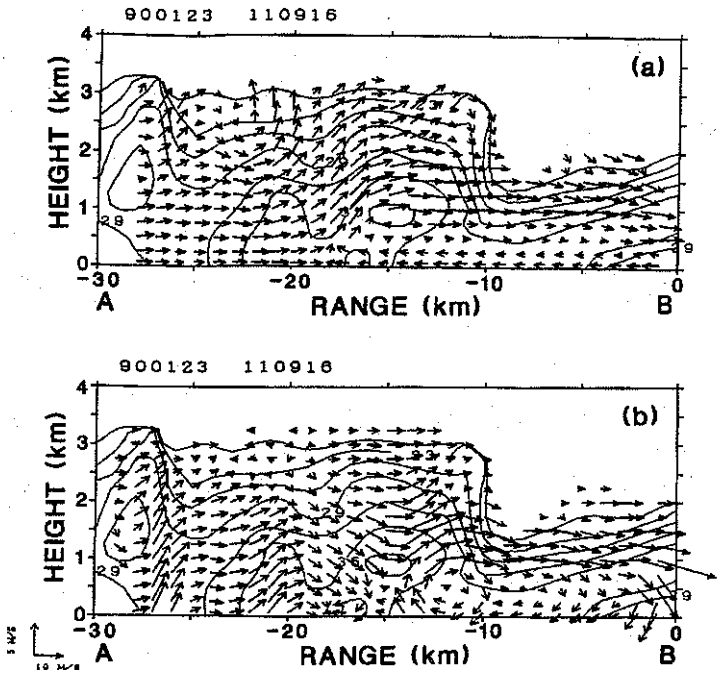

Figure 3.9: Vertical cross section of wind field and radar reflectivity along AB in Fig. 3.8. (a) Upward integration with $w = 0$ at the lowest level and (b) downward integration with $w = 0$ at the top of echo. (After Satoh and Wakahama, 1991[6])

References

[1] Browning, K.A. and R. Wexler, 1968: The determination of kinematic properties of a wind field using Doppler radar. *J.Appl.Meteor.*, **7**, 105–113.

[2] Lhermitte, R. M., and L.J. ,Miller, 1970: Doppler radar methodology for the observation of convective storms. *Preprints 14th Conf. Radar Meteorology*, Tucson, *Amer. Meteor. Soc.*, 133–138

[3] Ogura, Y. and N.A. Phillips, 1962: Scale analysis of deep and shallow convection in the atmosphere. *J.Atmos.Sci.*, **19**, 173–179.

[4] Srivastava, R.C., T.J. Matejka, and T.J. Lorello, 1986: Doppler radar study of the trailing anvil region associated with a squall line. *J.Atmos.Sci.*, **43**. 356–377.

[5] Tsuboki, K. and G. Wakahama, 1988: Single Doppler Radar Measurements of a Kinematic Wind Field: VAD Analysis Based on a Least-Square-Fitting Method. *Low Temperature Science,* **Scr. A47**, 73–88.

[6] Satoh, S. and G. Wakahama, 1991: Dual Doppler Radar Measurements of a 3-dimensional Wind Field. *Low Temperature Science,* **Scr. A50**, 23–35.

Chapter 4

Radar Rainfall Measurement

Toshiaki Kozu
Communications Research Laboratory
Ministry of Posts and Telecommunications, Japan
4-2-1 Nukui-kita-machi, Koganei, Tokyo 184-8795, Japan
Phone: +81-423-27-7543, fax: +81-423-27-6666
E-mail: kozu@crl.go.jp

This text, mainly based on my Dr. E dissertation submitted to Kyoto University in 1991, is prepared for the 8th IHP training course held in March 1999. The content of this text is as follows: (1) rainfall parameters related to the radar measurement of rain are outlined, (2) basic theory of radar rainfall measurement and (3) rainfall parameter estimation from radar measurements. A comprehensive list of references is also attached.

4.1 Rainfall Parameters Related to Radar Measurement

4.1.1 Definitions of meteorological parameters

As a preparation for the discussion of radar rainfall measurements, it is helpful to summarize various radar and meteorological quantities. They include

Table 4.1: Definitions and units of meteorological and radar quantities used in this chapter.

Quantity	Symbol	Definition	Unit
Frequency	f	-	Hz
Wavelength	λ	-	m
Speed of light	c	2.99792×10^8	m/sec
Refractive index	m	$m = m_R - im_I$	- *
Real part of m	m_R	-	-
Imaginary part of m	m_I	-	-
Dielectric factor	K	$(m^2-1)/(m^2+2)$	-
Dielectric factor of water	K_w	-	-
Mass density	ρ	-	g/cm^3
Drop diameter	D	-	mm
Scattering cross section	σ_s	-	m^2
Absorption cross section	σ_a	-	m^2
Total cross section	σ_t	$\sigma_t = \sigma_s + \sigma_a$	m^2
Back scattering cross section	σ_b	-	m^2
Drop size distribution (DSD)	$N(D)$	-	mm^{-1}/m^3
Falling velocity	$\nu(D)$	-	m/sec
nth moment of DSD	M_n	$\int D^n N(D)dD$	mm^n/m^3
Radar reflectivity	η	$\int \sigma_b(D)N(D)dD$	m^{-1}
Radar reflectivity factor	Z	$\int D^6 N(D)dD$	mm^6/m^3
Effective radar reflect. factor	Z_e	$10^{18}\lambda^4\pi^{-5}\lvert K_w\rvert^{-2}\int \sigma_b(D)N(D)dD$	mm^6/m^3
Rainfall rate	R	$0.0006\pi \int \nu(D)D^3N(D)dD$	mm/hour
Attenuation coefficient	k	$4343\int \sigma_t(D)N(D)dD$	dB/km
Liquid water coefficient	W	$\rho\pi/6\times10^{-3}\int D^3N(D)dD$	g/m^3
Optical extinction	Σ	$\pi/2\times10^{-3}\int D^2N(D)dD$	km^{-1}

"m" is also used for a parameter of gamma dropsize distribution.

scattering and absorption cross sections of a particle, dielectric constant, size distribution of particles, and various integral rainfall parameters. Table 4.1 lists those parameters and their units used in this note. Although the units used here are very common, it should be noted that they are not unique. Care should be given to the difference in the units in comparing the results of this text to the results of other papers. More discussions on those parameters follow.

4.1.2 Dielectric constant

The dielectric constant, ε, is a fundamental parameter to characterize the attenuation and scattering properties of hydrometeors. It is often expressed as a value relative to that of free space, ε_0 ($= 8.854\times10^{-12}$ F/m). The relative dielectric constant ε_r ($= \varepsilon/\varepsilon_0$) is related to the complex index of refraction, m, by $m^2 = \varepsilon$. The ε_r or m of water and ice can be calculated if the temperature is given. The result by Ray[1] is shown in Table 4.2. For general nonliquid hydrometeors which are composed of water, ice and air, however,er depends also on the mixing situation of the particle. Several formulae have been proposed to calculate the er of such mixed hydrometeors, a discussion of which is found in Meneghini and Kozu[2]. In this text, Wiener's formula[3], [4] will be employed to calculate the ε_r of the bright band particles.

4.1.3 Scattering, absorption and attenuation cross sections of a hydrometeor

The scattering, absorption and attenuation (or total) cross sections (σ_s, σ_a, and σ_t respectively) of a single hydrometeor are dependent on the dielectric constant of the particle, particle size and shape, and the wavelength and polarization of the incident wave. Hydro-meteors can be approximated as spherical or deformed (oblate spheroid or Pruppacher-Pitter[5] form) drop models. In most non-polarimetric radar measurements, the assumption of spherical shape may be sufficient[6]. The cross section of a spherical particle can be calculated with the Mie theory. A description of the Mie theory can be found in a number of text books (*e.g.* Stratton[7]). Scattering coefficients of deformed drops have been calculated by employing several techniques such as point-matching and least-square fitting methods, spheroidal function expansion methods, and T-matrix methods [8][9]. Since the symmetry axes of falling raindrops are aligned along the vertical direction on average, the spherical particle model may be used for the study of down-looking radar measurements.

According to the Mie theory, the scattering, absorption and total cross

Table 4.2: Complex refractive indices of water and ice

Frequency	Temperature	m_R	m_I	$\|K\|^2$
5.33 GHz	30°C	8.576	0.962	0.9249
	20°C	8.650	1.265	0.9279
	10°C	8.625	1.668	0.9307
	0°C	8.423	2.175	0.9332
	0°C (ice)	1.782	.003636	0.1767
10.00 GHz	30°C	8.185	1.649	0.9241
	20°C	8.032	2.059	0.9267
	10°C	7.682	2.507	0.9287
	0°C	7.087	2.907	0.9298
	0°C (ice)	1.781	0.002324	0.1764
13.80 GHz	30°C	7.786	2.066	0.9232
	20°C	7.465	2.462	0.9251
	10°C	6.938	2.815	0.9261
	0°C	6.221	3.034	0.9255
	0°C (ice)	1.781	.001848	0.1764
17.25 GHz	30°C	7.405	2.341	0.9221
	20°C	6.972	2.680	0.9234
	10°C	6.361	2.922	0.9232
	0°C	5.621	3.002	0.9205
	0°C (ice)	1.781	.001576	0.1764
24.15 GHz	30°C	6.684	2.661	0.9193
	20°C	6.133	2.851	0.9187
	10°C	5.482	2.902	0.9154
	0°C	4.791	2.802	0.9076
	0°C (ice)	1.780	.001241	0.1760
34.50 GHz	30°C	5.805	2.799	0.9137
	20°C	5.233	2.803	0.9093
	10°C	4.637	2.685	0.8998
	0°C	4.057	2.464	0.8819
	0°C (ice)	0.1789	.0009626	0.1760

sections, σ_s, σ_a, and σ_t are given by

$$\sigma_s = \lambda^2/(2\pi)\Sigma(2n+1)(|a_n|^2 + |b_n|^2) \quad (4.1)$$
$$\sigma_t = -\lambda^2/(2\pi)\Sigma(2n+1)\mathrm{Re}[a_n + b_n] \quad (4.2)$$
$$\sigma_a = \sigma_t - \sigma_s \quad (4.3)$$

where λ is the wavelength in the background medium. The expansion coefficients a_n and b_n are called Mie coefficients, and are expressed in terms of spherical Bessel functions and Hankel functions of the second kind with arguments χ ($= 2\pi r/\lambda$, being the radius of the particle) and the relative complex dielectric constant, ε_r. The a_n and b_n represent the scattered fields arising from the induced magnetic dipoles, quadrupoles, etc. and electric dipoles, quadrupoles, etc., respectively. Similarly, the Mie backscattering cross section, σ_b, is given by

$$\sigma_b = \lambda^2/(4\pi)|\Sigma(-1)^n(2n+1)(a_n - b_n)|^2 \quad (4.4)$$

4.1.4 Rayleigh approximation

Much simplification is possible in the above expressions of σ_s, σ_a, σ_t and σ_b, when the particle size is much smaller than the wavelength λ, which is known as the Rayleigh approximation. With this approximation, σ_s, σ_a, σ_t and σ_b are expressed as

$$\sigma_s = 2/3(\pi^5/\lambda^4)D^6|K|^2 \quad (4.5)$$
$$\sigma_a = (\pi^2/\lambda)D^3\mathrm{Im}[-K] \quad (4.6)$$
$$\sigma_t = \sigma_s + \sigma_a \quad (4.7)$$
$$\sigma_b = (\pi^5/\lambda^4)D^6|K|^2 \quad (4.8)$$

with

$$K = (\varepsilon_r - 1)/(\varepsilon_r + 2) \quad (4.9)$$

where D (= 2r) is the diameter of the particle.

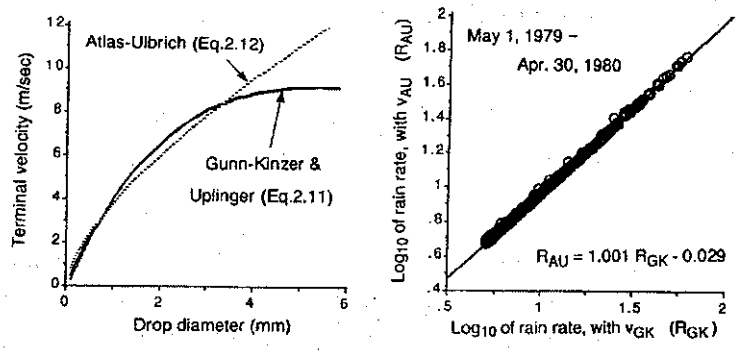

Figure 4.1: Terminal fall velocity of raindrops using different equations, and comparison of rain rates calculated from ground-measured DSDs using terminal velocities $\nu_{Up}(D)$ and $\nu_{AU}(D)$.

A criterion of the diameter range where the Rayleigh approximation is valid is $|\sqrt{\varepsilon_r \chi}| < 0.5$ [10]. Eqs. 4.5 through 4.8 state that σ_s and σ_b are proportional to D^6, while σ_a is proportional to D^3 in the Rayleigh region. Because of the difference between the particle size dependences of σ_s and σ_a, σ_a is generally much greater than σ_s (*i.e.*, $\sigma_t \approx \sigma_a$) when $D \gg \lambda$. The dielectric factor, K, for water (hereafter K_w) is later used to define the effective radar reflectivity, Z_e:

$$K_w = (\varepsilon_r - 1)/(\varepsilon_r + 2), \tag{4.10}$$

with ε_r for water.

4.1.5 Terminal fall velocity

Rain rate is among the rain parameters most often required from meteorological, hydrological and cloud physics studies. Since rain rate is the downward flux of water, it is essential to know the terminal fall velocity of hydrometeors. Gunn and Kinzer[11] data have widely been used as the

raindrop terminal velocity at the ground. The height or air density dependence of the terminal velocity can be simply expressed by the factor $(\rho(0)/\rho(z))^{0.4}$, $\rho(z)$ being the air density at height z, multiplied to the Gunn-Kinzer velocity, $\nu_{GK}(D)$, which was given by Foote and du Toit[12]. It is sometimes convenient to approximate $\nu_{GK}(D)$ by an analytic function. In this text, we use the following two functions:

$$\nu_{U_p} = 4.854D\exp(-0.195D) \tag{4.11}$$

$$\nu_{AU}(D) = 3.778D^{0.67} \tag{4.12}$$

where the velocity is in m/sec and the drop diameter is in millimeters. A comparison of ν_{GK}, ν_{U_p} and ν_{AU} is shown in Fig. 4.1. The former, proposed by Uplinger[13], gives an excellent fit over the entire drop diameter range up to about 5.5 mm and will be used to calculate the rain rate from measured and theoretical DSDs. The latter, proposed by Atlas and Ulbrich[14], gives a less accurate fit than the former; however, we will employ it in making approximate comparative analyses between rain rate and other rain parameters, since with $\nu_{AU}(D)$ rain rate is expressed as a quantity proportional to the 3.67th moment of the DSD. In order to evaluate the validity of $\nu_{AU}(D)$, rain rates are calculated from DSDs measured on the ground using $\nu_{AU}(D)$ and $\nu_{GK}(D)$. The result, also shown in Fig. 4.1, indicates that $\nu_{AU}(D)$ is sufficient for the purpose mentioned above.

4.1.6 Drop size distribution (DSD)

a. Importance of knowledge of DSD

The size distribution of precipitation particles (DSD) is a fundamental precipitation parameter by which all integral rain parameters (IRPs, see section 4.1.7 and relationships among them are characterized. Because the direct radar measurable, radar reflectivity, is approximately proportional to the 6th moment of the DSD and different from the other IRPs of interest, knowledge of the DSD is essential to make an accurate radar estimation of IRPs. It is known that DSD is highly variable[15]-[18]. Examples of such

DSD variation are shown in Fig. 4.2, which were measured on the ground by a disdrometer. It changes from time-to-time and from one rain event to another. Although there have been numerous studies to understand, to parameterize and to estimate the DSD, large uncertainties remain in temporal and spatial DSD variabilities and their dependence on rainfall type and climatological regimes.

b. DSD models

Although natural DSDs are highly variable, three-parameter models such as gamma and lognormal models are known to fit the natural DSDs well. Two-parameter models are less flexible but still provide good fitting to the natural DSD's in a limited domain. They are considered to provide sufficient accuracy to relate rainfall parameters of practical interest such as radar reflectivity, rain rate, LWC and microwave attenuation[18], [19]. The reason is that all of those rain parameters are mainly determined by distributions at intermediate to large drop diameters and therefore variations in distributions at small drops can be neglected. The DSD model most frequently used to date is the gamma distribution:

$$N(D) = N_o D^m \exp(-\Lambda D) = N_T \frac{\Lambda^{m+1} D^m}{\Gamma(m+1)} \exp(-\Lambda D) \tag{4.13}$$

where $[N_0,\ m,\ \Lambda]$ or $[N_T,\ m,\ \Lambda]$ are parameters of the gamma model. Although N_T is the zeroth moment of the DSD modeled as gamma, we treat it also as a DSD parameter that can be used in place of N_0[20]. The parameter m is often fixed for simplicity and for making it possible to estimate the DSD from dual-parameter radar measurements. The exponential distribution is a special case ($m = 0$) of the gamma distribution and expressed as

$$N(D) = N_0 \exp(-\Lambda D) = N_T \Lambda \exp(-\Lambda D) \tag{4.14}$$

where $[N_0,\ \Lambda]$ or $[N_T,\ \Lambda]$ are parameters of the exponential model.

Another DSD model that is sometimes employed is the lognormal dis-

tribution

$$N(D) = \frac{N_T}{\sigma D\sqrt{2\pi}} \exp\left(-\frac{(\ln D - \mu)^2}{2\sigma^2}\right) \tag{4.15}$$

where $[N_T, m, \sigma]$ are parameters of the lognormal model. Similar to the m parameter of the gamma model, the parameter s is often fixed[17],[21].

The other problem in the DSD modeling is to characterize the spatial or temporal variation in DSD. For example, the Marshall-Palmer (MP)[22] DSD model

$$N(D) = N_0 \exp(-\Lambda D), \quad \text{with} \quad N_0 = 8000 \quad \text{and}\Lambda = 4.1R^{-0.21} \tag{4.16}$$

assumes that N_0 is constant and Λ is related to rain rate R by a negative power law. Similar DSD models were proposed by Joss *et al.*[15]:

$N_0 = 1400$ and $\Lambda = 3.0R^{-0.21}$	Joss-thunderstorm (J-T)
$N_0 = 7000$ and $\Lambda = 4.1R^{-0.21}$	Joss-widespread (J-W)
$N_0 = 30000$ and $\Lambda = 5.7R^{-0.21}$	Joss-drizzle (J-D).

It has been reported that the MP model fits well to natural DSDs if a large number of DSDs are averaged inspite of the large fluctuation in short term DSDs[18],[23]. Since the Z factor or rain rate dependences of the DSD parameters are closely related to the relationships among various rain parameters, it is important to investigate such DSD fluctuation properties. In comparison to the modeling of individual DSDs, the number of studies concerning this problem is relatively small. Although there are many papers concerning the relationships among rainfall parameters (especially the Z-R relation) [24],[25] and although it is well known that such IRP relations are formed as a result of DSD variations, a relatively limited number of papers give a quantitative discussion on the relation between "DSD variation" and the "relation between two rainfall parameters"[26],[27].

4.1.7 Integral rainfall parameters (IRP)

As shown in Table 4.1, most of the rain parameters of scientists' and communications engineers' interest are defined as the integral of the product of

a "kernel", $\kappa(D)$, and DSD, $N(D)$, over the drop diameter, D:

$$\text{IRP} = \int_0^\infty \kappa(D)N(D)dD \tag{4.17}$$

Such quantities are called "integral rainfall parameters (IRP)". A major task of radar rainfall measurement is to estimate IRPs of interest from IRPs directly obtained from radar measurements. (Note that the IRP can be defined regardless of particle phase even though we call it Integral "Rain" Parameter.) The IRPs most important for the radar rainfall measurement include radar reflectivity factor Z, effective radar reflectivity factor Z_e, attenuation coefficient k, rain rate R, and liquid water content W, which are defined in Table 4.1.

For making studies of the IRPs and DSD, it is convenient to approximate the IRPs by the xth moment of DSD, M_x, which is defined by

$$M_x \equiv \int_0^\infty D^x N(D)dD \tag{4.18}$$

and expressed as the following equations for gamma and lognormal DSD models

$$M_{x,\text{gamma}} = N_0 \frac{\Gamma(m+x+1)}{\Lambda^{m+x+1}} = N_T \frac{\Gamma(m+x+1)}{\Lambda^x \Gamma(m+1)} \tag{4.19a}$$

$$M_{x,\text{lognormal}} = N_T \exp\left(x\nu + \frac{1}{2}x^2\sigma^2\right) \tag{4.19b}$$

where x may be non-integer. In Table 4.3, such moment approximations are summarized. In the case of the moment approximation of the attenuation coefficient, the order of the moment, x, depends on frequency. Around 10 GHz, x takes a maximum value of about 4.5. With decreasing or increasing frequency, x decreases due to the increasing contribution of σ_a to σ_t at lower frequency and due to the increasing Mie scattering effect at higher frequency. Figure 4.2 shows regression results of the relation between logarithms of σ_t and D at several frequencies, from which the x value is obtained. The x value close to 3.67 at 35 GHz indicates that the attenuation measurements at around this frequency should provide accurate rain rate estimates.

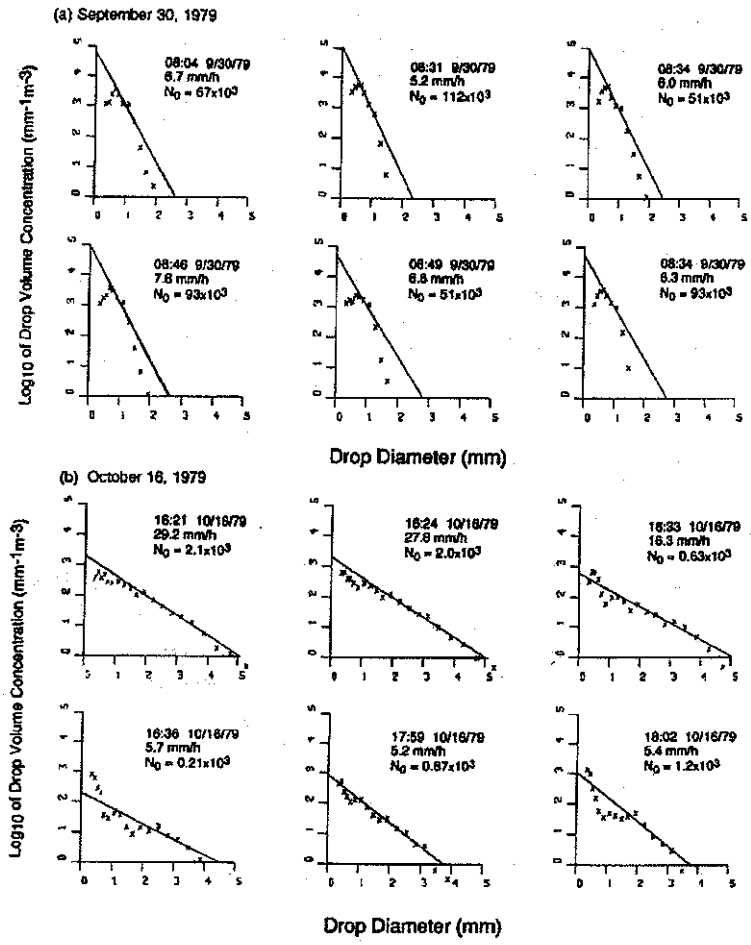

Figure 4.2: Examples of natural DSD measured by a disdrometer. Solid line represents an exponetial model fit using a moment method.

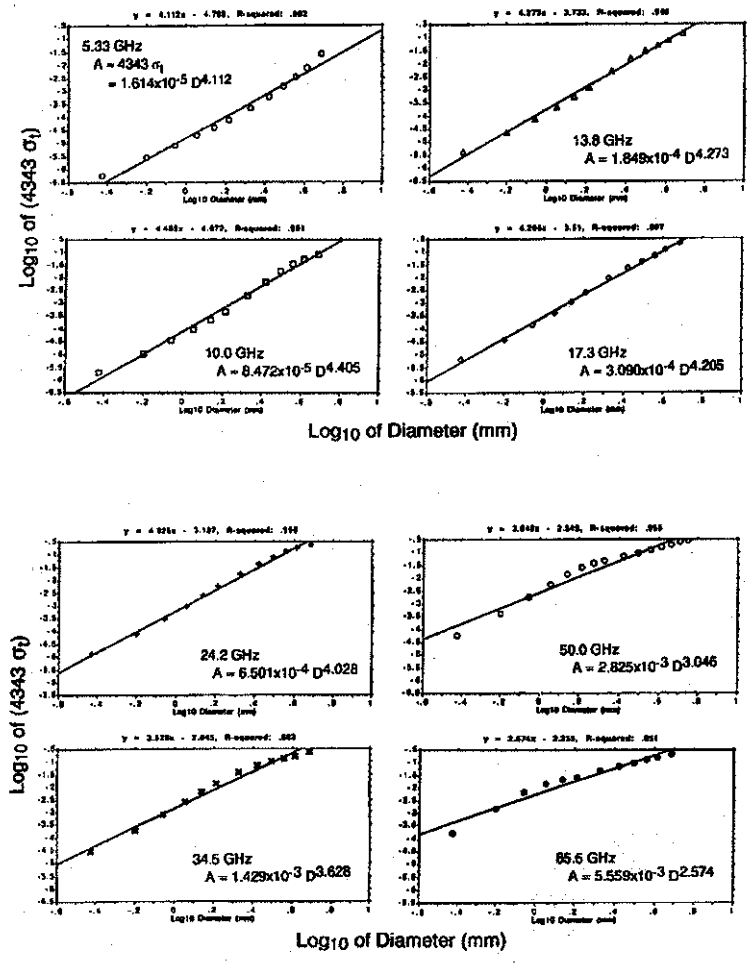

Figure 4.3: Regression results of the relation between logarithms of σ_t and D. Note that the exponent shifts with freuency and that $A = 4343\ \sigma_t$.

Table 4.3: Moment approximation of typical IRPs (IRP = CM_n).

Integral rain parameter	n	C	Unit.
Radar reflectivity factor, Z	6	1	mm^6/m^3
Effective radar reflect. factor, Z_e	~6	1	mm^6/m^3
Rainfall rate, R	3.67	$6\times3.78\pi\times10^{-4}$	mm/hour
Attenuation coefficient, k	3~4.5	$4343C_k$	dB/km
Liquid water content, W	3	$\rho\pi/6\times10^{-3}$	g/m^3
Optical extinction, S	2	$\pi/2\times19^{-3}$	km^{-1}

4.1.8 Melting layer (Bright band)

The information of thermodynamic phase is essential for accurate rainfall retrievals. The melting layer, at which frozen hydrometeors melt into rain, is very clearly seen by radar in stratiform rain. Because the melting process causes a clear enhancement in radar reflectivity for frequencies approximately less than 20 GHz, the melting layer is often called the "bright band"[25]. For convective storms, it is generally difficult to identify where the melting occurs because of the strong updrafts in the cloud, unless multi-frequency or polarimetric radars are employed. In this sense, stratiform rain is easier to model than convective storms. Examples of radar reflectivity profiles for stratiform and convective storms are illustrated in Fig. 4.4.

During a stationary stratiform rain, it may be reasonable to assume that the water flux (*i.e.*, rain rate) is constant from the top to the bottom of the storm. This assumption may be extended up to the bright band if water vapor condensation mainly occurs above the bright band and if evaporation has little effect on the flux.

Even with this constraint, there are many parameters characterizing the bright band in terms of scattering and attenuation properties. Those include drop size distribution, falling velocity, particle shape, orientation and dielectric constant. A number of bright band models have been proposed to date[28]-[32]. Because the shape of melting particles may be highly ir-

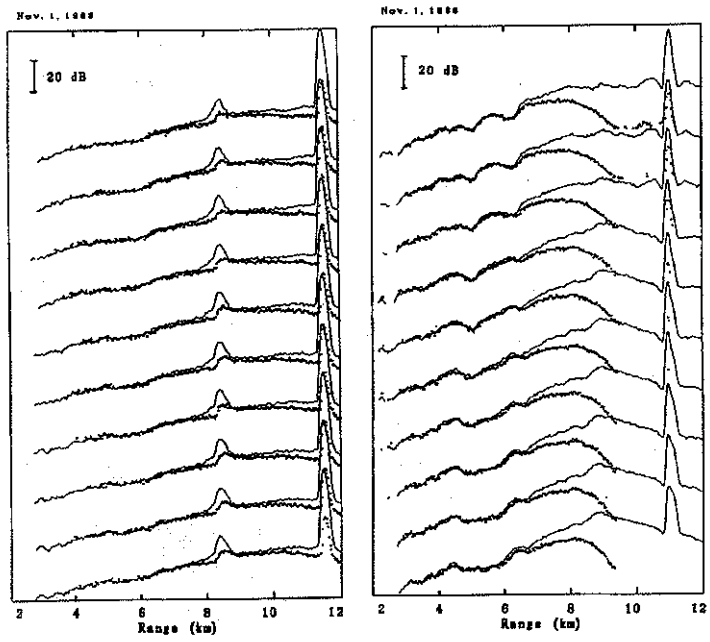

Figure 4.4: Examples of vertical radar reflectivity profile. Left: stratiform, and right: convective. Solid line and heavy dotted line represent X-band (10 GHz) and Ka-band (34.5 GHz) radar reflectivity factors including attenuation, respectively. The sharp spike at around 11–11.5 km is the surface return.

regular, it is almost impossible to know the shape of each particle, shape distribution and orientation precisely. As a first approximation, therefore, spherical or spheroidal particle models have been used to calculate the scattering properties.

Although there are two types of bright band particle model (concentric two-layer sphere and composite dielectrics models), no conclusion has been obtained as to which is better. These models have been studied by Awaka *et al.*[30]. They compared the N/N model with a modified Nishitsuji (M-N) model[4] in terms of the agreement with measured C-band Z factor profiles. Their conclusion is that the M-N model, which is considered to take physical processes in the bright band into account empirically, appears to be superior to the N/N model in the upper portion of the bright band. For the lower region of the bright band, however, the differences between the two models are small and both models show good agreement with the measured profile. Since the major issue of the brightband in radar rainfall measurement is to estimate the attenuation that would occur in the lower portion of the bright band, for simplicity, the N/N model may be used for the retrieval of the bright band together with a composite dielectrics model for individual particles.

4.1.9 Storm structure

In order to develop rainfall retrieval algorithms using a limited number of remote sensing data, the use of a proper storm structure model is required and it should be as simple as possible while keeping a reasonable representation of microphysical phenomena. For example, vertical storm models used for passive microwave rainfall retrieval to date consist of one uniform rain region plus one or several ice and ice+rain mixing layers. The melting layer or bright band that is a distinct radar precipitation signature has been omitted in the passive rainfall sensing to simplify radiative transfer computations [33],[34].

The radar, which has a capability of profiling, does not require such a simplification for vertical structure models. Yet, knowledge of the storm structure is required to understand the radar signatures and estimate vari-

ous precipitation parameters adequately, and to evaluate the effect of non-uniform beam filling on the accuracy of the algorithm. The modeling of stratiform type rain is fairly easy because of the existence of a clear bright band; rainfall is horizontally uniform and understanding the vertical structure would suffice for most purposes. On the other hand, convective type storms are more difficult to model because the strong updraft causes the mixing of different hydrometeors such as supercooled water drops, ice and melting particles, and because the horizontal variability in rainfall is much larger than that of stratiform rain.

More generally, the modeling of a storm can be recognized as a parameterization of three dimensional (3-D) storm structure. Although individual storm structure is far more complicated than can be modeled by a reasonable number of parameters, at least statistically, extensive simplification should be possible. Several simplified 3-D models have been proposed in the field of microwave propagation studies and passive microwave rainfall retrievals. They have uniform or simply stratified vertical structures and rotationally symmetric[35], or rectangular horizontal structures[36]. Although they should be adequate for approximate estimation of the effect of non-uniform beam filling and for making radiative transfer models, more precise models depending on the type of storm system (tropical convection, wide spread rain associated with warm front, etc.) would be required for more realistic simulation of spaceborne or airborne radar measurements.

4.2 Basic Theory of Radar Rainfall Measurement

4.2.1 Scattering and attenuation of radiowaves by hydrometeors

In section 4.1.3, we have considered the scattering and attenuation by a single hydro-meteor. In practice, there are many such particles having various sizes and distributed random-ly in space. Because of the randomness of the phases of scattered waves from particles, total scattered power is the incoherent sum of powers from individual particles. Thus, the radar equation that relates the radar received power from the hydrometeors in a

radar resolution volume can be expressed as a sum of the received power derived from the radar equation for a single hydrometeor. The radar and scattering conditions we consider here are: monostatic radar, linear and copolarized signal, and the presence of rain attenuation to and from the radar resolution volume of interest. In such cases, the radar equation expressed as an integral of powers from the infinitesimal volume of $d\Omega dr$, Ω and r being solid angle and range, respectively, is given by

$$P_r(t) = \frac{\lambda^2 P_t}{(4\pi)^3} \int \frac{G^2(\Omega)\eta(r,\Omega)\mathrm{e}^{-2\gamma(r,\Omega)}}{\nu r^2} |u(t-2r/c)|^2 d\Omega dr \tag{4.20}$$

where λ is the radar wavelength, P_t is the peak transmitted power, G is the one-way antenna gain, $u(t)$ is the complex envelope of the transmitted pulse normalized to have a peak amplitude of unity. η and γ are radar reflectivity and optical depth of rain, respectively, which are givenby

$$\eta = \int_0^\infty \sigma_b(D)N(D)dD = \pi^5 |K_w|^2 \lambda^{-4} Z_e \tag{4.21}$$

$$\gamma(r) = 0.1 \ln 10 \int_0^r k(s)ds \tag{4.22}$$

where the definitions of the quantities used in Eqs. 4.21 and 4.22 are given in Table 4.1.

The following approximations hold for most cases: (1) Most of the transmitted energy is concentrated in a narrow main beam so that the radar reflectivity and rain attenuation are independent of angular variations; (2) The Antenna gain pattern is given by a two-dimensional Gaussian function and sidelobe contributions to the received power can be neglected. With these approximations, Eq. 4.20 becomes

$$P_r(t) = \frac{C|K_w|^2}{r^2} Z_e \exp\left(-0.2 \ln 10 \int_0^r k(s)ds\right) = \frac{C|K_w|^2}{r^2} Z_m \tag{4.23}$$

with

$$C = \frac{\pi^3 P_t G_0^2 \theta_B^2 c\tau}{1024 \ln 2 \lambda^2} \tag{4.24}$$

where G_0 is the peak antenna gain, θ_B is the half-power antenna beamwidth, c is the speed of light, and τ is the transmitted pulse width. For convenience, the "apparent" or "measured" effective radar reflectivity factor, Z_m, is also introduced. Z_m is recognized as an estimate of Z_e using a radar equation neglecting rain attenuation. Since Z_m can be estimated with the radar sys-tem parameters only, it is convenient to begin the rain parameter estimation with this quantity.

Difference in Z_e values between spherical and deformed drop models

Since the present study concerns radar observations using near-nadir incidence angles at which there is little polarization difference in scattering properties, it may be sufficient to use the spherical model. Mie theory may then be used to calculate all scattering and attenuation cross sections, which makes the calculation much easier than that for the deformed drop models. However, it may be required to check the difference between the spherical and deformed drops having the same volume, because the effective diameter of the deformed drop is larger than that of the spherical drop when the drop is seen from down or upward. For this purpose, comparisons are made for Z_e factors calculated from the spherical and deformed (Pruppacher-Pitter) drops. For the calculation of the deformed drop case, we use the result from Oguchi's point-matching-and-least-squares method[37], (M. Satake, private communication). Since Z_e is approximately proportional to the 6th moment and puts the largest weight on the large drops among the IRPs of interest, it should be sufficient to check the difference in Z_e. The result is shown in Fig. 4.5 for 10 GHz and 35 GHz. It is found that the differences in Z_e factors (in dB unit) increase with rain rate to some extent depending on frequency and DSD. It appears, however, that the difference is minor incomparison to the large variation in DSD that causes large fluctuations in Z_e-R and k-Z_e relations, and that it can approximately be treated as a constant bias of several tenths of a decibel.

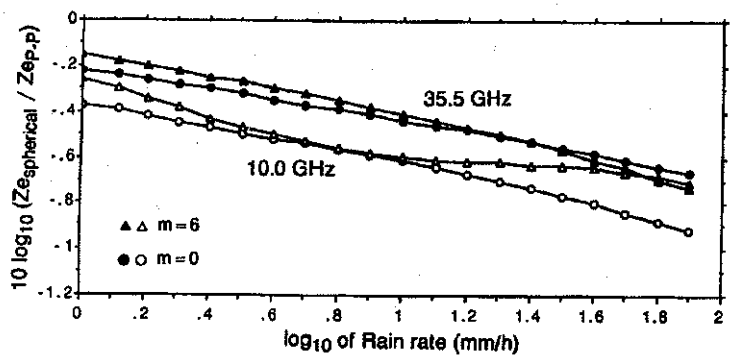

Figure 4.5: Difference in Z_e factors of the spherical drop model and the deformed drop model at 10 GHz and 35.5 GHz assuming the two-parameter gamma DSD models given in Table 4.2, with $m = 0$ and $m = 6$.

4.2.2 Estimation of meanreceived power and radar reflectivity

Since the hydrometeors in a radar resolution volume are randomly distributed and fluctuating randomly, the radar precipitation return shows large fading due to the interference among return signals from each scatterer. The quantity that should be obtained by a radar precipitation measurement is the radar received power, P_r, that is defined by the radar equation described above; the sum of received powers from individual scatterers. The most common method to estimate P_r is to use the average of the fluctuating instantaneous received signal level. For the estimation, some assumptions are usually employed: (1) The fluctuating return signal is ergodic so that both ensemble and time averaging can be used; and (2) many small scatterers are randomly distributed in a resolution volume which is much larger in size than the radar wavelength, so that the phase of the composite return signal is uniformly distributed over 0 to 2π and the amplitude is Rayleigh distributed.

It follows from the assumption (2) that the instantaneous return power, P, is exponentially distributed; *i.e.* the probability density function (pdf) of P, $p(P)$, is given by

$$p(P) = P_r^{-1} \exp(-P/P_r). \tag{4.25}$$

The exponential pdf has a standard deviation equal to the mean value P_r and therefore the estimation of P_r from a single measurement suffers from a large error. In order to reduce the estimation error, many statistically independent samples should be averaged. The averaging is made after the detection of IF signal. The pdf of the averaged video signal depends on the type of detection. For a square-law detection, the pdf of the average of N independent video signals, $p_N(\xi)$, can be written in the form of the χ-squared distribution with $2N$ degrees of freedom[38]:

$$p_N(\xi) = \frac{N^N \xi^{N-1}}{P_r^N (N-1)!} \exp(-N\xi/P_r), \quad \xi = N^{-1} \Sigma_{i=1}^N P_i \tag{4.26}$$

so that the expectation (E(.)) and variance (Var(.)) of ξ are P_r and P_r^2/N, respectively.

For the logarithmic detection that is frequently employed to increase the dynamic range, the pdf of the average of $\log_{10}(P/P_r)$, $p_{LN}(\zeta)$, is approximated by[39]

$$p_{LN}(\zeta) = \frac{aN[N(a-b)\zeta]^{3N-1}}{(3N-1)!} \exp[-N(b-a\zeta)], \quad \zeta = N^{-1} \Sigma_{i-1}^N \log(P_i/P_r) \tag{4.27}$$

where $a = 3.13$, $b = 2.215$. It is shown that $E(z)$ is about -0.25; *i.e.*, the mean of the log-converted power is 2.5 dB smaller than the log of the true mean, Pr. Thus, a correction of 2.5 dB is needed in the radar equation when logarithmic detection and averaging are employed, whereas, the standard deviation of ζ is approximated by $0.557/\sqrt{N}$[40].

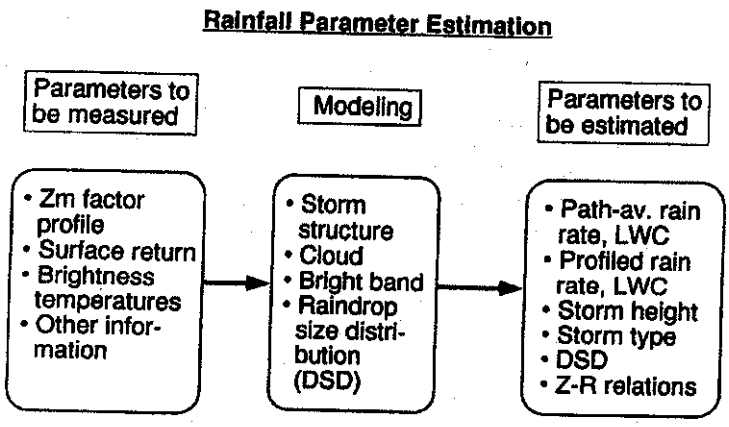

Figure 4.6: Concept of rain parameter estimation by means of remote sensing techniques.

4.3 Rainfall and DSD Parameter Estimation

4.3.1 General discussion

The concept of "rainfall remote sensing", which is to estimate various rainfall param-eters of interest from remote sensing techniques, is shown in Fig. 4.6. The rainfall parameters to be estimated include rain rate, LWC, microwave attenuation, storm height, horizontal storm area, etc. The rain parameters to be measured include radar reflectivity, microwave/millimeter wave attenuation and brightness temperatures, differential Z_e (ZDR), differential phase shift, etc. For the estimation, it is common to model rainfall scene characteristics such as storm structure, DSDs (rain, bright band, and snow regions), fall velocity, etc. Techniques to be employed are closely related to the requirements such as accuracy and spatial/temporal resolutions. For example, if only rainfall or rain rate statistics for a long period (*e.g.* a month) or a wide area are required, statistical properties of rainfall can be utilized in estimation techniques, which should reduce the difficulty in comparison to the estimation of instantaneous rain rate profiles[41],[42].

In the case of radar measurements, it is the most basic problem to estimate rainfall parameters in a radar resolution volume which is approximately several hundred meters in range and several kilometers in horizontal dimension. Development of rainfall parameter estimation techniques with fine temporal/spatial resolutions is important, because the fine resolution rainfall mapping is a basis to understand large scale rainfall statistical properties and is essential for various climatological studies, short range weather forecasts, and other cloud/rainfall microphysics. In this text, therefore, explanations are given to the rainfall parameter estimation with high spatial/temporal resolution.

In the following, rainfall and DSD parameter estimation methods are classified in terms of the number of measurable rain parameters; single, dual and multi-parameter measurements. Methods to estimate rainrate by spaceborne radar measurements are also reviewed briefly and classified in this manner.

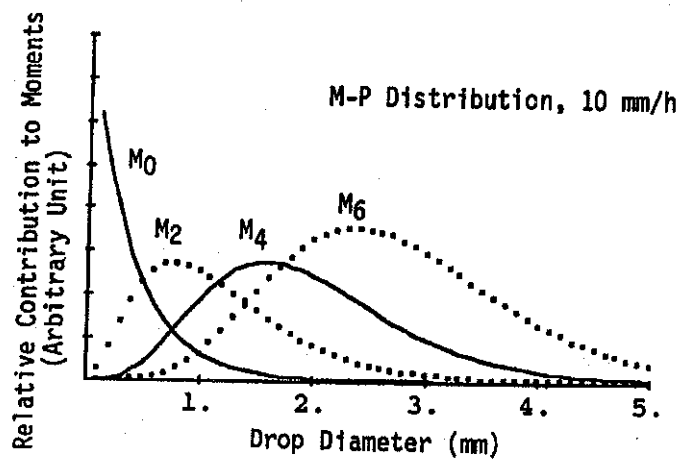

Figure 4.7: Distributions (weighting functions) for several moments of DSD.

4.3.2 Single-parameter (SP) measurements

The conventional way to estimate rain rate and LWC, W, is to use empirical relationships between Z and R and between Z and W. Such methods are regarded as Single-Parameter (SP) measurements. In general, the SP measurement can be defined as estimating IRPs from a "single" IRP. Because of the difference in the weighting functions, the relationships between Z and other IRPs depend on the DSD (see Fig. 4.7). From the DSD parameter estimation point of view, the SP measurement has an ability to estimate only one DSD parameter. Since at least two parameters are required to express reasonably the natural DSD, it is anticipated that the SP measurement has a limited capability to estimate IRPs. If one can measure an IRP that has a kernel close to that of the IRPs to be estimated, estimating the two DSD parameters is not so essential to obtain sufficient accuracy; *e.g.* estimating rain rate from Ka-band ($\gg$ 35 GHz) attenuation[14]. However, such measurement can notalways be accomplished.

4.3.3 Dual-parameter (DP) andmulti-parameter measurements

The terms "dual-parameter" and "multi-parameter" have been used in various measurement configurations. For example, Doviak and Zrnic[43] describe the combination of a ground-based radar and raingage(s) set up far from the radar as one of the dual-parameter measurements. Atlas *et al.*[19], Rogers[44] andHall[45] review various methods including dual-frequency, dual-polarization,Doppler, path-integrated microwave or optical attenuation and radiometry. In short, adding another measurement other than the radar reflectivity maybe called a "dual-parameter measurement". In this text, however, the terminology of the single-, dual- andmulti-parameter measurements is redefined from the DSD parameter estimation (for a given spatial or temporal resolution) point of view, which is recognized as a narrow-sense definition and will make the discussion of the methods clear.

The basic concept (the narrow sense) of dual-parameter (DP) and multi-parameter rain measurements have been explored by Ulbrich and Atlas[19]. The terms "dual" and "multi" correspond to the number of "independent" IRPs to be measured. From such multiple meas-urements, DSD parameters can be estimated. Such estimation processes are known as "inversion techniques", and there are many applications such as retrievals of temperature profiles from microwave radiometers around an O_2 absorption line, of cloud dropsize spectra from multi-wavelengths/incidence angle lidar measurements. For DSD estimation, Furuhama and Ihara[46] succeeded to estimate the path-averaged DSD from multi-frequency attenuation measurements. For those methods, several inversion techniques such as Phillips-Twomey method (PTM) and Backus-Gilbert method (BGM) may be applied[47]. Those techniques have been employed to stabilize the result of the inversion because the inversions mentioned above are so-called "ill-posed" problems. Differences between the above applications and the multi-parameter measurements using radar are that the latter is not necessarily "ill-posed", and that the number of measurable independent rain parameters is very limited. Because of these facts in the dual- and multi-parameter radar measurements, the usual way to make the inversion is to

solve simultaneous equations analytically or numerically. Of course, it is necessary to employ some averaging scheme in order to avoid a noisy result in the DSD estimation. The dual-polarization radar combining Z_e and Z_{DR} [19],[43]-[45],[48],[49] and the dual-frequency method studied by Goldhirsh and Katz[2],[43],[50] are typical examples of the DP measurement.

4.3.4 Semidual-parameter measurement

The "semi" dual-parameter (SDP) measurement can be defined to generalize the concept of SP and DP measurements in terms of the resolutions of measurable IRPs and those of the DSD parameters to be estimated. The SDP measurement is defined as DP measurements in which one of the rain parameters to be measured has a spatial or temporal resolution coarser than that required. Various methods to improve the estimation accuracy of the Z-R method can be classified as SDP measurements. For example, the calibration of Z-factor-derived rain rate by comparing with rain gage data is an SDP measurement in which the rain gage data has a resolution much coarser than that of the Z-factor measurement. The adjustment of Z-R relations for each rain event may be an SDP measurement in which a rain parameter is estimated with the resolution of a storm so as to determine the Z-R relation. Similarly, most of the "dual" parameter measurements proposed for spaceborne radar measurements to date are considered to be of this type.

References

[1] Ray, P. S., 1972: Broadband complex refractive indices of ice and water. *Appl. Optics*, **11**, 1836–1844.

[2] Meneghini, R. and T. Kozu,1990: *Spaceborne weather radar.* Artech House, Norwood, MA, 199pp.

[3] Matsumoto, A. and A. Nishitsuji, eds., 1971: SHF and EHF propagation in snowy districts, *Monograph Ser. of the Res. Inst.of Appl. Electricity*, Hokkaido Univ., (19).

REFERENCES

[4] Nishitsuji, A. and M. Hirayama, 1971: On the anomalous attenuationof radio wave due to snowfall. *Trans. IECE Japan*, **54-B**, 22–29 (in Japanese).

[5] Pruppacher, H.R. and R.L. Pitter, 1971: A semi-empirical determination of the shape of cloud and rain drops. *J. Atmos. Sci.*, **28**, 86–94.

[6] Awaka, J., and T. Oguchi, 1982: Bistatic radar reflectivities of Pruppacher-and-Pitter form raindrops at 14.3 and 5.33 GHz. *J. Radio Res. Lab.*, **29**, (127), 125–150.

[7] Stratton, J.A., 1941: *Electromagnetic theory*, McGraw-Hill, New York.

[8] Oguchi, T., 1981: Scattering from hydrometeors: A survey. *RadioSci.*, **16**, 691-730.

[9] _____, 1983: Electromagnetic wave propagation and scattering in rain and other hydrometeors. *Proc. IEEE*, **71**, 1029–1078.

[10] Ulaby, F.T., R.K. Moore, and A.K. Fung, 1981: Microwave remotesensing: *Active and Passive*. Vol.I. Artech House, Norwood, MA,456pp.

[11] Gunn, K.L.S. and G.D. Kinzer, 1949: The terminal velocity of fall for water droplets in stagnant air. *J. Meteorol.*, **6**, 243–248.

[12] Foote, G.B. and P.S. du Toit,1969: Terminal velocity of raindrops aloft. *J. Appl. Meteor.*, **8**, 245–253.

[13] Uplinger, W.G., 1981: A new formula for raindrop terminal velocity. Preprints, *20th Conf. Radar Meteor.*, Boston, MA, Amer. Meteor. Soc., 389–391.

[14] Atlas, D. and C.W. Ulbrich,1977: Path- and area-integrated rainfall measurement by microwave attenuation in the 1-3 cm band. *J. Appl. Meteor.*, **16**, 1322–1331.

[15] Joss, J., J.C. Thams, and A. Waldvogel, 1968: The variation of raindrop size distribution at Locarono, *Proc. Int. Conf. Cloud Physics*, 369–373.

[16] Waldvogel, A., 1974: The N0 jump of raindrop spectra. *J. Atmos. Sci.*, **31**, 1067–1078.

[17] Feingold, G. and Z. Levin,1986: The lognormal fit to raindrop spectra from frontal convectiveclouds in Israel. *J. Climate Appl. Meteor.*, **25**, 1346–1363.

[18] Kozu, T. and K. Nakamura, 1991: Rainfall parameter estimation from dual radar measurements combining reflectivity profile and path-integrated attenuation. *J. Atmos. Ocean. Tech.*, **8**, 259–270.

[19] Atlas, D., C.W. Ulbrich and R.Meneghini, 1984: The multiparameter remote measurement of rainfall. *Radio Sci.*, **19**, 3–22.

[20] Chandrasekar, V. and V.N. Bringi, 1987: Simulation of radar reflectivity and surface measurements of rainfall. *J. Atmos. Oceanic. Tech.*, **4**, 464–478.

[21] Feingold, G. and Z. Levin, 1987: Application of the lognormal raindrop size distribution to differential reflectivity radar measurement (ZDR). *J. Atmos. Oceanic. Tech.*, **4**, 377–382.

[22] Marshall, J.S. and W.M. Palmer, 1948: The distribution of raindrops with size. *J. Meteorol.*, **5**, 165–166.

[23] Joss, J. and E.G. Gori, 1978: Shapes of raindrop size distributions. *J. Appl. Meteorol.*, **17**, 1054–1061.

[24] Stout, G.E. and E. A. Mueller,1968: Survey of relationships between rainfall rate and radar reflectivity in the measurement of precipitation. *J. Appl. Meteor.*, **7**, 465–474.

[25] Battan, L.J., 1973: *Radar observation of the atmosphere*, The University of Chicago Press, Chicago, 324pp.

[26] Atlas, D. and C.W. Ulbrich,1974: The physical basis for attenuation-rainfall relationships and the measurement of rainfall parameters by combined attenuation and radar methods, *J. Res. Atmos.*, **8**, 275–298.

[27] Ulbrich, C.W., 1983: Natural variations in the analytical form of raindrop size distributions. *J. Climate Appl. Meteor.*, **22**, 1764–1775.

[28] Dissanayake, A.W. and N.J. McEwan, 1978: Radar and attenuation properties of rain and bright band. *IEE Conf. Publ.*, **169**,125-129.

[29] Yokoyama, T., H. Tanaka, K.Nakamura, and J. Awaka, 1984: Microphysical processes of melting snowflakes detected by a two wavelength radar. Part II. Application of a two-wavelength radar technique. *J. Meteor. Soc. Japan*, **62**, 668–677.

[30] Awaka, J., Y. Furuhama, M.Hoshiyama, and A. Nishitsuji, 1985: Model calculations of scattering properties of spherical bright-band particles made of composite dielectrics. *J. Radio Res. Lab.*, **32**, 73–87.

[31] Bringi, V.N., R.M.Rasmussen, and J. Vivekanandan, 1986: Multiparameter radar measurements in Colorado convective storms. Part I: Graupel melting studies. *J. Atmos. Sci.*, **43**, 2545–2563.

[32] Klassen, W., 1988: Radar observations and simulation of the melting layer of precipitation. *J. Atmos. Sci.*, **45**, 3741–3753.

[33] Wilheit, T.T., 1986: Some comments on passive microwave measurement of rain. textitBull. Amer. Meteor. Soc., **67**, 1226–1232.

[34] Kummerow, C., R.A. Mack, and I.M. Hakkarinen, 1989: A self-consistency approach to improve microwave rainfall rate estimation from space. *J. Appl. Meteorol.*, **28**, 869-884.

[35] Capsoni, C., F. Fedi, and A.Paraboni, 1987: A comprehensive meteorologically oriented methodology for the prediction of wave propagation parameters in telecommunication applications beyond 10 GHz. *Radio Sci.*, **22**, 387–393.

[36] Kummerow, C. and J.A. Weinman,1988: Determining microwave brightness temperatures from precipitating horizontally finite and vertically structured clouds. *J. Geophys. Res.*, **93**, (D4), 3720–3728.

[37] Oguchi, T., 1977: Scatteringproperties of Pruppacher-and-Pitter form raindrops and crosspolarization due to rain: Calculations at 11, 13, 19.3 and 34.8 GHz. *Radio Sci.*, **12**, 41–51.

[38] Marshall, J.S. and Hitschfeld,W., 1953: The interpretation of the fluctuating echo for randomly distributed scatterers. Part I. *Can. J. Phys.*, **31**, 962–994.

[39] Kodaira, N., 1960: The characteristics of the averaged echo intensity received by the log arithmic IF amplifier. *8th Weather Radar Conf.*, Amer. Meteor. Soc., Boston, 121–125.

[40] Joss, J., R. Cavalli and R. K. Crane, 1974: Good agreement between theory and experiment for attenuation data. *J. Res. Atmos.*, **8**, 299–318.

[41] Atlas, D., D. Rosenfeld, and D.A. Short, 1990: The estimation of convective rainfall by area integrals, 1. The theoretical and empirical basis. *J. Geophys. Res.*, **95**, (D3), 2153–2160.

[42] Rosenfeld, D., D. Atlas, and D. A. Short, 1990: The estimation of convective rainfall by area integrals, 2. The height-area rainfall threshold (HART) method. *J. Geophys. Res.*, **95**, (D3), 2161–2176.

[43] Doviak, R.J. and D.S. Zrnic,1984: *Doppler radar and weather observations.* Academic Press, Orlando, FL, 458pp.

[44] Rogers, R.R., 1984: A review of multiparameter radar observations of precipitation. *Radio Sci.*, **19**, 23–36.

[45] Hall, M.P.M., 1984: A review of the application of multiple-parameter radar measurement of precipitation, *ibid*, 37–43.

[46] Furuhama, Y. and T. Ihara, 1981: Remote sensing of path-averaged raindrop size distribution from microwave scattering measurements. *IEEE Trans. Antennas. Propag.*, **AP-29**, 275–281.

[47] Ishimaru, A., 1978: *Wave propagation and scattering in random media.* Vol.2., Academic Press, Orlando, FL, 572pp.

[48] Seliga, T.A. and V.N. Bringi,1976: Potential use of radar differential reflectivity measurements at orthogonal polarizations for measuring precipitation. *J. Appl. Meteor.*, **21**, 257–259.

[49] Holt, A.R., 1984: Some factors affecting the remote sensing of rain by polarization diversity radar in the 3- to 35-GHz frequency range. *Radio Sci.*, **19**, 1399–1412.

[50] Goldhirsh, J. and I. Katz, 1974: Estimation of raindrop size distribution using multiple wavelength radar systems. *Radio Sci.*, **9**, 439–446.

Chapter 5

Optical Sensors

Yoshiaki Honda
Center for Environmental Remote Sensing, Chiba Univ.
1-33 Yayoi, Inage-ku, Chiba, 263-8522, JAPAN
Phone: +81-43-290-3835, fax: +81-43-290-3857
E-mail: yhonda@rsirc.cr.chiba-u.ac.jp

This part of the text is extracted from Remote Sensing Note which was published by Japan Association on Remote Sensing (JARS).

5.1 Types of Sensor

Figure 5.1 summarizes the types of sensors now used or being developed in remote sensing. It is expected that some new types of sensors will be developed in the future. Passive sensors detect the reflected or emitted electro-magnetic radiation from natural sources, while active sensors detect reflected responses from objects which are irradiated from artificially generated energy sources, such as radar. Each is divided further in to non-scanning and scanning systems.

Sensors classified as a combination of passive, scanning and imaging are classified further into image plane scanning sensors, such as TV cameras

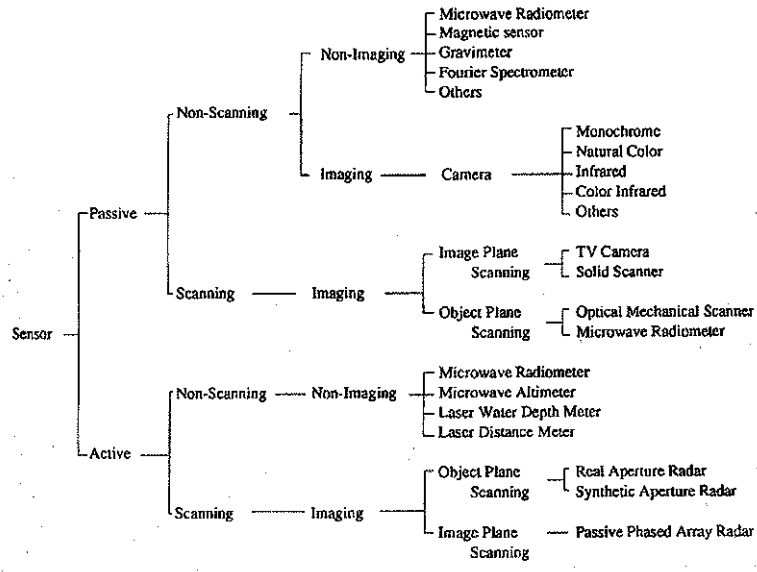

Figure 5.1: Classification od Sensor

and solid state scanners, and object plane scanning sensors, such as multispectral scanners (optical-mechanical scanner) and scanning microwave radiometers.

An example of an active, non-scanning and non-imaging sensor is a profile recorder such as a laser spectrometer and laser altimeter. An active, scanning and imaging sensor is a radar, for example synthetic aperture radar (SAR), which can produce high resolution, imagery, day or night, even under cloud cover.

Laser sensors have recently begun to be used more frequently for monitoring air pollution by laser spectrometers and for measurement of distance by laser altimeters.

Figure 5.2 shows the most common sensors and their spectral bands.

Those sensors which use lenses in the visible and reflective infrared

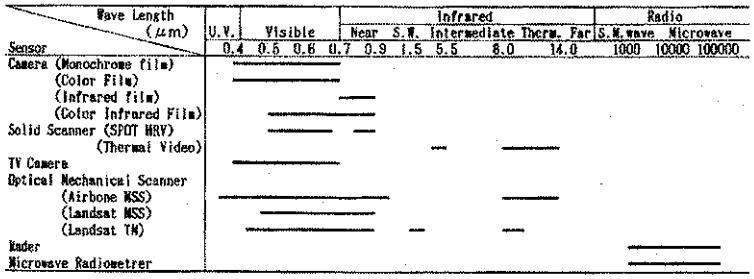

Figure 5.2: Wave length band of principal Sensor

region, are called optical sensors.

5.2 Characteristics of Optical Sensors

Optical sensors are characterized specified by spectral, radiometric and geometric performance. Figure 5.3 summarizes the related elements for the three characteristics of optical sensor. Table 5.1 presents the definitions of these elements.

The spectral characteristics are spectral band and band width, the central wavelength, response sensitivity at the edges of band, spectral sensitivity at outer wavelengths and sensitivity of polarization.

The geometric characteristics are specified by those geometric factors such as field of view (FOV), instantaneous field of news (IFOV), band to band registration, MTF, geometric distortion and alignment of optical elements.

IFOV is defined as the angle contained by the minimum area that can be detected by a scanner type sensor. For example in the case of an IFOV of 2.5 milli radians, the detected area on the ground will be 2.5 m $\times$ 2.5 m, if the altitude of sensor is 1,000 m above ground.

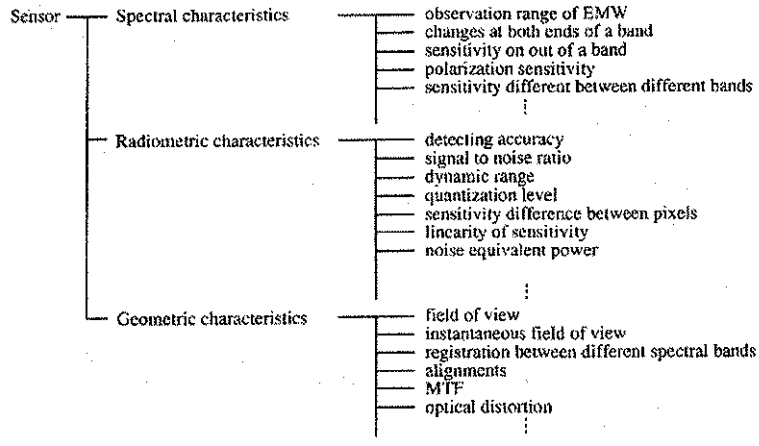

Figure 5.3: Definition of optical sensor's characteristics

5.3 Spectrometer

There are many kinds of spectral measurement devices, for example, spectroscopes for human eye observation of the spectrum, spectrometer to record spectral reflectance, monochro meter to read a single narrow band, spectro photometer for photometry, spectro radiometer for measurement of spectral radiation etc. However, in this section only optical spectrometers are of interest.

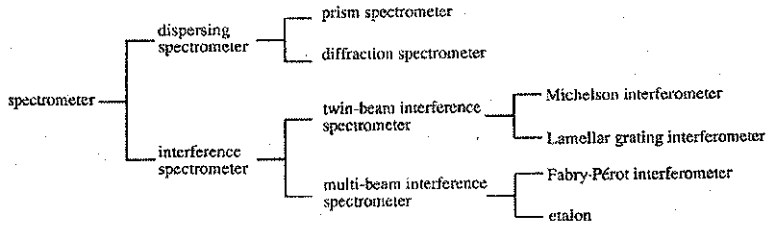

Figure 5.4: Spectrometers

items	definition
band range of EMW	observation width of EMW(Electro magnetic waves) on a band
center wavelength	center wave length on a band
band responsibility at both ends of a band	characteristics curve at both ends of a band
band sensitivity	sensitivity on a band
without band sensitivity	sensitivity on spectral ranges of outside of the band
sensitivity difference between different bands	ratio of sensitivity between different bands
S/N ratio	signal to noise ratio
dynamic range	range of sensor's sensitivity in terms of the difference maximum and minimum radiance ratio
sensitivity difference between pixels	ratio of maximum output level to minimum output levels pixels
linearity of sensor's input-output characteristics	input level to output level in higher input power level
noise equivalent power	input signal power giving output equivalent with noise power
field of view	covered area by a remote sensor, picture (angular field of camera, scanning width by scanner
instantaneous field of view (IFOV)	field of angle detected by one detector
registration between different spectral bands	geometric distortion between one standard band and other bands
MTF	modulation transfer function of a sensor, determining it's IFOV
optical distortion	image distortion due to optical components of a sensor. e.g. lens aberration
angle of stereoscopic observation	difference of viewing angle of stereoscopic sensors
imaging frequency	time of scanning one line

Table 5.1: Definition of optical sensor's characteristics

Figure 5.4 shows a classification of spectrometers, which are divided mainly into dispersing spectrometers and interference spectrometers. The former utilizes prisms or diffraction gratings, while the latter the interference of light.

5.3.1 Dispersing spectrometer

A spectrum is obtained at the focal plane after a light ray passes through a slit and dispersing element as shown in Fig 5.5. Figure 5.6 is a typical dispersing spectrometers;

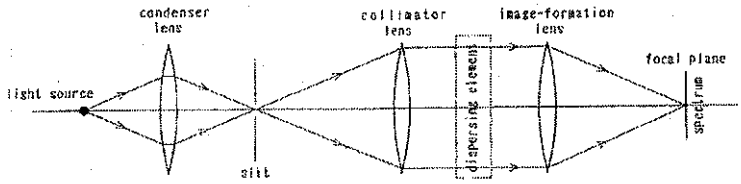

Figure 5.5: Conceptual structure of dispersing spectrometers (Lanses are exchangable by spherical mirrors and/or parabolic mirrors)

5.3.2 Twin beam interference spectrometer

A distribution of the spectrum is obtained by cosine Fourier transformation of the interferogram which is produced by the inference between two split rays. Figure 5.7 shows Michelson interferometer which utilizes a beam splitter.

5.3.3 Multi-beam interference spectrometer

The interference of light will occur if oblique light is incident on two parallel semi-transparent plane mirrors. A different spectrum is obtained depending on incident angle, interval of the two mirrors and the refraction coefficient (Fig. 5.8).

Imaging spectrometers are characterized by a multispectral scanner with a very large number of channels (64–256 channels) with very narrow band widths, though the basic scheme is almost the same as an optical mechanical scanner or pushbroom scanner.

Figure 5.9 (imaging spectrometry with line arrays) shows a similar scheme to the right upper system but with an additional dispersing element (grating or prism) to increase the spectral resolution. The right lower (imaging spectrometry with area arrays) shows an imaging spectrometer with area arrays.

Table 5.2 shows the optical scheme of the Moderate Resolution Imaging

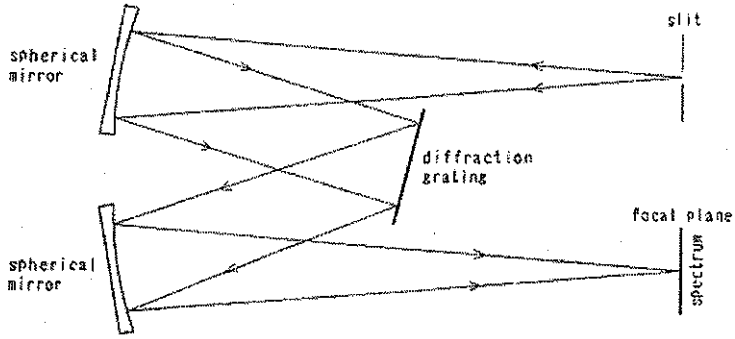

Figure 5.6: Czerny-Turnaer spectrometer using diffraction grating (The diffraction grating is exchaned by a prism)

items	dioptic system	dio & catoptics system	catoptics system
wide angle (>90°)	most suitable	suitable	unsuitable
temperature effect	no good	middle	good
stray light effect	no good	middle	good
observation range	narrow (color aberration)	middle	wide
aperture (>250mm)	unsuitable	suitable	most suitable
linearity of optical axis	bad	middle	good
size & weight	big & heavy	middle	small & light

Table 5.2: Comparison with dioptic system & catoptic system

Spectrometer-Tilt (MODIS-T) which is scheduled to be carried on EOS-a (US Earth Observing Satellite). MODIS-T has an area array of 64×64 elements which enables 64 multispectral bands from 0.4 mm to 1.04 mm with a 64 km swath. The optical path is guided from scan mirror to Schmitt type off axis parabola of dio and catoptic system. The the light is then dispersed into 64 bands by a grating and is detected by an area CCD array of 64×64 elements.

As imaging spectrometer provides multiband imagery with a narrow wave length range, and is useful for rock type classification and ocean color analysis.

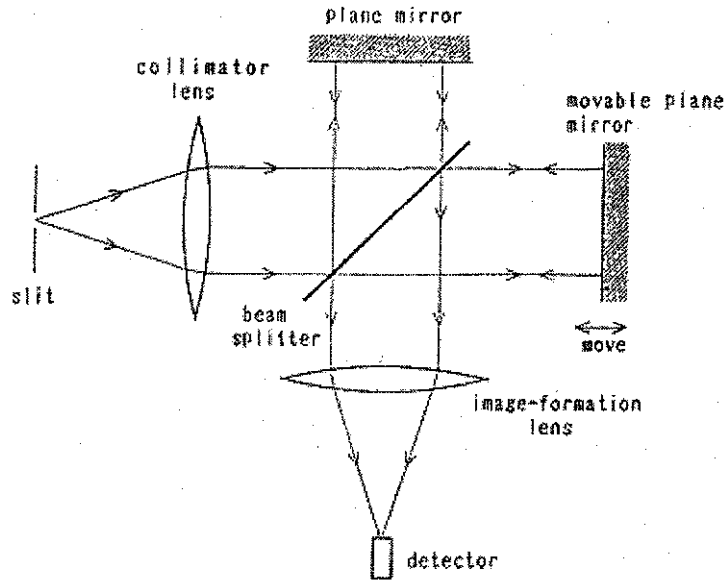

Figure 5.7: Michelson interferometer

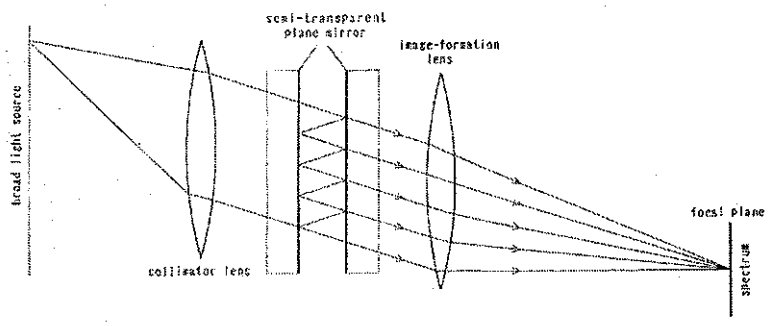

Figure 5.8: Fabry-Pérot interferometer. That in which, space between mirrors is fixed, is called as an etalon.

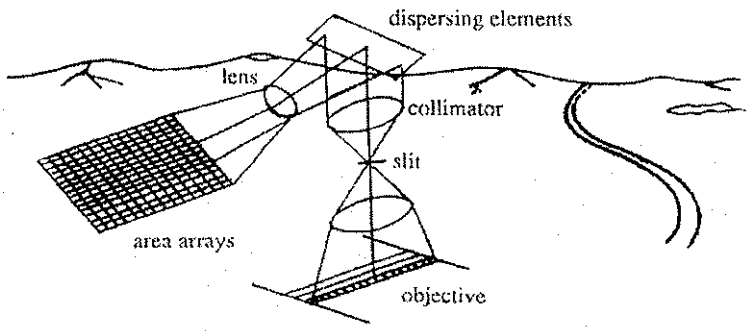

Figure 5.9: Imaging spectrometry with area array

5.4 Atmospheric Sensors

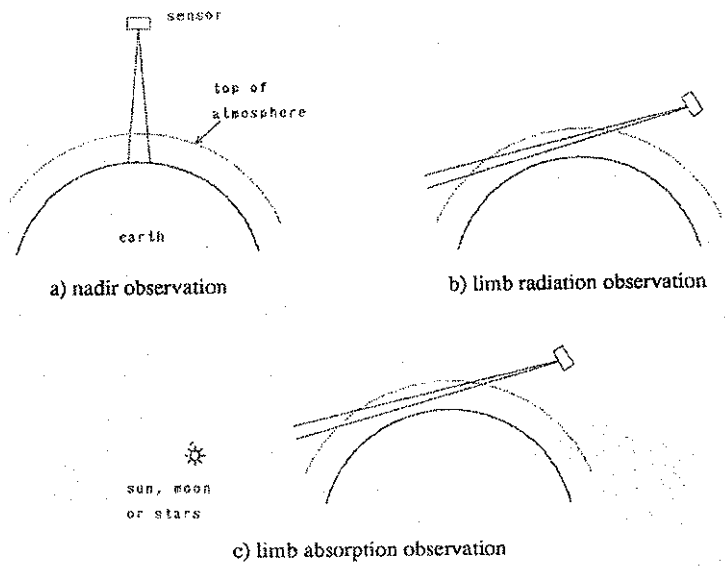

Figure 5.10: Direction of atmospheric observation

Atmospheric sensors are designed to provide measures of air temperature, vapor, atmospheric constituents, aerosols the etc. as well as wind and earth radiation budget. The spectral wave length range is very wide from the near ultraviolet to the millimeter radio wave depending on the objects to be measured.

Two directions of atmospheric observation are usually adopted; one is nadir observation and the other is limb observation as shown in Fig. 5.10. The nadir observation is superior in the horizontal resolution compared to vertical resolution. It is mainly useful in the troposphere but not in the stratosphere where the atmospheric density is very low.

The limb observation method is to measure the limb of the earth with an oblique angle. In this case, not only atmospheric emission but also

atmospheric absorption of the light of the sun, the moon and the stars are measured, as shown in Fig. 5.10. Compared with the nadir observation, the limb observation has higher vertical resolution and higher measurability in the stratosphere. The absorption type of limb observation has rather high S/N but observation direction or area is limited except for the stars.

Chapter 6

Applications of Remote Sensing

Yoshiaki Honda
Center for Environmental Remote Sensing, Chiba Univ.
1-33 Yayoi, Inage-ku, Chiba, 263-8522, JAPAN
Phone: +81-43-290-3835, fax: +81-43-290-3857
E-mail: yhonda@rsirc.cr.chiba-u.ac.jp

This part of the text is extracted from Remote Sensing Note which was published by Japan Association on Remote Sensing (JARS).

6.1 Land Cover Classification

Land cover mapping is one of the most important and typical applications of remote sensing data. Land cover corresponds to the physical condition of the ground surface, for example, forest, grassland, concrete pavement etc., while land use reflects human activities such as the use of the land, for example, industrial zones, residential zones, agricultural fields etc. Generally land cover does not coincide with land use. A land use class is composed of several land covers. Remote sensing can provide land cover information

rather than land use information.

Initially the land cover classification system should be established, which is usually defined as levels and classes. The level and class should be designed in consideration of the purpose of use (national, regional or local), the spatial and spectral resolution of the remote sensing data, user's request and so on.

The definition should be made as quantitatively clear as possible. Figure 6.1 shows an example of land cover classes for land cover mapping in the Sagami River Basin, Japan, for use with Landsat MSS data.

The classification was carried out as follows.

a. **Geometric correction**
   A geo-coded Landsat image was produced.

b. **Collection of the ground truth data**
   A ground investigation was made to identify each land cover class on the geo-code Landsat image as well as on topographic maps.

c. **Classification by Maximum Likelihood Method**
   The Maximum Likelihood Method was adopted using the training samples obtained from the ground truth.

Figure 6.1 shows the classified land cover map.

Generally Landsat MSS imagery can provide about about ten land cover classes, depending upon the size and complexity of the classes.

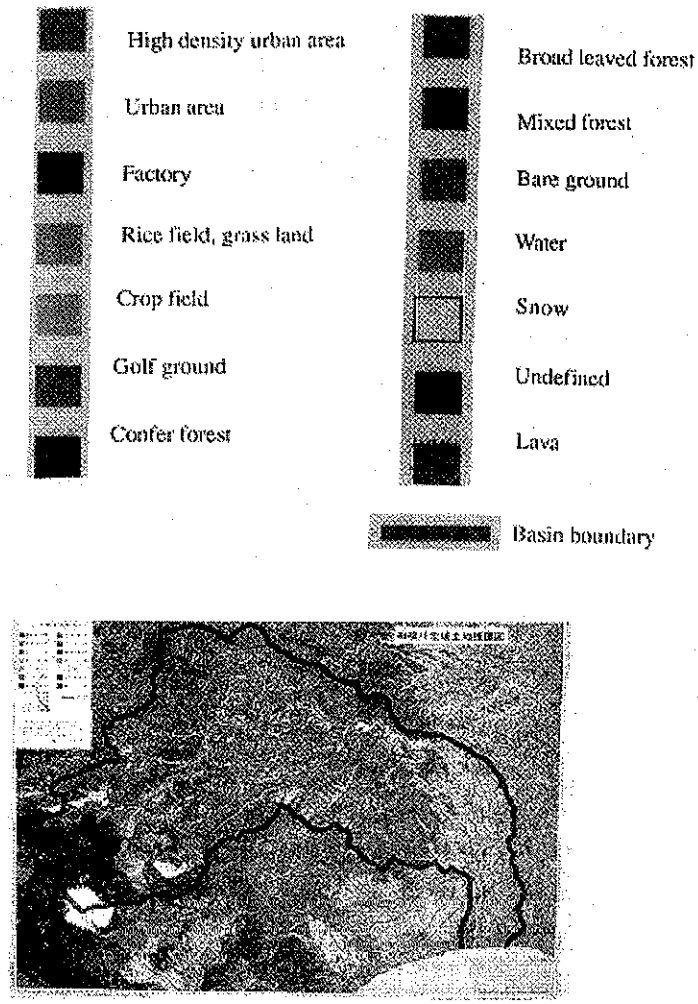

Figure 6.1: Land cover classification by Landsat MSS data

6.2 Land Cover Change Detection

Land cover change detection is necessary for updating land cover maps and the management of natural resources. The change is usually detected by comparison between two multi-date images, or sometimes between an old map and an updated remote sensing image.

The method of change detection is divided into two;

a. comparison between two land cover maps which are independently produced

b. change enhancement by integrating two images into a color composite or principal component image.

Such detection is very useful for updating "vegetation maps" of 1:50,000 to 1:100,000 scale with Landsat TM or SPOT, and of 1:250,000 scale with Landsat MSS.

The land cover change can also be divided into two;

a. **seasonal change**
Agricultural lands and deciduous forests change seasonally.

b. **annual change**
Land cover or land use changes, which are real changes, for example deforested areas or newly built towns.

Usually seasonal change and annual change are mixed within the same image. However only the real change should be detected, so that two multi-data images of almost same season should be selected to eliminate the effects of seasonal change. One should note that a cycle of seasonal change can be rather complex as shown in Fig. 6.2. Sometimes seasonal change rate is very high, for example in spring time in cold area.

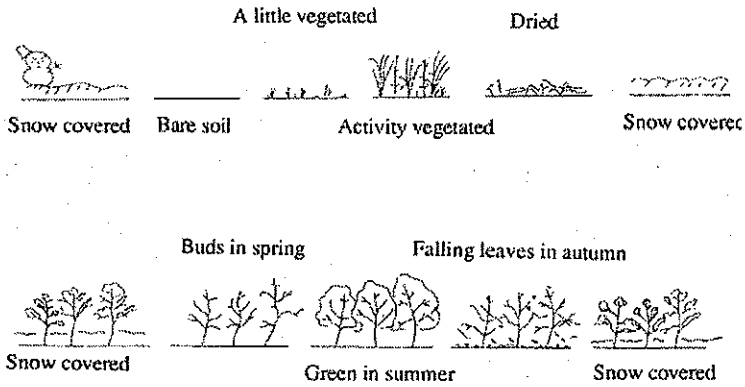

Figure 6.2: Seasonal change of grassland (upper) and deciduous (lower)

6.3 Global Vegetation Map

NOAA AVHRR data are very useful for producing a global vegetation maps which cover the whole world, because NOAA has edited global cloud free mosaics in the form of a GVI(global vegetation index) on a weekly basis since April of 1982.

The GVI data include information about NDVI (Normalized Difference Vegetation Index) as computed as follows

$$\mathrm{NDVI} = \frac{\mathrm{Ch.2} - \mathrm{Ch.1}}{\mathrm{Ch.2} + \mathrm{Ch.1}} \tag{6.1}$$

Ch.1: visible band
Ch.2: near infrared band

NDVI is sometimes simply called NVI (Normalized Vegetation Index). NDVI or NVI are indicators of the intensity of biomass. The larger the NVI is, the denser the vegetation.

Though the original resolution of NOAA AVHRR is 1.1 km per pixel of the Equator, the GVI has a low resolution of 16 km $\times$ 16 km per pixel at the Equator. In spite of the low resolution, the GVI is useful for producing a global vegetation map.

6.4 Water Quality Monitoring

Water pollution has become a very serious problem in big cities and in offshore areas along industrial zones. Water quality monitoring is one of the typical applications of remote sensing.

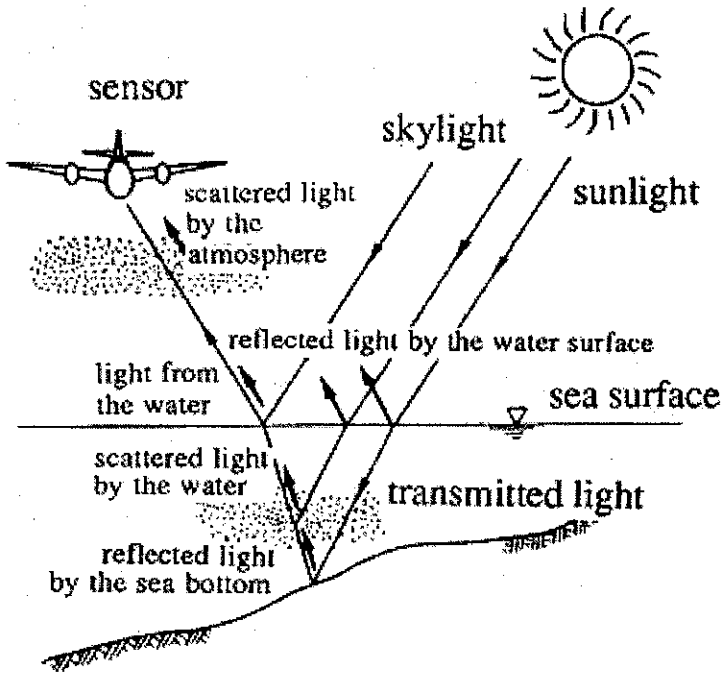

Figure 6.3: Incident light into a sensor on the sea

Figure 6.3 shows the characteristics of reflection, absorption and scattering on the water surface, beneath the surface water and from the bottom. The sea color depends on the absorption and scattering due to water molecules and suspended particles or plankton.

Figure 6.4 shows various curves of spectral attenuation with respect to various types of water. As seen in the figure, clear water has a peak of minimum attenuation around 0.5 μm, while turbid water with suspended solid (SS) has larger attenuation with a minimum peak around 0.55 μm. In other words, radiation can penetrate into deep clear water and is scattered by the water volume, causing the typical bluish color. Turbid waters cannot be penetrated and radiation is scattered near the surface, giving a greenish or yellowish color.

The sea color depends on not only suspended solids but also the chlorophyll of plankton within the water body. Figure 6.5 shows an example of the measurement for spectral reflectance of various amounts of chlorophyll. As seen in the figure, chlorophyll in the sea can be detected in the region of 0.45–0.65 μm.

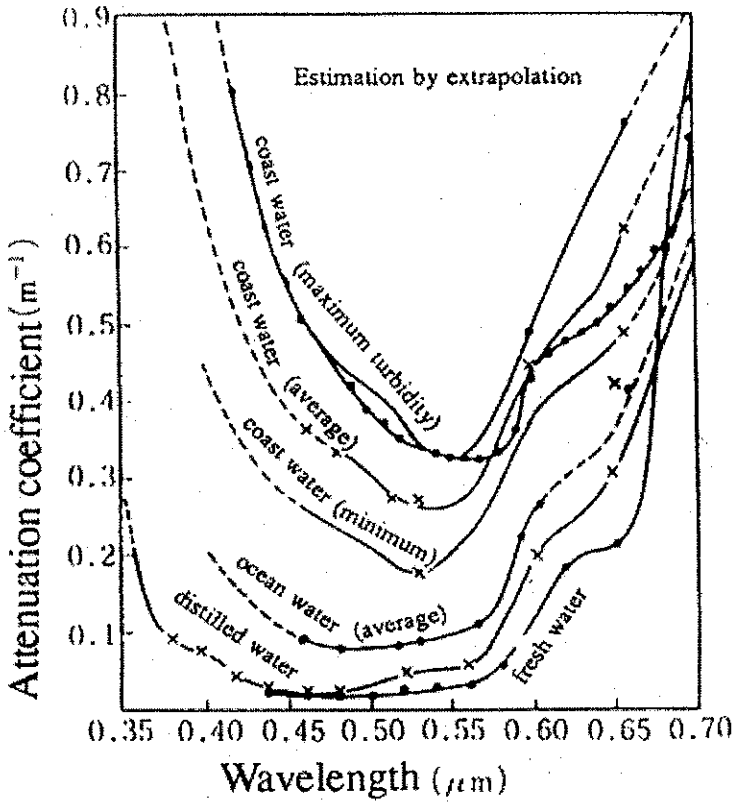

Figure 6.4: Spectral attenuation characteristics of water

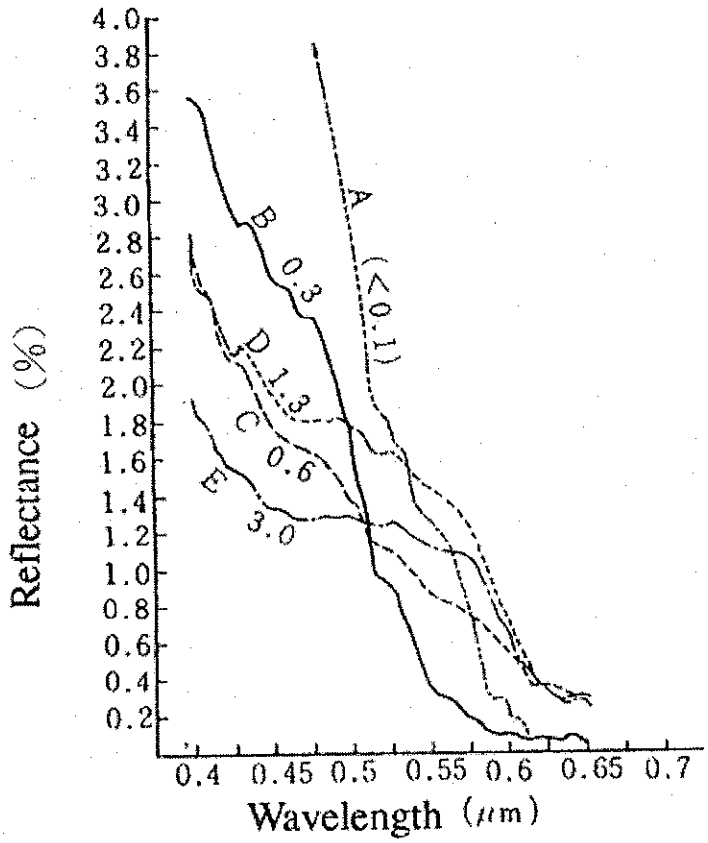

Figure 6.5: Spectral reflectance of water with chlorophyll

6.5 Measurement of Sea Surface Temperature

The temperature detected by a thermal sensor is called the "brightness temperature". Though the brightness temperature coincides with the real temperature if the objects is a black body, the actual object on the earth has a different emissivity e ($e < 1$) which emits electro-magnetic energy of eI, where I indicates the radiance of a black body with the same temperature.

Thus the value of e as well as the emitted radiance should be measured in order to compute the exact temperature, as explained in Fig. 6.6.

However the value of e for sea water is very nearly equal to 1 and also comparatively constant, while the value e for ground surfaces is not homogeneous. Thus sea surface temperature can be estimated more accurately than ground surface temperature.

As the actual brightness temperature includes emitted radiance from the atmosphere, this will cause a temperature error ranging 2–3 K between the actual sea surface temperature and calculated brightness temperature from satellite data. Thus atmospheric correction is very important for accurate sea surface temperature measurement.

Figure 6.7 shows the sea surface temperature in pseudo color in Northern Japan using NOAA AVHRR data which were atmospherically as well as geometrically corrected with overlays of sea coast lines and latitude and longitude grid lines.

Using the most recent technology, the estimated accuracy of sea surface temperature is claimed to be about ± 0.5 K on a global scale and about ± 0.3 K on a regional scale.

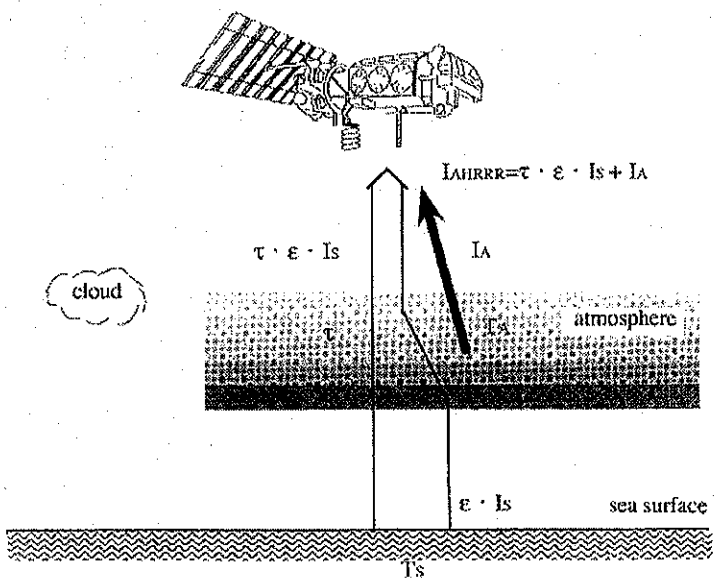

TS	: sea surface temperature
IS	: electromagnetic energy emitted form black body at temperature TS
ε	: emissivity of atmosphere
τ	: transmittance of atmosphere
TA	: average temperature of atmosphere
IA	: electromagnetic energy emitted form atmosphere at temperature TA
IAVHRR	: electromagnetic energy detected by AVHRR sensor

Figure 6.6: Sea surface temperature measurement

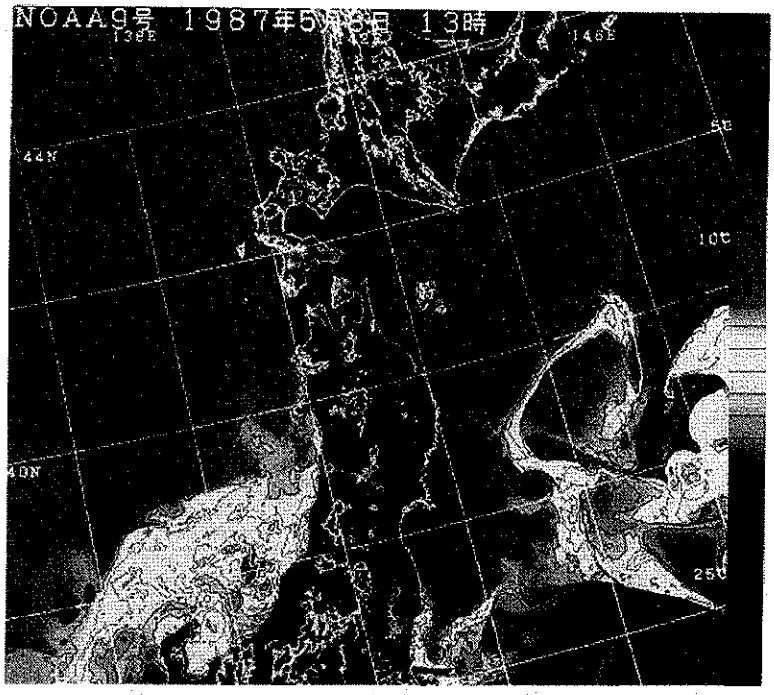

Figure 6.7: Sea surface temperature map derivered from NOAA AVHRR data

6.6 Snow Survey

As snow cover has a very high reflectance, the aerial distribution of snow can be identified very easily from satellite remote sensing data. Several models to estimate water resources in units of snow water equivalent have been proposed with use of the estimated snow cover area.

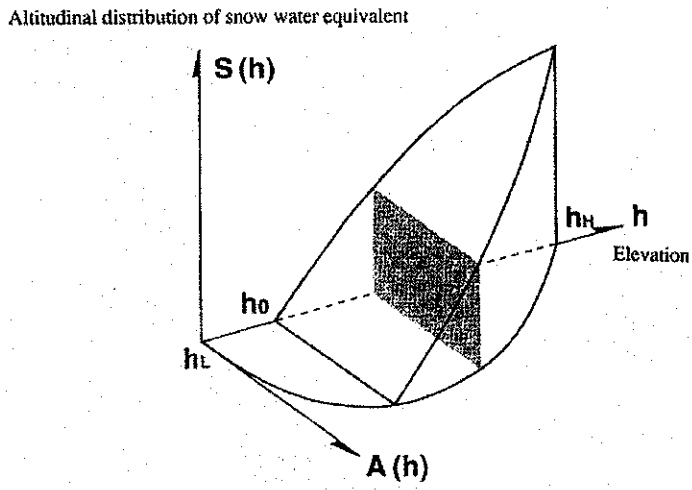

Figure 6.8: Estimation of basin-wide snow water equivalent

Figure 6.8 shows a conceptual diagram of the estimation of basin-wide snow water equivalent with the three parameters of elevation h, latitudinal distribution of snow water equivalent $S(h)$ and hydrometric curve $A(h)$.

Snow water equivalent S_s in a river basin can be computed as follows.

$$S_s = \int_{h_L}^{h_H} S(h)A(h)dh \tag{6.2}$$

where
h_H: maximum elevation
h_L : minimum elevation

If snow appears over the average elevation of snow line h_o, h_L should be replaced by ho. From the above formula, the latitudinal distribution of snow water equivalent $S(h)$ and the hydrometric curve $A(h)$ should be determined in order to estimate the snow water equivalent.

It is known that the snow water equivalent increases linearly proportional to the elevation, which can be obtained from the existing snow survey. On the other hand, the catchment area can be expressed in lower order of polynomials as a function of elevation. Therefore the snow water equivalent can be estimated as a function of percentage of snow cover area in a river basin.

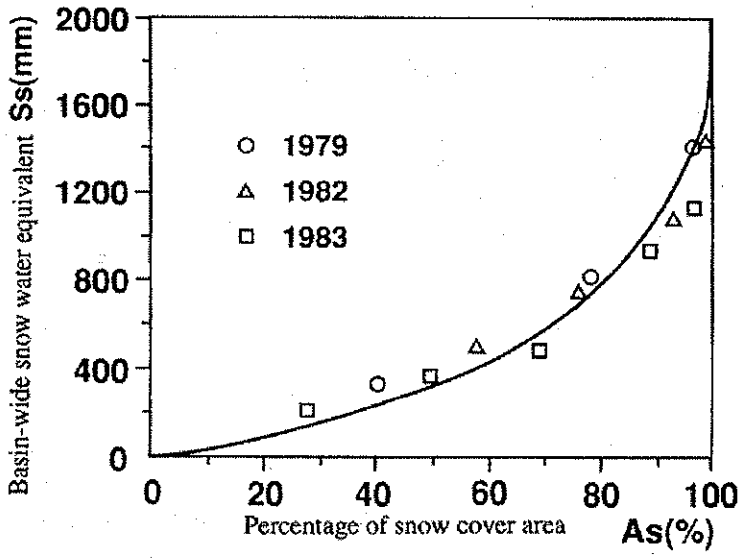

Figure 6.9: Result of model application to Takaragawa main stream basin

Figure 6.9 shows an estimated curve of snow water equivalent which was obtained from sample data in the three years of 1979, 1982 and 1983 in the Takaragawa River Basin, Japan. From the curve, the snow water

equivalent can be estimated if the snow cover area is detected from remote sensing imagery (Fig. 6.10).

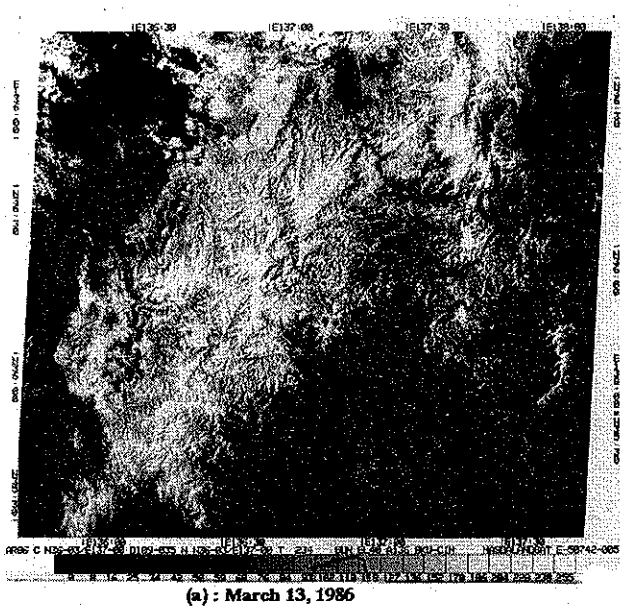

(a) : March 13, 1986

Figure 6.10: Snow line change by Landsat TM images

Recently microwave remote sensing has been applied to estimate snow volume. Passive microwave radiometers can provide snow surface temperature with respect to inductivity of the snow, which may provide snow information. Active microwave radar can provide reflectivity or scattering of snow with respect to snow density, snow temperature, size of snow particles etc. It is still difficult to estimate snow volume from microwave data but several research projects are currently being carried out on this topic.

6.7 Monitoring of Atmospheric Constituents

Each atmospheric constituent such as water vapor, carbon-dioxide, ozone, methane etc. has its own unique spectral characteristic of emission and absorption. With the use of these characteristics, the density of these atmospheric molecules can be monitored by measuring the spectral energy which transmits from the sun, the moon or the stars through the atmosphere, the scattering energy from the atmosphere or the clouds, the reflected energy from the earth surface and/or the thermal radiation emitted from the atmosphere and the earth surface. The spectral energy can be measured by two methods; absorption spectroscopy and emission spectroscopy.

These methods have been applied for many years ago for the measurement of the upper atmosphere from the ground. Recently the methods have been extended for measurements from aircraft, balloon and satellite. In addition, multi-spectral laser with variable wavelength, called laser rader or lidar, has been developed for the measurement of the spatial distribution of the atmospheric constituents.

Figure 6.11 shows the spectral transmittance of H_2O, CO_2, O_3, N_2O and CH_4 in the infrared region. Figure 6.12 shows the spectral attenuation of water vapor (H_2O), and oxygen with a number of channels of the AMSU (Advanced Microwave Sounding Unit) instrument.

There are three methods used to measure the vertical distribution of atmospheric constituents; the occultation method which measures the attenuating light of the sun light at the sun rise and the sun set, from a satellite, the limb scan method which measures the spectrum of atmosphere around the limb of the earth and the vertical viewing method, which measures the atmospheric emission from various altitudes and contribution ratio are analyzed with respect to the spectral absorption coefficient by the inversion method. The vertical look down method is operationally applied for carbon-dioxide and water vapor in the infrared region and for ozone in the ultra-violet region.

Figure 6.13 shows the normalized contribution function at various wavelengths in the ultra-violet region where the vertical distribution of ozone is measured from the back scattering of blue ultra-violet (BUV) radiation.

6.8 Lineament Extraction

Lineament is defined as a line feature or pattern interpreted on a remote sensing image. The lineament reflects the geological structure such as faults or fractures. In this sense, the lineament extraction is very important for the application of remote sensing to geology. However the real meaning of lineament is still unclear. It should be discriminated from other line features that are not due to geological structures. Therefore the lineament extraction should be carefully interpreted by geologists.

Computer generated lineament would involve all linear features of natural terrain as well as artificial structures which have to be removed by interpretation. As lineaments can be interpreted very well on satellite images, geological survey methods have been advanced, particularly over large areas. Lineament extraction is useful for geological analysis in oil exploration in which oil flow along faults, oil storage within faults and the oil layer can be estimated. Lineament information can even allow analysis of the geological structure and history.

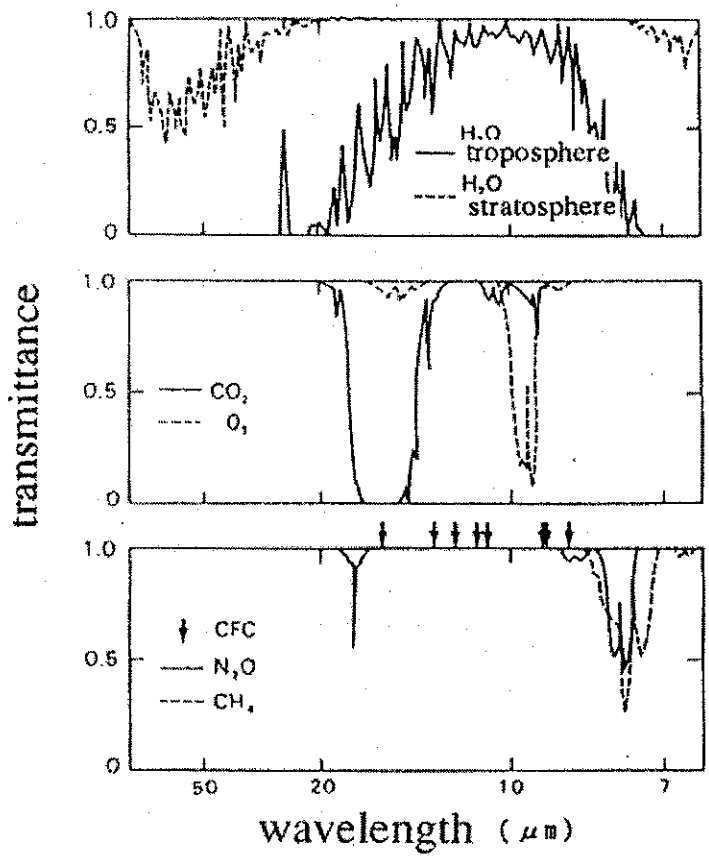

Figure 6.11: Spectral profile of the atmospheric transmission for thermal infrared radiation. Indicated are the amount integrated from the ground surface to the upper end of the atmosphere. Main absorption bands of trace gases are indicated.

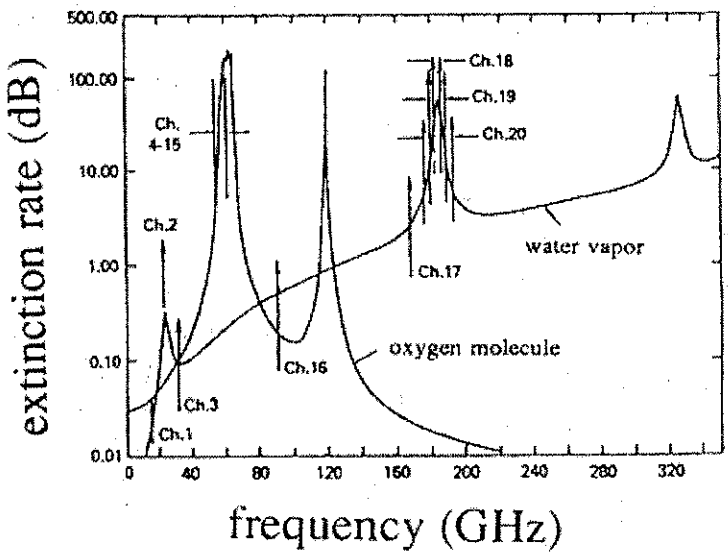

Figure 6.12: Atmospheric absorption spectrum in the microwave range

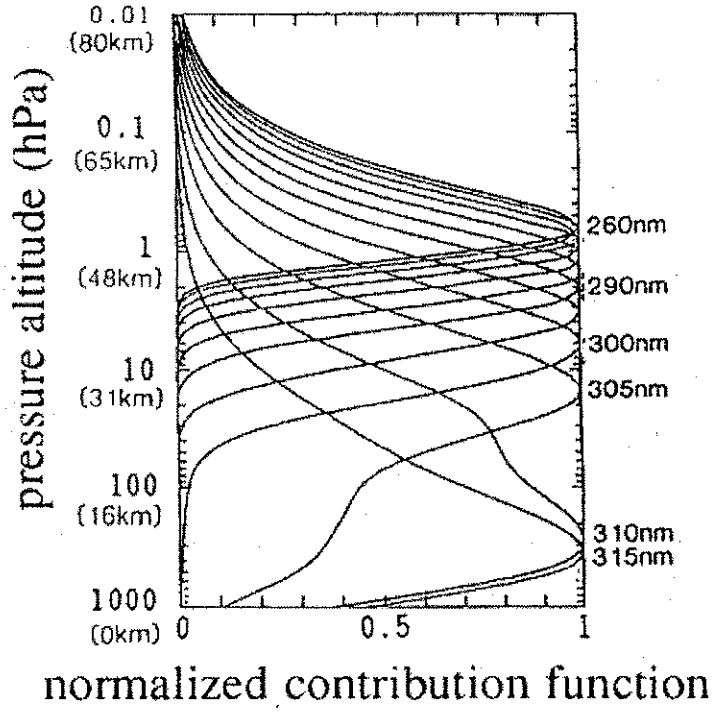

Figure 6.13: Vertical profile of contribution functions in each wavelength for solar ultraviolet back scattering light

6.9 Geological Interpretation

The applicability of remote sensing data increases according to the improvement in the spatial resolution as well as the spectral resolution , for example as from Landsat MSS to Landsat TM and SPOT HRV. The advantage of satellite remote sensing in its application to geology is the wide coverage over the area of interest, where much useful information such as structural patterns and spectral features can be extracted from the imagery.

There are two ways of information extraction; geometric feature extraction with the use of geomorphologic patterns and radiometric feature extraction using the unique characteristics of spectral absorption corresponding to the rock type.

Generally visual image interpretation is most widely used in order to extract geological information from remote sensing images. A comprehensive analysis can be carried out with geomorphologic information such as land form and slope, drainage pattern and density, and land cover.

Radiometric interpretation of multi-spectral features is mainly applied to rock type classification. Because each rock has its own spectral absorption band in the region of the short wave infrared, data from multi-spectral scanners or imaging spectrometers with multi channels is very useful for rock type classification. Thus the OPS data of JERS-1 will be useful in geology because of the shortwave infrared bands.

6.10 Height Measurement (DEM Generation)

Topographic mapping or DEM (Digital Elevation Model) generation is possible with a pair of stereo images.

The height accuracy Δh depends on the parameters of base-height ratio (B/H) and the accuracy of parallax which may be approximated by ground resolution ΔG, as indicated as follows.

$$\Delta h = H/B\Delta G \tag{6.3}$$

Table 6.1 shows the theoretical accuracy of height determination for Landsat MSS, Landsat TM and SPOT HRV (panchromatic). In the case of SPOT HRV, with maximum base length and a B/H ratio of about 1, the height accuracy will be about 10 m the same as the ground resolution, which will be suffcient to produce topographic maps with contour lines of 40 m interval.

parameter / Satellite	Satellite height	Orbital interval	Ground resolution	Height accuracy
Landsat MSS	705,000 (m)	145,000 (m)	83 (m)	400 (m)
Landsat TM	705,000 (m)	145,000 (m)	30 (m)	145 (m)
SPOT pan.	830,000 (m)	840,000 (m)	10 (m)	10 (m)

Table 6.1: Height accuracy of elevation data derived from satellite stereo images

There are two methods of topographic mapping or DEM generation; using operator based analytical plotters with special software, and automated DEM generation by stereo matching. Usually rectified images for a pair of stereo images are initially pre-processed using ground control points. Then stereo matching is applied to determine the conjugate points, which give x-parallax or difference of height to be converted to the height or elevation.

Chapter 7

Lidar and the Global Environment

Toshikazu Itabe
Communications Research Laboratory
Ministry of Posts and Telecommunication, Japan
4-2-1, Nukui-Kitamachi, Koganei, Tokyo 184-8795, Japan
Phone: +81-423-27-7546 fax: +81-423-27-6667
E-mail: itabe@crl.go.jp

Abstract

There are two ways to obtain global data for monitoring the global environment by using techniques of remote sensing. One of them is based on an observation network, which is a system to get data located at many places globally. Another one is to get data by a spaceborne sensor. Lidar is an active sensor with a laser as a source and can be used as one of the most important tools for both of the ways. the lidar can monitor clouds, aerosol and many gases which are closely related to the global environment. This chapter describes how the lidar is working for the global environment.

7.1 Introduction

It is well know that the global environment is now changing due to human activity. Ozone depletion and global warming are two important issues. A lidar is an active remote sensor similar to radar. The lidar uses laser as a light source with very short wavelengths, less than 10 μm, and is used in research of the ozone depletion and global warming in addition to radar and other remote sensors.

The following lidars are used for research of the global environment.

Mie lidar	aerosol and cloud in the troposphere and stratosphere (Fig. 7.1)
Ozone DIAL	ozone in the troposphere and stratosphere
H_2O DIAL	H_2O vapor in the troposphere

where the DIAL is a **DI**fferential **A**bsorption **L**idar using a method to measure gas from the difference of on-line and off-line absorption of two laser sources. Aerosols are small particles with a diameter of the order of μm.

Other lidars can be used to measure the atmospheric wind and temperature and metal vapor layer existing around the mesopause. The Mie lidar is a unique sensor to measure aerosols, which is now recognized to be important in the study of global warming as well as the stratospheric ozone depletion. Ozone and H_2O DIALs are suitable sensors for observing the ozone and the H_2O vapor from aircrafts and spacecrafts.

7.2 Ozone Hole

Roles of aerosols in ozone depletion and global warming are described here briefly. The dramatic decrease of Antarctic stratospheric ozone in October were reported by Farman and his colleagues in 1985. They attributed it to the catalytic chemistry of chlorine compounds, Cl and ClO, as follows.

$$\mathrm{ClO} + \mathrm{O} \longrightarrow \mathrm{Cl} + \mathrm{O} \tag{7.1}$$

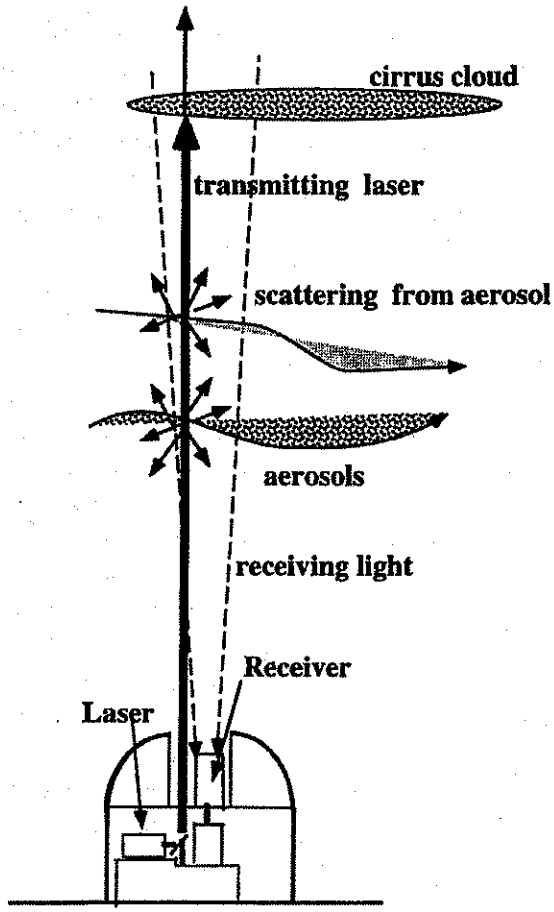

Figure 7.1: Lidar observation of the atmosphere.

$$Cl + O_3 \longrightarrow ClO + O_2 \tag{7.2}$$

This phenomena was named the ozone hole by Farman and was theoretically expected by Molina and Rowland, who are the Novel prize winners of 1995. After the discovery of the Antarctic ozone hole, man-made chemical compounds such as chlorofluorocarbons, primarily $CFCl_3$ (or CFC-11 and CF_2Cl_2 (or CFC-12) are recognized as sources of the catalytic chemical compounds, which deplete the Antarctic stratospheric ozone. Their production was prohibited under the Montreal Protocol (June 1990).

Although Cl and ClO are produced from the photodissociation of chlorofluorocarbon those chlorine compounds react with nitrogen dioxide, NO_2 leading to the formation of less reactive chlorine nitrate, $ClONO_2$. Most of the chlorine in the stratosphere should be bound up in the less reactive compounds $ClONO_2$ or HCl, referred to as "reservoir" species of chlorine. Consequently, early chemical models of the Antarctic ozone hole did not explain the "Heterogeneous reactions" -that is, reactions on the surface of the aerosols. There are aerosols named Polar Stratospheric Clouds (PSC) in the winter stratosphere of the Antarctic. A model including heterogeneous reactions on the surface of PSC clouds did not explain the observed ozone depletion using known stratospheric NO and NO_2 concentrations.

The theory of the Antarctic ozone hole including Polar Stratospheric Clouds (PSC) is now almost confirmed. This tells us that the air in the Antarctic stratosphere is isolated within a strong polar vortex and is cooled down about 180 K. At temperatures between 190 and 200 K, Type 1 PSC, which are particles of condensed nitric acid, possibly in the crystalline form of nitric acid trihidrate, $HNO_3 \cdot 3\ H_2O$ (NAT particle) are produced. Heterogeneous reactions on the surface of NAT particles can make chlorine Cl_2 from $ClONO_2$ rapidly leading to ozone destruction. When the temperature is cooled down to about 188 K, the NAT particles begin to grow by condensation of H_2O vapor and become Type 2 PSCs, which fall to the troposphere due to gravity. As a resultsof the falling of the Type 2 PSCs, NO_2 and H_2O concentration are very low in the stratosphere within the Antarctic polar vortex (denitrification and dehydration). The low NO_2 concentrations al-

low the amount of free chlorine to be high through repartitioning of chlorine from reservoir species to Cl_2 and HOCl during the polar night. These PSCs can be distinguished by dual wavelength and depolarization observations of Mie lidar according to the table of Browell, NASA Langley as below:

Type of PSC	Scat.Ratio		α	Aero.Depol.		β
	Vis	IR		Vis	IR	
1a	1.2–1.5	2–5	0.4	30–50	30–50	~0
1b	3–8	5–20	2–3	0.5–2.5	<4	—
2	>10	> 20	< 0.8	>10	>10	~0

7.3 Lidar Observations Network

After much research on the Antarctic ozone hole, interests of scientists were directed to the north pole (Arctic) and the global ozone depletion. Network observations were started in 1991, by the Network Detection of the Stratospheric Change (NDSC). Stations of NDSC were assigned at three sites in the north polar region, one at the north middle latitude, one at the equatorial, one at the south middle latitude and 1 at the south polar region. Each station has to have a set of remote sensing instruments including a lidar to monitor ozone and key-ozone-related parameters. Japanese scientists cooperated on the NDSC and installed Mie lidars in many places which were selected for observation of the Pinatubu stratospheric volcanic clouds, which were produced by the eruption of Mt. Pinatubo (15N, 120E), on Luzon Island, Philippines (Table 7.1). The stations related to the Japanese scientists are shown in Table 7.1.

Type 1a PSCs were observed at Eureka in December, 1994 and January, 1995 (Fig. 7.2), since the Arctic stratosphere was so cold. The PSCs appeared at higher temperatures than the production temperature of NAT particles expected. The phenomena suggests a new production mechanism of the particles, although it was not clear. The PSC from 1994 to 1995 have destroyed the Arctic stratospheric ozone from the comparison with the satellite data at the same period.

Site	Location	Operating Institution/University
Arctic Region		
Erureka	80N, 86W (Canada)	CRL, MRI, STEL of Nagoya Univ.
Ny-Alesund	79N, 12E (Norway)	STEL of Nagoya Univ. Fukuoka Univ.
Fairbanks	65N, 147W (Alaska, USA)	STEL of Nagoya Univ. Fukuoka Univ.
In Japan		
Wakkanai	45N, 142E	CRL, TIT
Tsukuba	36N, 140E	MRI
Tokyo	36N, 139E	Tokyo Metropolitan Univ.
Nagoya	35N, 137E	STEL of Nagaya Univ.
Fukuoka	34N, 130E	Fukuoka Univ.
Okinawa	26N, 128E	MRI
Lanzhou	36N, 104E (China)	CRL, Lanzhou Desert Inst.
Bangkok	13N, 100E (Thailand)	CRL, KMITL
Bangkok	7N, 108E (Indonesia)('96)	CRL, MRI, STEL of Nagoya Univ., LAPAN

where
MRI; Meteorological Research Institute, Ministry of Transport
TIT; Tohoku Institute of Technology
STEL of Nagoya Univ; Solar Terrestrial and Environment Laboratory of Nagoya Univ.

Table 7.1: Stations for ozone monitoring

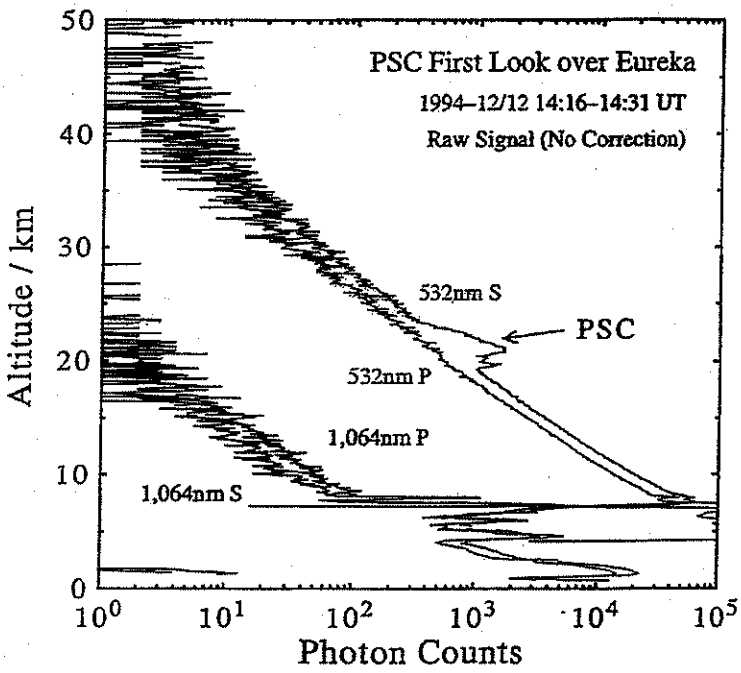

Figure 7.2: Lider observation of PSC over Eureka.

Aerosol observation have been conducting by using a lidar system on the campus of KMITL, Bangkok since February, 1994. The temperature of the tropopause over the tropics is sometimes lower than 190 K. That has suggested the possibility of the production of NAT particles near the tropopause over the tropics. Cirrus clouds were observed very often at a height of the tropopause by the lidar of KMITL. More precise microphysical processes between cirrus and the stratospheric aerosol over the tropics will be clarified from the analysis of lidar data.

It has been revealed that global ozone is depleted by the chlorine catalytic chemical reaction. After the eruption of Mt. Pinatube, a great amount of sulfur was injected into the stratosphere. The sulfur was converted to the volcanic sulfate particle (H_2SO_4), which formed Stratospheric Volcanic Clouds and spread all over the world. The volcanic clouds enhanced the heterogeneous reaction on the surface of the sulfuric acid droplet particles. Hofmann and Solomon showed that the following reaction is significant for the heterogeneous reaction of nitric compounds on the surface of the sulfuric acid droplet. $N_2O_5 + H_2O \longrightarrow 2HNO_3$. The heterogeneous reaction changes the chemical partition of nitric compounds in the stratosphere and leads to a decrease in $ClONO_2$ and in the ozone concentration by a similar process which causes the ozone hole. Photometric observations of the total column content of NO_2 at Hokkaido showed a decrease caused by the Pinatubo volcanic clouds. A decrease of ozone and the Mie backscattering coefficient are strongly correlated in the same period of the decrease of the NO_2 observation. The strong correlation indicated that global ozone depletion was occuring by the heterogeneous reaction on the increase surface area of the stratospheric volcanic clouds.

7.4 Future

Observations of global cloud distributions are very important for climate modeling. Height, thickness, particle size and ice-water content of the clouds are necessary to include the clouds in climate models. Clouds often have multi-layered structures. New sensors to observe those cloud parame-

ters are desired by many climate modellers. At present, it is believed that observations of clouds by a spaceborne Mie lidar and a cloud profiling radar are the most suitable sensors. Scientists are now seeking to realize such a satellite mission as soon as possible. The spaceborne lidar is called "Space Lidar", and has been researched and developed in many countries.

The NASA Space Shuttle Lidar was successfully launched in September, 1994 and has taken many data and shown us many beautiful cloud pictures. The Shuttle lidar mission is called as "Lidar In-space Technology Experiment" (LITE). Japan hopes to launch the first space lidar to measure clouds and aerosols in 2001.

Aerosols exist in the troposphere as well as the stratosphere. There are many types of aerosols, which generate dust, such as carbon particles from biomass burning, sulfate aerosols and so on. The key issue of tropospheric aerosols is the matter related to sulfate aerosols, since they are produced anthropogenicaly and are increasing so rapidly. Current estimates suggest that the increase in CO_2 has produced a net climate warming of 2–2.5 Wm^{-2}. Although the effect of sulfate aerosols on the climate is complicated, the increase of the sulfate aerosols cause increase the reflectance of the solar radiation, producing a net climate cooling of 0.9–0.3 Wm^{-2}, that is negative warming. The reflectance of solar radiation is called direct radiative forcing. Sulfate aerosols in the troposphere have another effect, since they become cloud condensation nucleus (CCN) particles. When clouds form in air with increased sulfate aerosols as CCN, the clouds reflectivity is enhanced because of the increased concentration of CCN. Simultaneous lidar and in-situ observations are needed to study the interaction between aerosols and clouds and will be started soon under a well organized program.

A ground based lidar network can see precise time variability with high vertical resolution. On the contrary, a space lidar can see globally but it takes time to see all the world. Also, space lidar needs to be calibrated and validated under the support of the ground based network observation. After once finishing the calibration and validation, the space lidar can provide us unique data as the LITE has shown. In any event, Lidar network observations and space lidar observations are complementary ways to mon-

itor the global environment. To clarify our understanding of the global environment, more active and well organized observations including lidar are desirable.

Chapter 8

Japanese Earth Observation Programs

Haruhisa Shimoda
Tokai University Research & Information Center
2-28 Tomigaya, Shibuya-ku, Tokyo 151-0053, Japan
Phone: +81-3-3481-0611, fax: +81-3-3481-0610
E-mail: smd@keyaki.cc.u-tokai.ac.jp

8.1 Introduction

The Japanese program for Earth observation from space has been, and continues to be conducted by NASDA (National Space Development Agency of Japan). There are two space agencies in Japan, *i.e.* NASDA and ISAS (Institute of Space and Astronomical Sciences), but ISAS has been engaged in space sciences and not earth sciences. Here, a brief history and future plans of Japanese Earth observation programs will be described.

8.2 MOS (Marine Observation Satellite)

The first Japanese Earth observation satellite was MOS-1, which was launched in 1987. It carried three sensors, *i.e.* MESSR, VTIR and MSR. MESSR (Multi-spectral Electronic Self Scanning Radiometer) is a 4-band pushbroom scanner with 50 m resolution. VTIR (Visible and Thermal Infrared Radiometer) is a 4-band wide swath whiskbroom radiometer, which was designed to measure sea surface temperature. MSR (microwave Scanning Radiometer) is a 2-band microwave radiometer.

After MOS-1, a similar satellite which was named MOS-1b was launched in 1990. These satellites were operational until around 1994, and especially MESSR was used for the study of Japan and Asia. As those satellites were not equipped with data recorders, only areas which were covered by ground receiving stations were observed.

8.3 JERS-1

In 1992, JERS-1 (Earth Resources Satellite) was launched. This satellite was developed by NASDA and MITI (Ministry of International Trade and Industry). Two sensors, *i.e.* OPS and SAR were on-board the satellite.

OPS (Optical Sensor) was actually composed of two sensors called VNIR (Visible and Near Infrared Radiometer) and SWIR (Short Wave Infrared Radiometer). The former has 3 bands in the visible and near infrared region while the latter has 4 bands in the short wave infrared region. Both sensors have 75 km swath and 18 m $\times$ 24 m resolution. The detector of the SWIR was cooled by an active refrigerator, but unfortunately this cooler stopped after 2 years of operation.

SAR (Synthetic Aperture Radar) is an L band synthetic aperture radar with 75 km swath and 18 m resolution. Unlike MOS-1, JERS has carried an onboard data recorder, and global data have been obtained.

JERS-1 stopped its operation in 1998, but within its life of more than 6 years, a huge volume data have been acquired. Especially, it should be noted that SAR images of most of the global tropical and boreal forests

were obtained. This intensive forest mapping was done as a part of Global Forest Mapping project, and the global forest data set is under development for the study of global land eco-systems.

8.4 ADEOS

The main objectives of ADEOS are to contribute to elucidation of phenomena of the earth system through integrated observation of geophysical parameters using a number of sensors. The main parameters observed by ADEOS are 1) energy flux between atmosphere and ocean, 2) three-dimensional distribution of temperature and water vapor, 3) aerosol distribution over ocean, 4) three-dimensional distribution of ozone, 5) chlorophyll distribution in ocean, 6) sea surface temperature, 7) ocean wind vector and 8) vegetation distribution.

In addition to the scientific purpose, the data acquired by ADEOS can be used for practical applications such as weather forecasting, probing of fishing grounds, land cover surveying and elevation measurement.

While ADEOS is the first satellite to observe the earth system in an integrated manner, long-term observation is required in order to fully understand changes of global environmental phenomena. It is hoped that a sufficient level of understanding will eventually be achieved through observations made by the ADEOS-II and other satellites, which will succeed to the ADEOS's mission in the future.

ADEOS carries 8 sensors on board, *i.e.* OCTS, AVNIR, NSCAT, TOMS, POLDER, ILAS, RIS and IMG.

ADEOS was launched on August, 1996 and all the instruments worked well, but on 30, June, 1997, it stopped its operation due to the breakdown of its solar paddle. Although ADEOS was operational less than 10 months, data acquired by ADEOS will be very valuable for the understanding of the global environment.

Ocean Color and Temperature Scanner (OCTS) is an optical radiometer to achieve highly sensitive spectral measurement with 12 bands covering visible and thermal infrared regions. In the visible and near-infrared

bands, the ocean conditions are observed by taking advantage of spectral reflectance of the dissolved substances in the water and phytoplankton. On the other hand, the sea surface temperature is accurately measured in 4 thermal infrared bands.

As the swath width of OCTS is about 1,400 km with a scanning mirror (west-east) and OCTS also scans south and north, it can observe the entire earth surface in 3 days. The spatial resolution is about 700 m. A satellite flying over the equator cannot get information on the ocean because of direct sunglitter at the sea surface. In order to prevent this sunglitter from interrupting the observation, OCTS can tilt its field of view along the track by +/−20 degrees.

It is likely that sensor performance is subject to unique space environmental factors, such as radiation, affecting detector sensitivity and mirror transmittance. OCTS has optical calibration functions using solar light and a halogen lamp so as to perform as planned in visible and near-infrared bands. For example, when the satellite passes over the north pole, solar light enters the solar calibration module so that deep space and a black body are observed every rotation of a mirror so as to calibrate differences between the lower temperature and ambient temperature. In addition, OCTS has electrical calibration functions to confirm performance of the electrical unit.

OCTS has two data transmission modes. All raw pixel data is transmitted via a Direct Transmission Subsystem (DT) or Inter Orbit Communication Subsystem (IOCS) in fine data transmission mode. One pixel data is sampled from every 6 km × 6 km area as typical data of the area and is downlinked to the local users (ex. fishery ships) via Direct Transmission to Local Users (DTL) in a coarse data transmission mode.

OCTS consists of a Scanning Radiometer Unit (SRU), which contains an optical system, and an Electrical Unit (ELU) for digital signal processing and other functions.

The scanning mirror reflects observation light to focus on the Optics Assembly. The mirror is electrically rotated per second and scans a line at forward and backward tilts within +/−20 degrees. In the Optics Assembly, light is converged through a Ritchie-Chretien telescope and then split into

two visible-near infrared bands and an infrared band through a dichroic filter. In the Visible and Near Infrared Detector Assembly, optical signals are converted electrically.

The infrared detector is cooled at 100 K by a large radiation cooler. It faces deep space at a temperature of 4 K, and emits the heat of the detector. The electrical signals are amplified by the specified gain in the Analog Signal Processor, and then converted to digital signals. Digital signals processed in the Digital Signal Processor are transmitted to the bus module.

The Advanced Visible and Near-Infrared Radiometer (AVNIR) is an optical sensor for measuring surface reflectance in 3 visible bands and 1 near-infrared band. The three visible bands are indicated by blue, green and red while the near-infrared band is suitable to observe vegetation. AVNIR has 4 multispectral bands of 16 m resolution and 1 panchromatic band of 8 m resolution.

AVNIR scans about an 80 km swath width along the cross track, using large linear array CCDs with 5,000 pixels (multispectral band) and 10,000 pixels (panchromatic band). The observation area is limited because of the narrow swath width. In order to compensate for this disadvantage, the pointing capability acquires a wide range of targets within +/−40 degrees around nadir. Similar to OCTS, AVNIR has optical and electrical calibration functions so that sensitivity can be monitored.

AVNIR is a high resolution optical sensor for a wide range of the Earth surface monitoring. The AVNIR data is used to understand vegetation and soil conditions in order to contribute to solving such phenomena as desertification and deforestation of tropical forests. In the land and urban utilization, the observation data of artificial structures and plant distribution profile contributes to creating a better living environment. Other observation data such as surface reflectance and radiance play a key role in evaluation of the energy balance of the earth. Given the fact that all environmental issues have been addressed at the local and regional levels, the AVNIR data with high resolution is valuable for the global environment observation community.

AVNIR is composed of two units, the Scanning Radiometer Unit (SRU)

which mainly consists of optical components and the Electronic Unit (ELU) which mainly processes the image data. The observation light is reflected by a pointing mirror with 0.5 degree drive angles. Optics in the SRU adopt a Catadioptric Schmidt optical system as a mirror while the spectrum is split into 4 multispectral bands and 1 panchromatic band by combined effects of an optical prism and interference filter.

After the optical signals are converted to electrical signals, Charged Coupled Devices (CCDs) scan those signals and output to the ELU. As CCDs have a capability of changing the integration time of the optical signals, sensitivity can be well maintained even in dark areas. The electrical signals are amplified in the Process Amplifier, and then converted to digital signals. The digital signals are processed in Image Processing Assembly and transmitted to the bus module. The multispectral observation data is compressed by about 10 % in order to reduce the transmission data rate.

The NASA Scatterometer (NSCAT) is an active microwave radar to measure winds over the oceans by transmitting Ku band microwave pulses (13.995 GHz) and receiving backscattered power from the ocean surface. The backscattered power is subject to changes in the direction of surface waves.

Multidirectional measurements can thus be used to solve wind speed and direction simultaneously by using algorithms derived from previous studies. NSCAT makes simultaneous measurements of the backscattered power with three different directions for each side along the track so that wind speed and direction of the sea surface are inferred. The antenna has a fan beam of 28 degrees (along the direction of beam radiation). The frequency of backscatter powers in changed by Doppler shift.

70 % of the entire earth's surface is covered by the ocean, which is the largest reservoir on the Earth and contains various thermal elements and greenhouse gases. It is likely that the ocean wind is deeply interrelated with the ocean changes on scales ranging from days to years, and the changes have great effects on climatic and environmental changes. Although the traditional measurements of ocean wind by ships and buoys are limited spatially and temporally, NSCAT has a wide instantaneous field of view and makes frequent observations. This observational data will contribute to

improvements of numerical weather forecasts and ocean circulation models, and a better understanding of the thermal balance in the upper ocean and environmental phenomena such as El Ninõ.

NSCAT consists of a RF subsystem, antenna subsystem and digital subsystem. The Traveling Wave Tube Amplifier (TWTA) in the RF subsystem produces a radar pulse with 13.995 GHz (frequency), 5 μsec (width), 62 Hz (repetition frequency). The pulse is fed to each antenna via a switch matrix. After the received signals are converted to the base band frequency level, they are transmitted to the digital subsystem.

The antenna subsystem consists of six independent fan beam antennas (two pairs of two antennas and two pairs of a single antenna). Each antenna configuration is two array antennas with wave guide slots (each for vertical and horizontal polarization). Two pairs of two antennas use one polarization while the other antennas do both polarizations. The antennas will be deployed after launch. The backscattered power, whose frequency is changed by a Doppler shift, are processed by the digital Doppler processor in the digital subsystem, and then transmitted to the bus module.

The Total Ozone Mapping Spectrometer (TOMS) is an optical sensor to measure the albedo of the earth's atmosphere in six narrow spectral bands. The total ozone content is interrelated with changes of solar radiation in the near ultraviolet wavelengths so that the spatial distribution of the total ozone can be inferred by observing several near UV bands. In addition, the TOMS observation data can be used to make quantitative estimates of sulfur dioxide gases in the near UV band.

The FOV of TOMS is 3×3 degrees (swath width: 42×42 km) and its scanning angle is $+/-55.5$ degrees (approx. 2,800 km of the ground surface) along the track. This wide swath width can cover the entire earth's surface in a day. The primary object of TOMS is to collect data on the global ozone content and sulfur dioxide continuously. Combined with monitoring of ozone depletion at the south pole, which has been recently addressed as one of the immediate environmental issues, and changes of ozone content after implementation of the CFC Protocol, the data can be used for quantitative analysis of factors related to ozone issues and the potential effects of volcanic eruptions on climatic changes.

TOMS consists of an optical subsystem, electrical subsystem and driving subsystem. The scan mirror observes the earth target along the cross track direction, and first focuses sunlight on the right side of a collimator. The spectrum, using holographic grating, is focused on the other side of the collimator and converted to electrical signals via an optoelectronic amplifier in the focal plane. Each spectrum is focused on the focal plane via Slit Plates and a Chopper.

The TOMS observation data will be calibrated by using one of three diffusers. The alternative use is to evaluate degradation of the diffuser by solar radiation. TOMS can also calibrate by using mercury phosphor and wavelength calibration is made by using a reflectance calibrator.

Polarization and Directionality of the Earth's Reflectances (POLDER) is an optical sensor for observing the surface reflectance in visible and near infrared bands. The major differences are that POLDER can observe an area from various directions and the spectral characteristics of the reflected solar light.

POLDER has a wide FOV lens with +/-43 degrees (along the track) × +/-51 degrees (cross track), using a pushbroom technique and an area can be observed from a maximum of 14 different directions. This observation helps understand angular characteristics of the earth's reflectance. In addition, POLDER can observe multi-polarization in multi-bands by rotating 16 types of interference filters and polarizers. Similar to the Total Ozone Monitoring Spectrometer (TOMS), the wide FOV of POLDER enables the entire earth's surface to be scanned four times within 5 days.

As mentioned above, POLDER can observe the reflectance of a given Earth target under different spectral, polarization and angular conditions. As a result, the atmospheric characteristics will be further understood. POLDER will help understanding the dynamics of the aerosols in the troposphere and the potential effects of clouds on the radiative balance of the Earth. POLDER consists of an optical subsystem and electronics subsystem. The optical subsystem consists of a telecentric lens, a filter wheel and a CCD array as a detector. The light is almost vertically incident on the filter wheel after the telecentric lens makes the optical correction. The CCD array (244 × 274 elements) can collect two-dimensional images. The filter

wheel has 16 filters and is rotated so that 16-channel images are acquired per one rotation.

The main functions of the electronics subsystem are to process imagery (*e.g.* A/D conversion), to handle telemetry/command for operation of the processed image and to control the filter wheel, the electric power and the heat.

The Improved Limb Atmospheric Spectrometer (ILAS) developed by the Environment Agency of Japan is a sensor to monitor polar stratospheric ozone. The object of ILAS is to monitor and study changes in the stratosphere, which are triggered by emissions of Chloro-fluoro carbons (CFC), and to check the effectiveness of world-wide emission controls of CFCs.

ILAS is a spectrometer, which observes atmospheric limb absorption spectrum from the upper troposphere to the stratosphere using sunlight (solar occultation technique). This covers the infrared region (850-1610 cm^{-1} and the near visible region (753 to 781 nm). ILAS is designed based on the LAS (Limb Atmospheric infrared Spectrometer), which was aboard EXOS-C (Ohzora, ISAS). It was developed to improve observation accuracy and also to detect minor constituents related to ozone hole chemistry. ILAS's observations are focused on the high latitude regions because of the geometrical relation of solar occultation events with the sun-synchronous orbit.

From these spectral observations, ILAS can measure the vertical profile of ozone hole related components: ozone (O_3), nitrogen dioxide (NO_2), aerosols, water vapor (H_2O), CFC11, methane (CH_4), nitrous oxide (N_2O), temperature, and pressure.

This dataset covers the key physical and chemical parameters which characterize ozone hole events: cooling at the polar lower stratosphere, PSC formation, the removal of nitrogen reservoirs, and ozone reduction by activated chemical chain reactions. ILAS will continue to contribute to research into stratospheric ozone changes into the late 1990's. ILAS measures the sequence of the limb atmospheric absorption spectrum, which pass the various tangent heights, at 12 Hz. The absorption (concentration) of each layer is derived from this spectral data stream. ILAS tracks the radiometric center of the solar disk. ILAS also has an IFOV position sensor

which measures the angle between IFOV and the top edge of the sun.

RIS (Retroreflector In Space) is a retroreflector for an earth-satellite-earth laser used in long-path absorption experiments. RIS has a corner-cube structure with an effective diameter of 50 cm. Measurements of ozone, CFC12, CO_2, CH_4, etc. are carried out using infrared pulsed lasers.

The Interferometric Monitor for Greenhouse Gases (IMG) is a sensor to monitor the earth's radiation balance, the temperature profile of the atmosphere, the temperature of the earth's surface, and physical properties of clouds. It was developed by the Japan Resources Observation System Organization (JAROS) for the Ministry of International Trade and Industry (MITI).

IMG will obtain detailed spectra of thermal infrared radiation from the earth's surface and atmosphere. The detailed spectra measured by IMG will be used to infer atmospheric concentrations of water vapor and other greenhouse gases.

A global increase in tropospheric concentrations of trace gases, such as carbon dioxide, methane, nitrous oxide, and chloro-fluoro-carbons (CFCs) has been noted. These increases have been brought about by human activities. Now however we have limited knowledge of the magnitude or distribution of the anthropogenic sources of these gases. Two sources whose magnitude must be investigated are deforestation and biomass burning. IMG will map the global and regional distribution of emission sources by measuring variations in the concentrations of trace gases. Moreover, natural sources and sink strengths of trace gases may vary widely with different terrestrial and oceanic ecosystems.

IMG is a Michelson-type Fourier Transform Spectrometer (FTS) with two mirrors and a beam splitter. The incident radiation received from the earth is divided by the beam splitter into two paths. One mirror is moved so that the two paths produce an interference pattern when they are recombined. The signal measured by the detector, the interferogram, can be Fourier transformed to obtain the incident spectrum. The diameter of the entrance aperture for the optics is 10 cm. The moving mirror is suspended on magnetic bearings and scans a 10 cm long path in 10 seconds.

8.5 TRMM

The hydrological cycle is a centerpiece of the Earth system and a key to understand its behavior. Among various components of the water budget, tropical rainfall, which comprises more than two-thirds of global rainfall, is the primary driver of the global atmospheric circulation as a heat source. Knowledge of tropical rainfall and its variability is therefore crucial to understand and to predict the global climate system.

In spite of its important role in our lives and global climate, the measurement of global rainfall is extremely difficult because of its high spatial and temporal variability, especially in the tropics and over oceans. Satellite remote sensing is probably the only way to provide reliable rainfall data on a global scale. TRMM is the first space mission dedicated to measuring tropical and subtropical rainfall though microwave and visible/infrared sensors, including the first space-borne rain radar that was developed in Japan.

More than half the solar energy incident upon the Earth is absorbed by the ocean and the land. This absorbed energy causes the evaporation of water from Earth surface. The water vapor condenses aloft and then falls as rainfall. The latent heat release in this process is the major energy source in the tropical atmosphere, and the driving force of the global circulation.

TRMM measurements are expected to provide a dataset that will be extremely valuable for understanding and for predicting global climate change and weather anomalies such as related to the sporadic "El Nino" phenomenon.

TRMM was proposed as a joint project between U.S. and Japan in 1986. In this joint project. Japan provided the Precipitation Radar (PR). H-II rocket and launched the TRMM satellite. The U.S. provided the spacecraft bus, four sensors except for the PR and operates the TRMM satellite. Telemetry and science observation data of TRMM are transmitted to the ground via NASA's Tracking and Data Relay Satellite (TDRS). In order to provide optimum opportunity for its various instruments to measure the average precipitation over the tropical latitudes, TRMM was launched into an orbit with: Altitude 350 km (approx.) Inclination 35 deg. (approx.).

TRMM was launched on November 28, 1997. Its mission instruments are the Precipitation Radar (PR), the TRMM Microwave Imager (TMI), the Visible and Infrared Scanner (VIRS), the Clouds and the Earth Radiant Energy System (CERES) and the Lightning Imaging Sensor (LIS). The major objectives of the PR are: provide three-dimensional rainfall structure, achieve accurate rainfall measurement over land and water and improve accuracy of TMI measurements by providing better rain structure information. PR performance characteristics are shown below.

Parameter	Value
Observation Band Frequency	13.796 and 13.802 GHz (Two channel frequency agility)
Pulse Repetition Frequency	2776 Hz
Horizontal Resolution	4.3 km
Swath Width	220 km
Pulse Width (Each frequency)	1.67 μsec
Beam Width	0.71° at nadir
Scan Angle (Crosstrack)	17°

INSTRUMENT RESOURCE REQUIREMENTS

Weight	: 475 kg
Power	: 250 Watts average
Data rate and storage	: 94 kbps

The TMI, designed for NASA by Hughes, is a five-channel, dual-polarized, passive microwave radiometer. Microwave radiation is emitted by the Earth's surface and by water droplets within clouds. However, when layers of large ice particles are present in upper cloud regions – a condition highly correlated with heavy rainfall – microwave radiation tends to scatter. The TMI will detect radiation at five frequencies chosen to discriminate

among these processes, thus revealing the likelihood of rainfall. The key to accurate retrieval of rainfall rates by this method is the deduction of cloud precipitation consistent with the radiation measurement at each frequency. The TMI data, supported by PR data, will be the primary data set for precipitation measurements.

TMI performance characteristics are shown below.

Band	1	2	3	4	5
Band Frequency (GHz)	10.7	19.4	21.3	37	85.5
Polarization	H/V	H/V	H	H/V	H/V
Horizontal Resolution(km)	38.3	18.4	16.5	9.7	4.4
Beam Width (Deg)	3.95	1.9	1.6	1.0	0.45
Swath Width(km)	790	790	790	790	790

INSTRUMENT RESOURCE REQUIREMENTS

Weight	: 62 kg
Power	: 72 Watts average
Data rate and storage:	9 kbps

The VIRS, designed for NASA by Hughes SBRS, is the third component of the primary three-instrument rain package. The five-channel cross-track scanning radiometer will measure radiance in five bands from the visible though the infrared spectral regions. VIRS will combine with the PR to provide information on the variation of rain-water content with altitude, valuable for determination of the vertical profile of condensation heat release. The VIRS data will also be used in conjunction with the secondary CERES instrument data to determine cloud radiation. The VIRS will provide a link between measurements made by the TRMM rain package and those made simultaneously by the visible and infrared radiometers on operational polar and geostationary satellites. VIRS performance characteristics are shown below.

Parameter	Value
Observation Band Wavelength (μm)	0.63, 1.6, 3.75, 10.8, and 12 (Five channel frequency agility)
Horizontal Resolution	2 km at nadir
Instantaneous Field of View (IFOV)	6.02 milliradians
Swath Width (Crosstrack)	720 km
Data Rate	50 kbps

INSTRUMENT RESOURCE REQUIREMENTS

Weight	: 55 kg
Power	: 53 Watts average
Data rate and storage	: 50 kbps

The CERES instrument, developed for NASA by TRW, is a broadband radiometer, which will provide data on the Earth's radiation budget and atmospheric radiation from the top of the atmosphere to the surface of the Earth. The CERES instrument has the capability of scanning the Earth continuously in one of two modes. The first is the normal or cross-track mode that scans back and forth across the Earth, pausing to view space on either side. The other mode is a biaxial scan mode that adds an angular oscillation between 90 ° and 270° while simultaneously scanning in the normal mode. CERES performance are shown below.

Parameter	Value
Wavelength (μm)	0.3 to 5 (Short Wave) 8 to 12 (Long Wave) 0.3 to 50 (Total)
Instantaneous Field of View (IFOV)	8 $\times$ 16 km at nadir
Swath Width	Full Earth plus sky
Scan Angle	+82°
Horizontal Resolution	25 km at nadir
Data Rate	9 kbps

INSTRUMENT RESOURCE REQUIREMENTS

Weight	: 47 kg
Power	: 47 Watts average
Data rate and storage:	9 kbps

The LIS instrument, developed by NASA, is an optical staring telescope and filter imaging system that will acquire and investigate the distribution and variability of both cloud-to-cloud and cloud-to-ground lightning over the Earth. The LIS measurements will be used with PR, TMI, and VIRS data to investigate the correlation of the global incidence of lightning with rainfall and other storm properties. LIS performance characteristics are shown below.

Parameter	Value
Observation Band Wavelength	0.7774 μm
Storm Spatial Resolution	4 km at nadir
Field of View	$80° \times 80°$
Data Rate	6 kbps

INSTRUMENT RESOURCE REQUIREMENTS

Weight:	22 kg
Power :	42 Watts average

8.6 Future Plans

8.6.1 ADEOS-II

The Advanced Earth Observing Satellite-II (ADEOS-II) which is the successor to the Advanced Earth Observing Satellite (ADEOS) mission will

take an active part in research of global climate changes, practical utilization for weather phenomena, fishery, etc., such as seizing the mechanism of global environmental changes including global warming.

The Committee of Earth Environmental Observation aims at contributing to studying global climatic changes and ADEOS-II is recommended to be positioned as a satellite with the main objectives of clarifying distributions of chlorophyll, vegetation cover, etc., and to play an important role in the Global Energy and Water Experiment (GEWEX) and the Climatic Variability and Predictability (CLIVAR) of the World Climate Research Programme (WCRP).

The Advanced Microwave Scanning Radiometer (AMSR) will observe various physical parameters concerning water (H_2O) by receiving weak microwaves naturally radiated from the Earth's surface and atmosphere (for example, water vapor content, precipitation, sea surface temperature, sea surface wind, sea ice, etc.) regardless of day or night, or clouds.

AMSR is a radiometer with eight frequency bands from 6.9 GHz to 89 GHz, respectively, observing vertical and horizontal polarized waves except at the two frequency bands near 50 GHz. It acquires radiance data by scanning the Earth's surface conically and mechanically rotating its antenna along the satellite flight path. Also, AMSR has a function and high-temperature calibration source to acquire radiance temperatures in deep space (about 2.7 K) for calibrating observation data.

The aperture diameter of AMSR's antenna is 2 m and its instantaneous visual field is about 5 km (89 GHz). It scans conically with an constant angle of incidence on the Earth's surface (a nominal angle: 55 degrees) and minimizes the effect of sea surface wind upon observation data and to have a swath width of about 1600 km.

The Global Imager (GLI) is an optical sensor aiming at observing globally and frequently the reflected solar radiation from the earth's surface including land and ocean, and cloud, and the infrared radiation for measuring the physical parameters such as chlorophyll, dissolved organic substance, surface temperature, vegetation distribution, vegetation biomass, distribution of snow and ice, and albedo of snow and ice, etc. These data may be used for grasping the global circulation of carbon, monitoring clouds, snow,

ice, and sea surface temperature, and understanding the primary marine production. GLI is an advanced type of the Ocean Color and Temperature Scanner (OCTS) sensor on-board ADEOS for further expansion of observation.

GLI has 22 bands in the visible and near-infrared region (VNIR), 5 bands in the short-wave length infrared region (SWIR), and 7 bands in the middle and thermal infrared region for its multispectral observation. Although the ground resolution at nadir is 1 km, some of the bands in VNIR and SWIR have a resolution of 250 m at nadir, which will be used for observing vegetation and clouds. The observation region by mechanically scanning is 12 picture elements (12 km) to the forward direction and 1600 km in the cross-track direction.

NASA's SeaWinds scatterometer will provide high accuracy wind speed and direction measurements over at least 90 % of the ice-free global oceans every 2 days. SeaWinds will provide a set of long term contiuous wind data for studies of ocean circulation, climate, air-sea interaction and weather forecasting.

SeaWinds is a follow-on to the NASA Scatterometer (NSCAT) which is a sensor on ADEOS and will, like NSCAT, provide measurements of ocean surface winds in all weather and cloud conditions. The SeaWinds will use a one meter diameter dish antenna with two beams rotated about the satellite nadir axis at 18 RPM. SeaWinds radiates and receives microwave pulses at a frequency of 13.4 GHz across a 1800 km wide swath.

Scatterometers use a highly indirect technique to measure wind velocity over the ocean. Changes in the wind velocity cause changes in ocean surface roughness, modifying the radar cross section of the ocean and the magnitude of the backscattered power. Multiple collocated measurements acquired from several directions can be used to solve wind speed and direction simultaneously.

The Improved Limb Atmospheric Spectrometer-II (ILAS-II) developed by the Environment Agency of Japan is a sensor to monitor high-latitude stratospheric ozone. The objectives of ILAS-II are to monitor and study changes in the stratosphere which are triggered by emissions of chloro-fluoro-carbons (CFC), and to evaluate the effectiveness of world-wide emis-

sion controls of CFCs. ILAS-II is a spectrometer which observes the atmospheric limb absorption spectrum from the upper troposphere to the stratosphere using sunlight as a light source (solar occultation technique).

The spectrometer covers the infrared region (2–13 μm) and the near visible region (753 to 784 nm). ILAS-II was designed to improve observation accuracy and cover wider spectral ranges than ILAS (aboard ADEOS planned for 1996 launch by NASDA) which was based on LAS aboard EXOS-C (Ohzora, ISAS, 1984). ILAS's observations are focused in the high latitude regions because of the geometrical relation of solar occultation events with the sun-synchronous orbit. From these spectral observations, ILAS-II can measure the vertical profiles of species related to ozone hole phenomena: ozone (O_3), nitrogen dioxide (NO_2), aerosols, water vapor (H_2O), CFC11, methane (CH_4), nitrous oxide (N_2O), chlorine nitrate ($ClONO_2$), temperature, and pressure.

The POLDER (Polarization and Directionality of the Earth's Reflectances) instrument will observe the polarization, directional and spectral characteristics of the solar light reflected by aerosols, clouds, oceans and land surfaces.

POLDER is a pushbroom, wide field of view, multi-band imaging radiometer/polarimeter developed by CNES. Multi-angle viewing is achieved by the along-track migration at the spacecraft velocity of a quasi-square footprint intercepted by the total instantaneous 114-degree wide field of view. This footprint is partitioned into 242 $\times$ 274 elements of quasi-constant 7 km$\times$6 km resolution, imaged by a CCD matrix in the focal plane (fig). Simultaneously, a filter/polariser wheel rotates and scans eight narrow spectral bands in the visible and near infrared (443, 490, 565, 665, 763, 765, 865 and 910 nm), and three polarization angles at 443,665 and 865 nm.

8.6.2 ALOS

Two programs are in the development phase for future launch. One is a satellite called ALOS (Advanced Land Observation Satellite) and will carry 3 sensors. One is an L band synthetic aperture called PALSAR (Phased

Array L band Synthetic Aperture Radar). PALSAR has an active phased array antenna, and has many capabilities, like variable incidence angle, variable resolution, scan SAR capability and multi polarization capability.

ALOS has two optical sensors, *i.e.*, AVNIR-2 and PRISM. AVNIR-2 (Advanced Visible and Near Infrared Radiometer) is a follow on of AVNIR on ADEOS and has 4 bands with 10 m resolution. PRISM is a panchromatic sensor with 3 telescopes, which will enable PRISM to take 3 direction (nadir, fore and aft) stereo pairs simultaneously. The resolution of PRISM is very high (2.5 m) with rather narrow swath (35 km).

The largest characteristics of ALOS are its capability to store and transmit quite a large data volume. It can acquire and transmit all the data of the global land area.

ALOS is planned to be launched in 2002, and for the study of hydrology, it is expected that the multi polarization characteristics of PALSAR can provide useful information on soil moisture.

8.6.3 SMILES

Another project on going is a sensor development for ISS (International Space Station). This sensor is called SMILES (Super-conducting Millimeter wave Emission Spectrometer) and measures millimeter wave emission from atmospheric constituents. In order to achieve high sensitivity, the main detector is composed of a SIS (Superconductor-Insulator-Superconductor) device and cooled down to 4 K by an active cooler. The planned launch date is year 2003, and SMILES will provide information on stratospheric chemical processes.

8.6.4 Other programs

Several other programs are under study. The most advanced one is MDS-2 and will carry a Mie scattering lidar, which will provide information on aerosols and clouds.

As a follow on of ADEOS-II, the ADEOS3 project is in the study phase. ADEOS3 will be composed of 2 satellites, ADEOS3-a and ADEOS3-b.

ADEOS3-a will carry two sensors, ILAS3 and ODUS. ILAS3 is a Fourier transform spectrometer with a Michelson interferometer and uses a sun occultation measurement configuration. It can measure not only ozone and related atmospheric species, but also greenhouse gases like methane, etc. ODUS is similar TOMS (Total Ozone Mapping Spectrometer), but has higher spectral and spatial resolution. ADEOS3-a will be on an oblique orbit with around 70 degree inclination and 600 km altitude.

On the other hand, ADEOS3b will be on a sun-synchronous orbit similar to ADEOS-II. It will carry SGLI, AMSR2, SeaWinds2, POLDER and ATRAS. SGLI is a follow-on of GLI on ADEOS-II and is a 36 channel spectrometer. AMSR2 is a follow-on of AMSR on ADEOS-II and is a microwave scanning radiometer. SeaWinds2 is a follow-on of SeaWinds on ADEOS-II and will have a higher spatial resolution than SeaWinds. ATRAS (Atmospheric Radiation Spectrometer) is a follow on of IMG on ADEOS and will have scanning capability with the same or better radiometric performance.

Part II

Outlines of Other Lectures

Chapter 9

Microwave Remote Sensing for Hydrology

Toshio Koike
Hydrosphere and Atmosphere Interaction Laboratory (HAIL)
Department of Civil and Environmental Engineering
Nagaoka University of Technology
Phone: +81-258-47-9667 fax: +81-258-47-9673
E-mail: tkoike@nagaokaut.ac.jp

9.1 Advantages of microwave for hydrology monitoring

Microwave remote sensing can directly measure the dielectric properties which strongly depends on the liquid water content. Especially, the large value of the real part of the dielectric constant and the relatively small of imaginary part of water around at 1 GHz mean that microwave has large sensitivity to soil moisture of surface layer to some extend. The longer wave length is also one of the advantages of microwave remote sensing of land surface hydrology. It is long enough to reduce the scattering effect of cloud particles and to make microwave sensors a useful all-weather sensor. The

wave length in the microwave region has sensitivity to the scattering effects of snow grains and leaves. Microwave remote sensing has a potential of the measurement of snow water equivalent and bio-mass. By using higher frequency channel, scattering effects of rain drops can also be detected. The independence of sun as a source of illumination is also one of the important reasons for using microwaves. We can obtain the data even at night. This advantage is more important in the case of non-sunsynchronous observation.

9.2 Soil moisture

In general, at a plane interface between two semi-infinite media, the emisivity is equal to one minus the Fresnel power reflectivity which is calculated by using dielectric constant of the media and incident angle. The temperature dependence of the emissivity of the smooth water surface is calculated by using the SSM/I specifications; frequencies, polarization and incident angle. The emissivity is larger at the higher frequency than at the lower one for both polarization. The normalized discrepancy between the emissivities at different frequencies can be used as an index for surface wetness. Based on the airborne experiments, the combination of 36.5 and 6.9 GHz shows the best performance for soil moisture measurement in the available sensors in 2000. An algorithm for soil moisture mapping in permafrost regions was developed by using two images of L-band Synthetic Aperture Radar (SAR), one in winter and the other in summer. The algorithm is based on a relationship between two surface roughness parameters, r.m.s. height (σ) and correlation length (l), and the scattering model composed by the Integral Equation Method (IEM) and formulation of volume scattering from inhomogeneous medium. The backscattering coefficient of the ground surface is affected not only by soil moisture but also by the other factors such as surface roughness, vegetation and soil composition. At first, the σ-l relationship is identified by using filed measurements. Then the surface roughness distribution is calculated from the SAR image obtained in very dry season. Then, surface soil moisture distribution in wet season is de-

rived by applying the scattering model and the estimated surface roughness distribution to the wet season image.

9.3 Snow

In order to understand the relationship between the brightness temperature and snow water equivalent, a radiative-transfer theory based on a scattering dielectric layer over a homogeneous half-space is applied to the emission from snowpack and underlying soil. The total radio brightness observed at radiometer is the sum of the direct component and the diffuse component. The direct component consists of the reflected sky radiation and the thermal radio emission from snowpack and soil. The diffuse field results from radiation scattered from the direct field and diffuse field. To estimate the direct component observed at radiometer, five sets of the nodal equations at the snow surface and the interface between the snow and soil are solved. And as far as the intensity of the diffuse radiation, these differential equations which mean that diffuse component is reduced by extinction and is increased by the scattering emission from the diffuse and direct field. The Rayleigh scattering coefficient and phase function are used in this model. The dependence of the grain size and snow depth on the direct field , the diffuse field and total brightness temperatures at two frequencies of SSM/I 37 and 19 GHz can be calculated by using radiative transfer model. The direct field brightness temperature for the lager grain size decreases more rapidly than one for the smaller grain size because of the stronger effect of the scattering extinction for the larger gain size. The opposit relationship appears in the diffuse field brightness temperature. Then the total brightness temperature for the lager grain size decreases more rapidly than one for the smaller grain size and reaches constant value and loses the sensitivity to snow depth. And the sensitivity to grain size and snow depth is more remarkable at the higher frequency than at the lower frequency. So the discrepancy of the brightness temperature at two frequencies can be used as an index of snow depth. However there is large dependence of the index on grain size. There is limitation of application for the larger grain

size. If grain size and snow density can be assumed, a diagram which describes snow depth and physical temperature of snow pack can be obtained by using brightness temperature at 19 and 37 GHz. By overlaying the data from satellite on the diagram, snow depth and physical temperature can be estimated.

Chapter 10

SAR and its Application for the Hydrology and Vegetation

Seiho Uratsuka
Communications Research Laboratory
Ministry of Posts and Telecommunications
4-2-1 Nukuikitamachi, Koganei, Tokyo 184-8795, Japan
Phone: +81-42-327-7536, fax: +81-42-327-5521
E-mail: pata@crl.go.jp

10.1 Introduction

Synthetic Aperture Radar (SAR) is a space-borne or airborne microwave radar which can observe the ground surface as an image whenever it is cloudy or night time. The SAR data are available since the 1990s. JERS-1, ERS-1/2 and RADARSAT are carrying SAR with about 30 m resolution. In early 2000s, European ENVISAT and Japanese ALOS satellites will be launched. They also board SAR with advanced technology (Scan-SAR and multi-polarization). These satellites aim at the application to the geol-

ogy, mine survey, oceanography, ice content, hydrology, and vegetation. The SAR image is just look like an aerial photograph, but projection and brightness of SAR is very different from the aerial photo. Projection of ground is emphasized ground topography. Brightness of image should be investigated based on the microwave scattering characteristics, which is different from optical scattering because of longer wavelength than optical one. Brightness depends on wavelength, polarization, surface roughness, dielectric condition (soil moisture), structural vegetation, angle of incidence and so on.

The aim of the application to vegetation is monitoring forest destruction, biomass measurement, forecasting harvest amount and other agricultural purposes. Algorithms have been developed worldwide. One of them is classification, which is a discrimination of crops, vegetables, trees, and non-vegetation area. Seasonal variation of them is also important item.

In the hydrological science, the discovery of ancient Nile River in Egypt by the Shuttle Imaging Radar-A (SIR-A: SAR experiment on the Space Shuttle in 1981) is a very famous success of SAR. However, the direct measurement of the soil moisture used only SAR data is not an easy problem. Snow cover extent is also. This application should be investigated with the combination of other sensors and knowledge of vegetation

References

[1] Curlander, J. D. and R. N. McDonough, Synthetic Aperture Radar: System & Signal Processing, *John Wiley & Sons*, 1991.

[2] Oliver, C. and S. Quegan, Understanding Synthetic Aperture Radar Images, *Artec House*, 1998.

[3] Ulaby, F. T. and C. Elachi ed., Radar Polarimetry for Geoscience Applications, *Artec House*, 1990.

[4] Ulaby, F. T., R.. K. Moore, and A. F. Fung, Microwave Remote Sensing: Active and Passive **Vol. II**, *Artech House*, 1986.

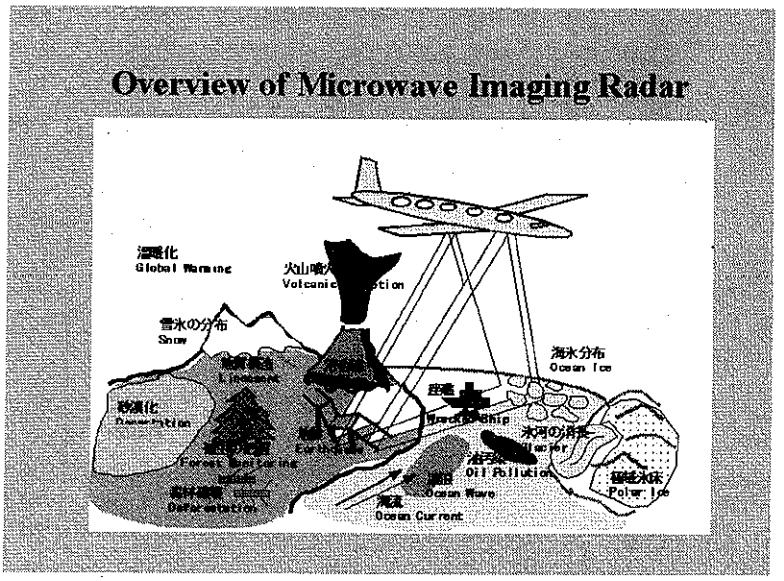

Figure 10.1: The SAR is strongly expected in various field in the global environmental monitoring and disaster such as vegetation, deforestation, glacier extent, and so on shown in Figure, because of its transparency of clouds or smoke from volcano or large fire.

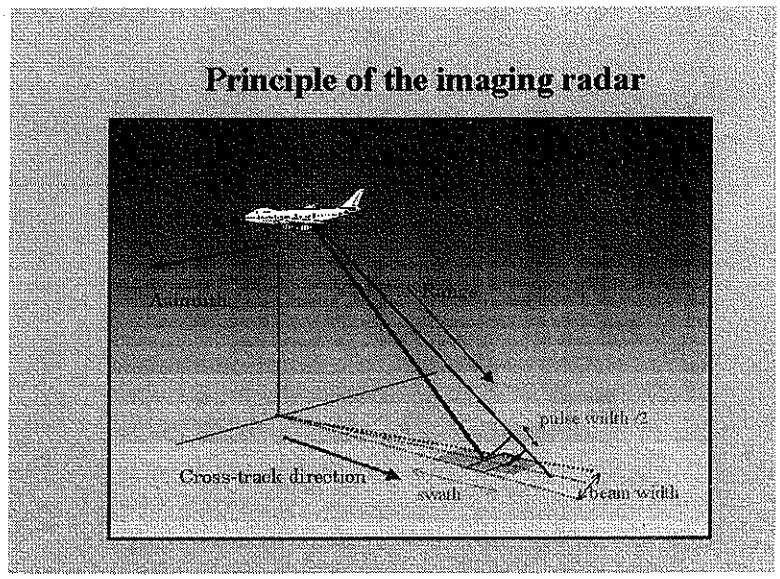

Figure 10.2: The microwave radar obtains the echo from the surface of the earth along cross-track direction. The distance in this direction is proportional to the range distance from the radar, and also proportional to the return time of the echo. Therefore, the radar echo becomes a line profile of surface. Because radar moves in the direction of the azimuth, the sweep of the profile produce a two dimensional image. Resolution in the range direction is determined depending on the pulse width of the radar as shown in Figure. The resolution of azimuth direction depends on beam-width.

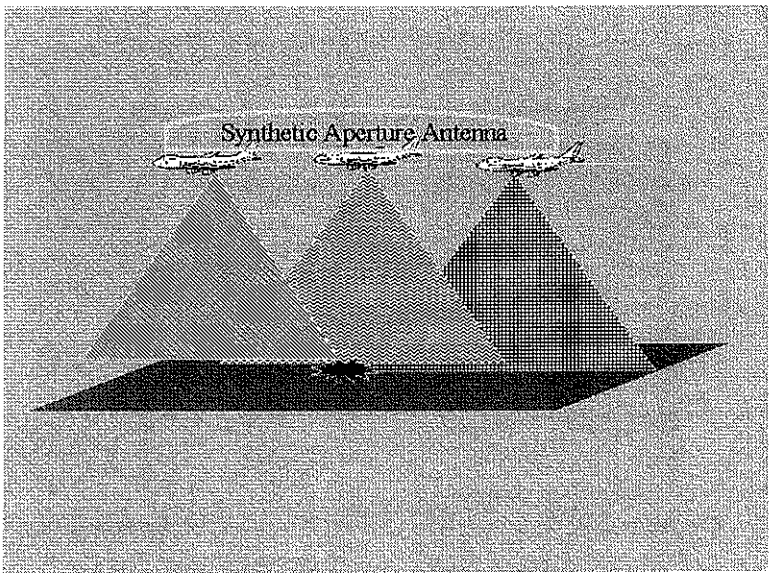

Figure 10.3: Large antenna is necessary to obtain high azimuth resolution. However, platform (aircraft or spacecraft) payload capacity is limited. The synthetic aperture radar overcomes the problem by constructing an equivalently large antenna. The data taken by small (wide-beam) antenna which looks a target for long period.

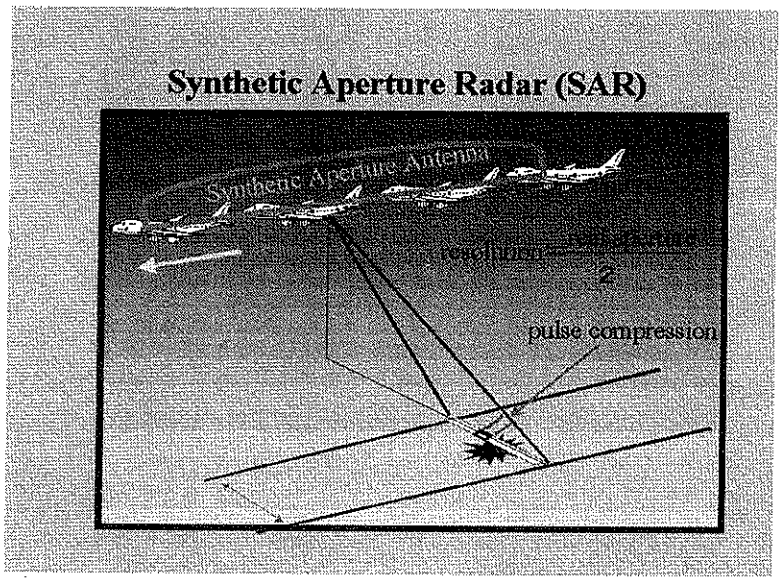

Figure 10.4: The resolution of SAR in azimuth direction is principally half of the real aperture. The resolution in cross-track is half of the pulse length, which is usually very short using pulse compression technique.

Satellite-borne SAR

Satellite	ERS-1 /ERS-2	JERS-1	RADARSAT	ENVISAT-1	ALOS
Launch	1991.4 /1994	1992.2	1995.11	2000.5	2002.8
Organization	ESA	NASDA	CSA	ESA	NASDA
Orbit Altitude	785km	568km	793-821km	800km	700km
Orbit inclination	98.5	97.7	98.6	98.55	
Frequency	5.3GHz C-band	1.275GHz L-band	5.3GHz C-band	5.3GHz C-band	1.27GHz L-band
Polarization	VV	HH	HH	Multi-Polarization	Polarimetry
Incidence angle	23	38.7	10-60	14-45	18-60
Swath	100km	75km	50-500km	50-405km	50-350km
Resolution	30m	18m	9-147m	30m	10/20/100
Peak power	4.8kW	325W	5kW	1.3kW	
Band width	19MHz	15MHz	11.6/17.3/30.0 MHz		28/14MHz
Antenna (El. x Az.)	1m x 10m	2.2m x 12m	1.5m x 15m Active phased array	Active phased array	Active phased array
Comments			Scan-SAR	Scan-SAR Multi-polarization	Scan-SAR Polarimetry Simultaneous observation with optical sensor (AVNIR-2)

Figure 10.5: List of the current and future space-borne SAR. Since 1992, the SAR data is available. Multi-functional and higher resolution SARs are expected after 2000.

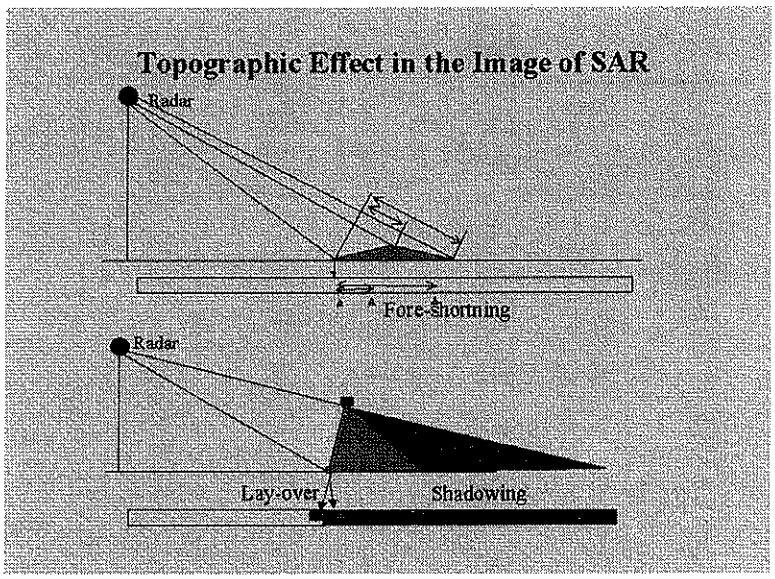

Figure 10.6: The cross-track distance in the radar image is a projection of the distance from the radar. Therefore, the topographic images are affected by layover, foreshortening, and shadowing.

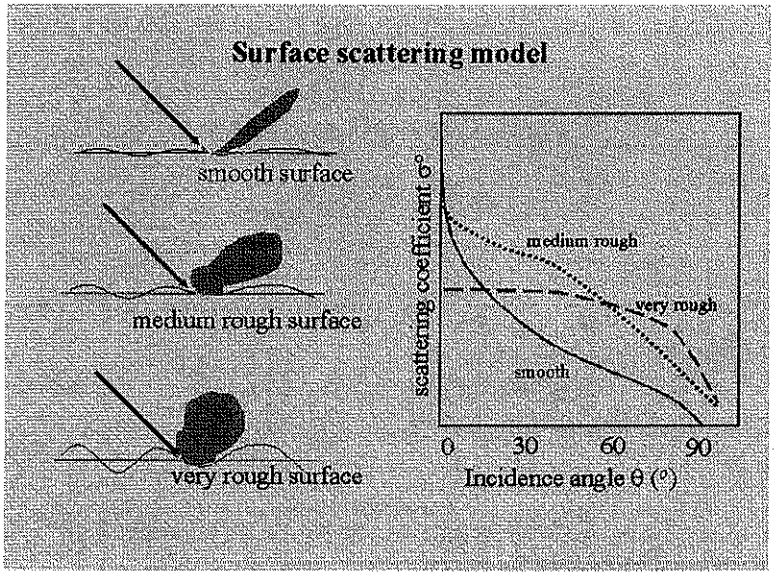

Figure 10.7: Incident radio wave to the surface is scattered to the wide direction. When the surface is very smooth, the scattered wave is concentrated in the reflected direction, and back scattering in large incidence is very small. When the surface is very rough, the backscattering component is not small. The general relation between backscattering amount and incidence angle is shown in the Figure.

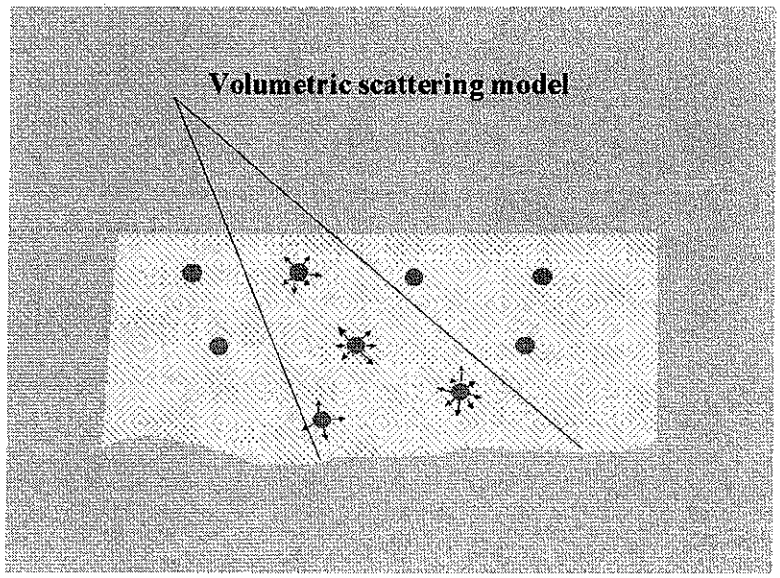

Figure 10.8: Another scattering mechanism is a volumetric scattering. In this case, the incidence angle dependence is very small. Scattering from snow is mixed of this volumetric and surface scattering.

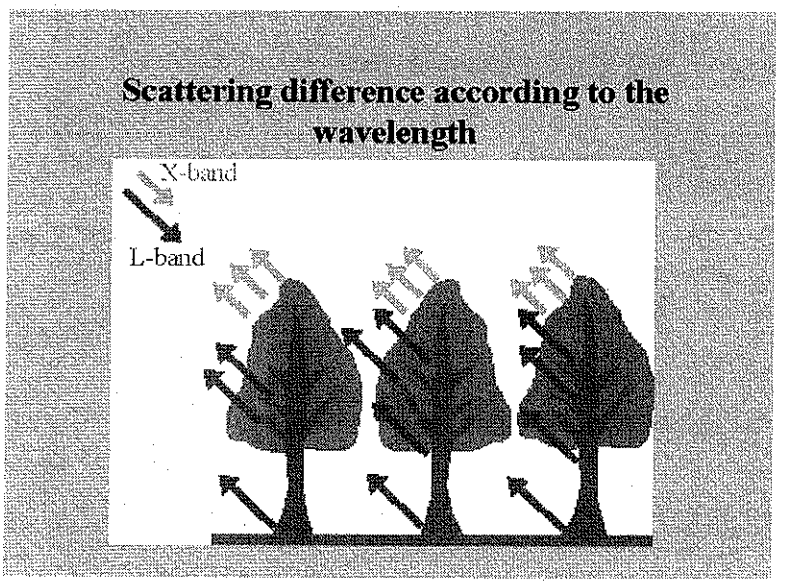

Figure 10.9: The penetration depth to the vegetation, dry soil, or snow is dependent on the microwave wavelength. Shorter wavelength (X-band in Figure) is scattered only from the surface of the leaves, but longer wave is scattered anywhere. The difference of two wavelengths led us to estimate the volume of the trees.

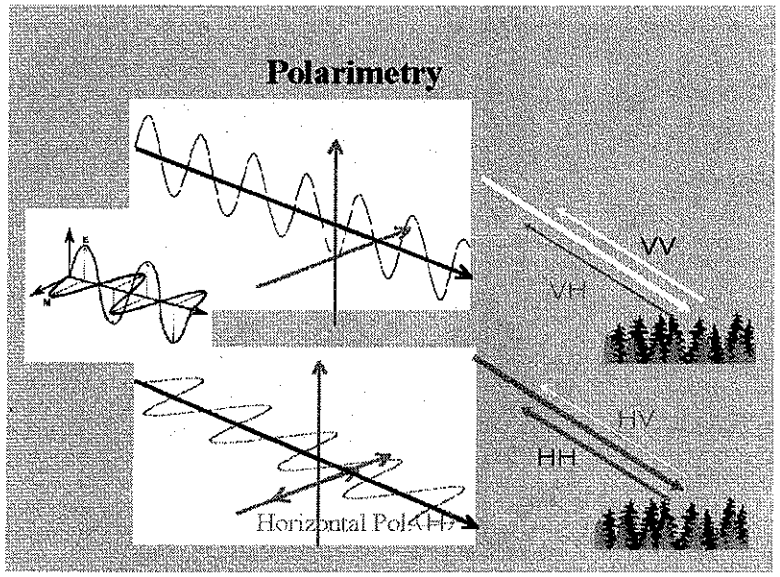

Figure 10.10: Radar can transmit and recieve any polarization radiowave according to the antenna. Usually, radar uses the combination of Vertical (V) or Horizontal (H) linear polarization. The surface characteristics have the own polarization response. All combinations of V and H polarization in transmittion and reception can be used to characterize the surface condition.

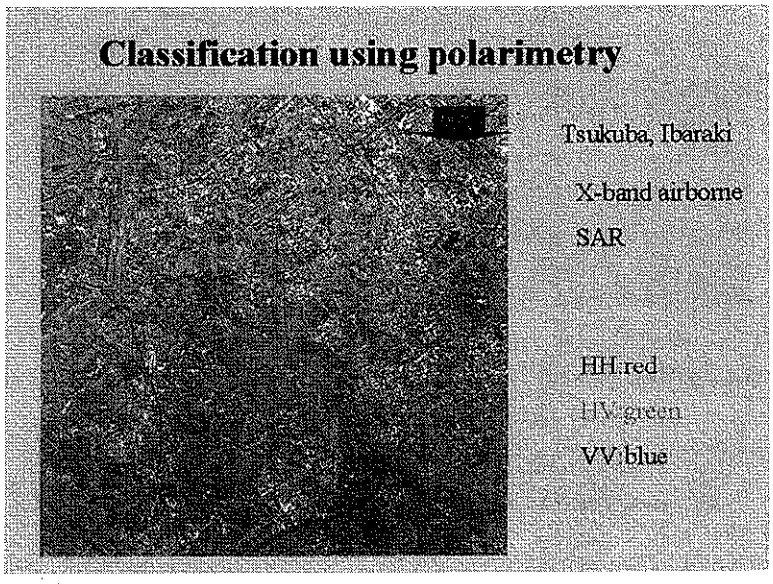

Figure 10.11: This image shows the polarization characteristics.

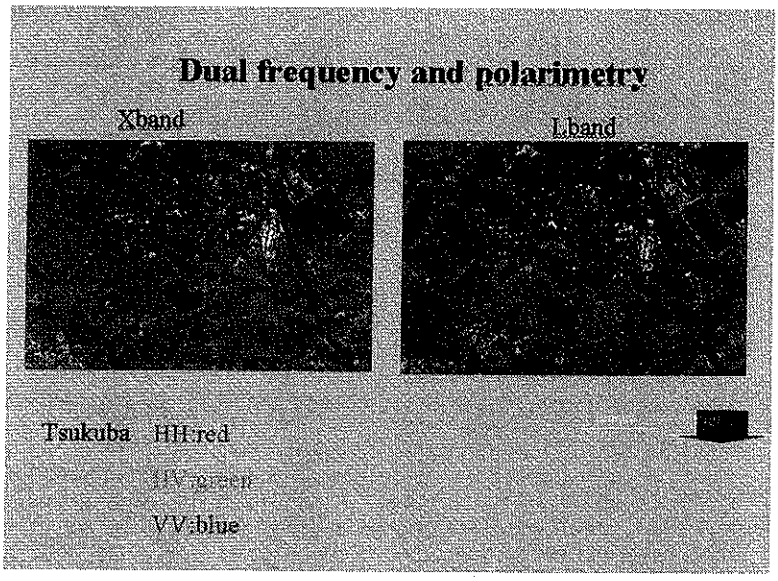

Figure 10.12: Both of images are processed in the same way as Figure 10.11. However, left is X-band (3.14 cm wavelength) image and, right is L-band (23 cm wavelength). The difference of these two images shows the different underground condition of rice field.

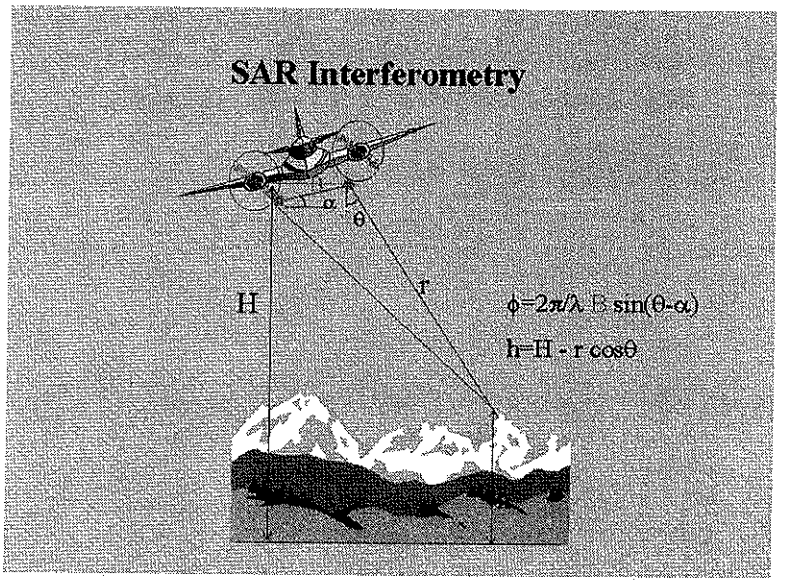

Figure 10.13: (Topics: Interferometry.) SAR image can resolve the topography using two antennas. The phase difference of the received signal between two antennas can be used to detect very fine difference of geographical height.

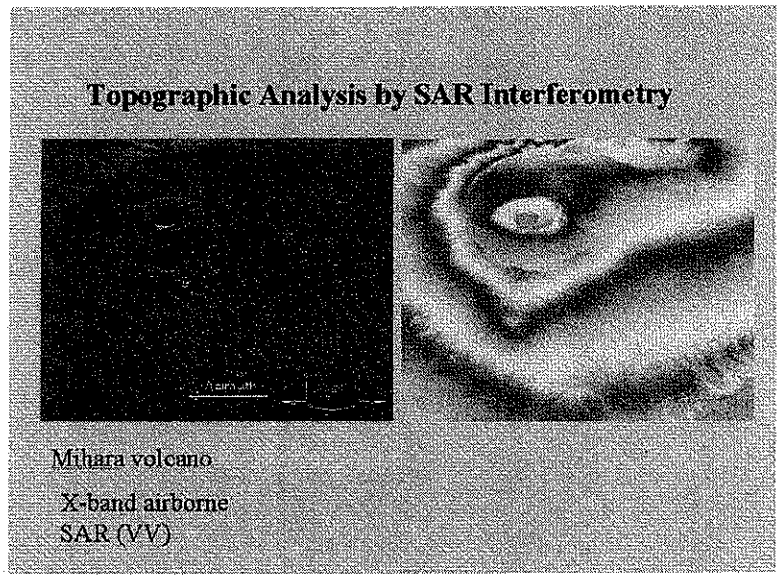

Figure 10.14: The left image is X-band airborne SAR of the volcano Mihara-yama. Right image shows the phase difference of the two antennas attached the aircraft. The phase pattern in the figure is corresponding to the topography.

Chapter 11

Windprofiler Radar

Yuichi Ohno
Communications Research Laboratory
Ministry of Posts and Telecommunication
4-2-1 Nukui-Kitamachi, Koganei, Tokyo 184-8795, Japan
E-mail: ohno@crl.go.jp

11.1 Windprofiler radar

Windprofiler is a Doppler radar for measuring wind from the ground. It can measure wind vectors above the radar site by using the clear-air echoes. Clear-air echo is caused by fluctuatiion of the refractive index whise scale is half of the radar wavelength (Bragg scattering). From the Doppler shift of along a certain beam direction, the line-of-sight velocity along the radar beam can be measured. Assuming horizontal homogeneity of wind field, three components of wind vectors can be measured by at least three beam observations. Observable height range if radars depends on transmit power, antenna size and radar frequency.

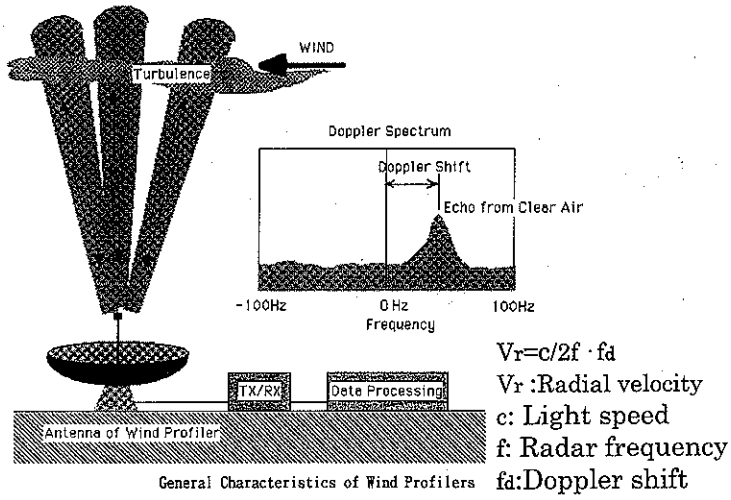

Figure 11.1: Concept of wind measurement by a windprofiler radar.

Radar Frequency	VHF Radar (50MHz)	UHF Radar (400MHz)	UHF Radar (1GHz)
Observable Range	2-20 km	0.5-17 km	0.2-3 km
Antenna Size	100*100 m	10*10 m	1*1 m
Transmit Peak Power	1000-100 kW	10 kW	1 kW
Example	MU Radar	NOAA Profiler Network MRI Wind Profiler	CRL Wind Profiler RASC BLR RADIAN Co. LAP-3000

Table 11.1: General specifications of three typical windprofiler radars.

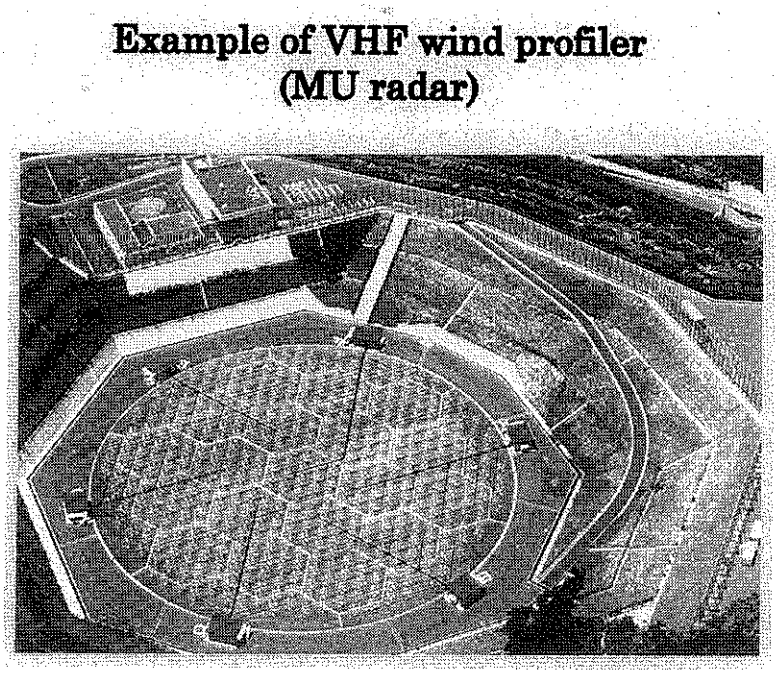

Figure 11.2: A picture of a VHF (50 MHz) windprofiler radar. This radar is belonging to Kyoto University. The diameter is about 100 m.

Basic Parameters of the MU radar

Location	Shigaraki, Shiga, Japan (34° 51'N, 136° 06'E)
Radar system	monostatic pulse radar;active phased array system
Operation frequency	46.5MHz
bandwidth	1.65MHz
Antenna	circular array of 475 crossed yagis
aperture	8,330 m^2 (103 m in diameter)
beam width	3.6 degree
Transmitter	475 solid state amplifiers
peak power	1 MW
average power	50 kW
Pulse repetition frequency	2.5 kHz maximum
Pulse width	1~500 micro sec
Receiver dynamic range	1.65MHz
Polarization	linear and circular

Table 11.2: System parameters of the VHF radar in Fig. 11.2.

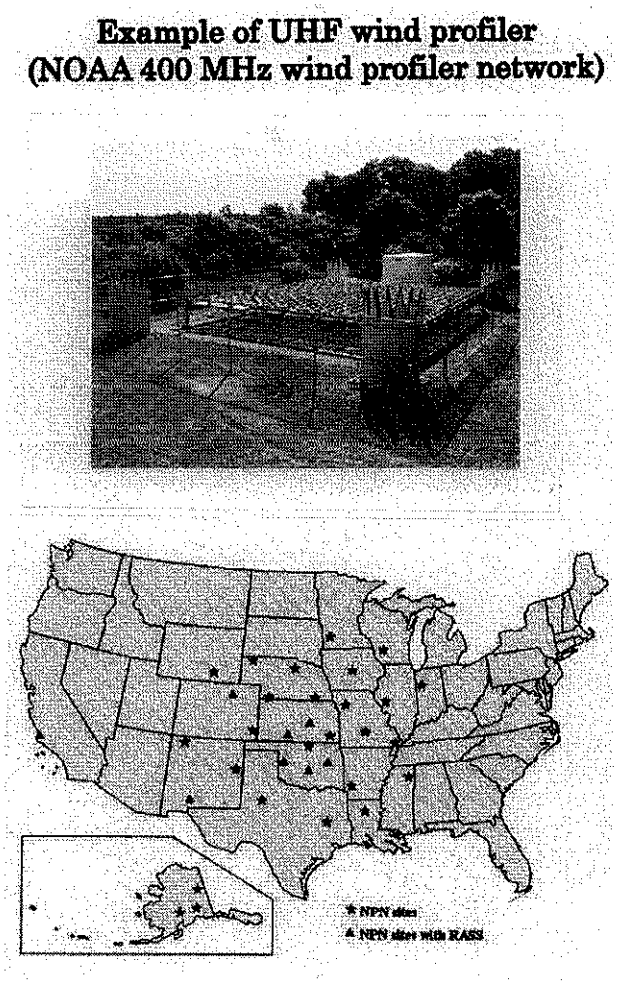

Figure 11.3: A picture and system parameters of a UHF (1.3 GHz) radar developed by the Communications Research Laboratory.

Example of UHF wind profiler (1357MHz CRL wind profiler)

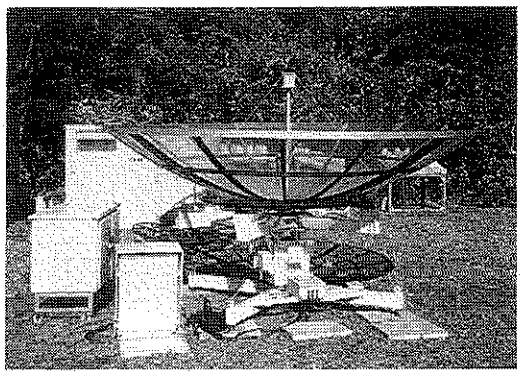

Characteristic of CRL wind profiler

Frequency	1357.5 MHz
Transmit peak power	1 kW
Pulse width	1 μsec
Inter pulse period	50 μsec
Time resolution	5 minutes
Antenna type	Parabolic Ref.
Antenna diameter	4.2 m
Antenna gain	33 dBi
Beam direction	Vertical (0°,0°)
(Azimuth, Zenith)	East (90°,8°)
	North (0°,8°)

Figure 11.4: A picture and system parameters of a UHF (1.3 GHz) radar developed by the Communications Research Laboratory.

Example of CRL wind profiler observation

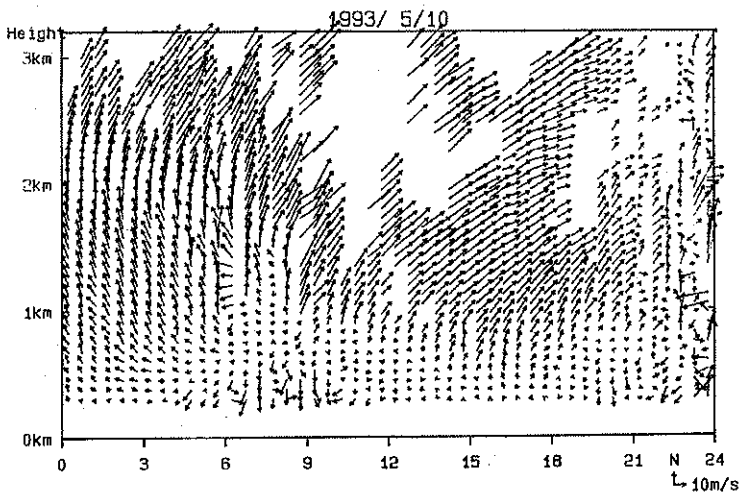

Figure 11.5: An example of wind measurement by a 1.3 GHz windprofiler radar. Each arrow represents the horizontal wind vector. The difference of winds in the boundary layer and free atmosphere is clearly shown.

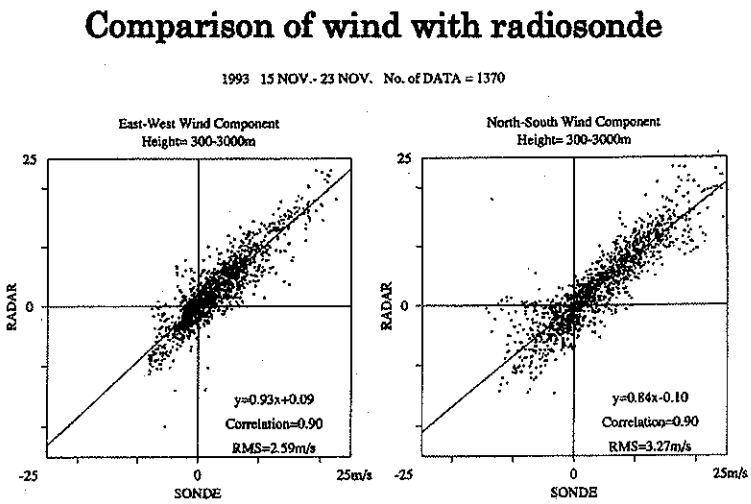

Figure 11.6: Comparisons of winds measured by a windprofiler radar and radiosondes. They show good agreements.

Result of CRL wind profiler observation (Typhoon 9512 approach)

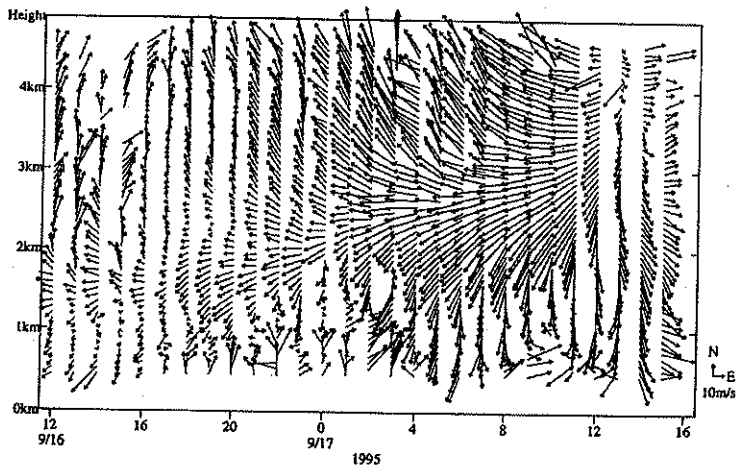

Figure 11.7: Another example of 1.3 GHz windprofiler radar in a typhoon event. A time change of very strong winds is shown.

(Passing of low pressure system)

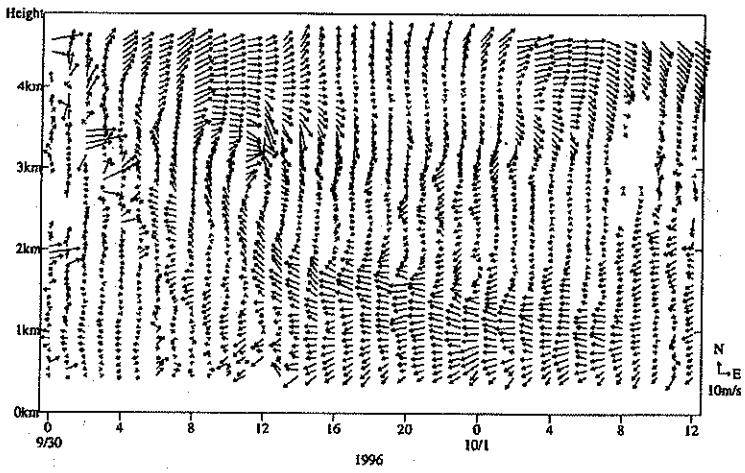

Figure 11.8: Other example of 1.3 GHz windprofiler radar wind measurement in a low pressure case.

Seasonal change of wind at Bangkok

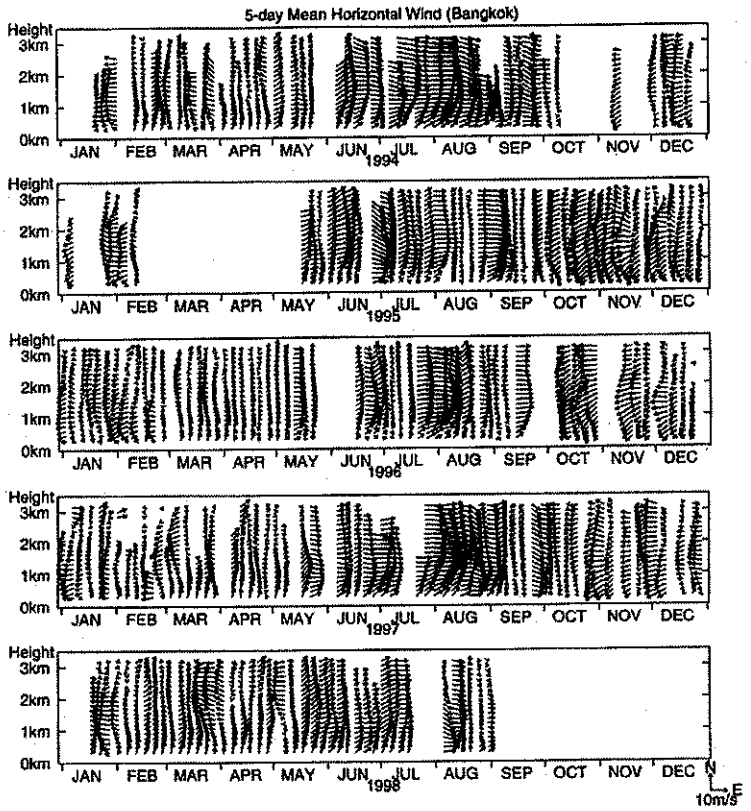

Figure 11.9: A result of a long-term wind observation in Thailand

Part III

Outline of the Trainining Course

Chapter 12

The Trainining Course in 1999

12.1 Remote Sensing

Recently, the environmental problems attracts strong attentions. The spatial scales of the problems range from very local one to global one. Environmental problems have close connection to atmospheric and hydrospheric phenomena. For the atmospheric and hydrospheric sciences, satellite remote sensing is very useful and essential because of its capability to observe the atmosphere and hydrosphere in a big scale. For example, recently launched TRMM (Tropical Rainfall Measuring Mission) is providing us a unique three-dimensional rain structures regardless of the location over tropical and a part of midlatitude regions. ADEOS (Advanced Earth Observing Satellite) gave us beautiful images of global phytoplankton distribution over global ocean.

Ground-based remote sensing which includes radars and lidars is also useful for the atmospheric observation.

The lectures give: the basic theory of remote sensing, technogy and applications, and current Earth observation satellites, etc.

12.2 Lectures

L. 1 Radar measurement of precipitation processes

Prof. K. Tsuboki
Institute for Hydrospheric-Atmospheric Sciences, Nagoya University

Multi-doppler radar observation is one of the powerful tools for proving the precipitation system. The technique and observation results will be introduced. Modelling efforts may also be included.

L. 2 Soil wetness measurement from satellite microwave remote sensing

Prof. T. Koike
Nagaoka University of Technology

Soil wetness is one of the key components in the land-atmosphere interaction. The soil wetness controls the water evaporation from land to atmosphere, and also runoff. Global soil wetness observation is a challenging target for the satellite remote sensing. The technique and observational results will be introduced.

L. 3 Observation of atmosphere by radar

Prof. K. Nakamura
Institute for Hydrospheric-Atmospheric Sciences, Nagoya University

Radar observation technology will be lectured. Radars include wind-profilers and rain/cloud radars. A recently launched satellite enabled us to have three dimensional rain structure over tropical region and a part of midlatitude region. The basic technology for spaceborne rain radar will also be included.

L. 4 Ocean color observation by satellite

Prof. T. Saino
Institute for Hydrospheric-Atmospheric Sciences, Nagoya University

Ocean color is a good index of the production of ocean. Satellite sensors, such as OCTS aboard ADEOS gave us a valuable data set. Sensors and recent results will be introduced.

L. 5 Active microwave measurement of rain and clouds from space

Dr. T. Kozu
Communications Research Laboratoy,
Ministry of Posts and Telecommunications

Active remote sensing of rain and clouds have a unique capability to give us the three dimensional structure. However, the sensor is heavy and complex. Current spaceborne radar technology and algorithms will be lectured.

L. 6 Lidar proving of the atmospher

Dr. T. Itabe
Communications Research Laboratoy,
Ministry of Posts and Telecommunications

A lidar is sensitive to small particles, such as cloud particles and aerosols in the atmosphere. Water vapor can also be profiled by lidar. The lidar technology and applications will be introduced. Spaceborne doppler lidar has a big potential for observation of wind in clear sky. The lidar technology will be lectured.

L. 7 Synthetic aperture radar and its applications

Dr. S. Uratsuka
Communications Research Laboratoy,
Ministry of Posts and Telecommunications

The lecture is on the synthetic aperture radar (SAR). SAR is famous for its excellent spatial resolution. Polarimeteric SAR provides much more information on land status. Recent interference technology added elevation detecting capability.

L. 8 Current remote sensing technology for global warming monitoring

Prof. H. Shimoda
Tokai University

Japan has a ADEOS series (ADEOS and ADEOS-II) for global warming monitoring. The current and future spaceborne sensors and technology for earth observation will be introduced.

L. 9 Global vegetation observation

Prof. Y. Honda
Chiba University

Global vegetation is, needless to say, important for mankind. It is sensitive to the climate change. The global monitoring of vegetation is invaluable. The basic technique and current results will be introduced.

12.3 Practical Training

The objective of the practical training is to give the trainees an idea what remote sensing data can give us and what procedure is required to produce result. The computer data processing is the main part of the training.

Each trainee will have his/her data and a PC, and he/she will be required to process the data. The sample data are by satellite-borne sensors and/or by airborne and ground-based radars. The training includes image production and correlation analysis. For example, the comparison among TRMM precipitation radar data and TRMM microwave radiometer data will be performed. The trainees are required to make reports.

12.4 Technical tours

The course also includes technical tours in the IHAS, Nagoya University, in the Communications Research Laboratory at Koganei, Tokyo, and in the Chiba University. There, the state of the art microwave remote sensing technology will be introduced.

12.5 Schedule 8-21 March, 1999

Mar. 8 (Monday): Arrival at Nagoya, Japan

Mar. 9 (Tuesday): Guidance, lectures and reception at IHAS, Nagoya Univ.

Mar. 10 (Wednesday): Lectures and technical tour in IHAS, Nagoya Univ.

Mar. 11 (Thursday): Lecture and guidance of data analysis training

Mar. 12 (Friday): Data analysis training

Mar. 13 (Saturday): Data analysis training (cont'ed)

Mar. 14 (Sunday): Move to CRL at Koganei, Tokyo

Mar. 15 (Monday): Technical Tour at CRL and lectures

Mar. 16 (Tuesday): Lectures

Mar. 17 (Wednesday): Move to Tokai Univ. and lectures. Move to Chiba Univ.

Chapter 12. The Trainining Course in 1999

Mar. 18 (Thursday): Lectures

Mar. 19 (Friday): Lectures and move to Nagoya

Mar. 20 (Saturday): Free day

Mar. 21 (Sunday): Departure from Nagoya

Chapter 13

Past Activities of the IHP Training Course

13.1 Past Activities of the IHP Training Course (1991–1998)

The IHP Training Course in Asia and the Pacific Region has been executed since 1991 by the Working Group for IHP Training Course, under the direction of the Sub-Committee for IHP, Japanese National Commission for UNESCO. The Training Course was aimed at giving the participants an opportunity to learn observation technology of hydrology and to have practical experience in hydrological observation in the field.

In the First to Sixth- sessions of the Training Course, the training began with two or three preliminary lectures to introduce the subjects to be studied throughout the remainder of the course schedule. After this introduction, students have been taken around to several specialized institutes, in the days following, to hear about what was actually done there, and to see modern instrumentation in general hydrology. It has been found, however, that this training approach possibly encourages passiveness on the part of the students because they spend an inordinate amount of time travelling daily to the host institutions where they can only listen and observe

rather than participate actively.

Some innovations, therefore, was made at Seventh- session, both in the educational content and in the schedule. Firstly, we decided to focus the training course on more clearly defined targets, and the first year's programme concentrated on Snow Hydrology. Secondly, we decided to include practice sessions such as a field programme to allow the students, themselves, the opportunity to carry out experiments and make relevant observations/analyses. Finally, we decided to prepare a newly edited textbook for the participants in the training course.

13.2 First to Sixth- sessions on General Hydrology (1991–1996)

13.2.1 T1. First IHP Training Course, 1991

T1.1. Participants

Ms. Zhao Ling (China): Student of the Special Program of Sciences of Atmosphere and Hydrosphere, Graduate School of Science, Nagoya University

Mr. Zhao Jing (China): ibid.

Ms. Hidajat Bernadia Irawati Tjandradewi (Indonesia): ibid.

Mr. Geng Biao (China): Student of Sciences of Atmosphere and Hydrosphere, Graduate School of Science, Nagoya University

Ms. Sri Mulat Yuningsih (Indonesia): The Research Institute for Water Resources Develop-ment, Department of Public Works

Mr. Roslan Bin Sahat (Malaysia): Hydrology Branch, Department of Drainage and Irrigation

T1.2. Schedule and Program

Opening lectures, held at Water Research Institute, Nagoya University, were given by the following specialists:

F. TAKAGI (Professor, Department of Civil Engineering, Faculty of Technology, Nagoya University): Runoff processes in river watersheds.

Y. FUJIYOSHI (Associate Professor, Laboratory of Atmospheric Environment, Water Research Institute, Nagoya University): Precipitation and water resources in Asia, part 1.

K. KATO (Assistant Professor, ibid.): ibid., part 1.

Y. ISHIZAKA (Associate Professor, Laboratory of Atmospheric Physics, ibid.): ibid., part 2.

Y. AGETA (Professor, Laboratory of Hydrospheric Physics, ibid.): ibid., part 3.

M. SAKAMOTO (Professor, Laboratory of Aquatic Ecology, ibid.): The matter cycle and water quality in the hydrosphere, part 1.

N. HANDA (Professor, Laboratory of Organic Geochemistry, ibid.): ibid., part 2.

K. OHTA (Associate Professor, ibid.): ibid., part 3.

The Training Course was presented from March 2 to 19, 1992 according to the following schedule:

Mar. 2–3: Water Res. Inst., Nagoya Univ. (Nagoya)

- Lecture on runoff processes in river watersheds.
- Lecture and Practice Session on precipitation and water resources in Asia.

- Lecture and Practice Session on the matter cycle and water quality in the hydrosphere.

Mar. 4–6: Chubu Regional Construction Bureau, Min. of Construction (Chubu Region)
Technical tour of hydrological facilities for river control.

Mar. 7- 8 (Sat-Sun): holidays

Mar. 9: Water Resources Res. Center, Disaster Prevention Res. Inst., Kyoto Univ.
Laboratory experiment on evaporation from bare soil.

Mar. 10: Kiryu Experimental Catchment, Faculty of Agriculture, Kyoto Univ.
Meteorological and hydrological observations at a small catchment in hilly terrain.

Mar. 11: (Kyoto to Tsukuba)

Mar. 12: Forestry & Forest Products Res. Inst., Min. of Agriculture, Forestry & Fisheries (Hitachi-Ohta)
Training on evaporation and soil moisture measurements, and hydrological observation.

Mar. 13: National Inst. for Environmental Studies, Environment Agency (Tsukuba)
Technical tour of research facilities for water quality conservation.

Mar. 14–15 (Sat-Sun): holidays

Mar. 16–17: Public Works Res. Inst., Min. of Construction (Tsukuba)
Lectures on hydrological observations and models of water discharge.

Mar. 18: Forecast Dept. & Observation Dept., Japan Meteorological Agency (Tokyo)

Lecture and technical tour concerning short-range precipitation forecasting using radar and the AMeDAS (automated meteorological data acquisition system).

Mar. 19: Meteorological Satellite Center, Japan Meteorological Agency (Kiyose)
Technical tour of Meteorological Satellite Center.

13.2.2 T2. Second IHP Training Course, 1992

T2.1. Participants

Ms. Thapa, Arati (Nepal): Student of Special Program of Sciences of Atmosphere and Hydrosphere, Graduate School of Science, Nagoya University

Mr. Kayastha, Rijan Bhakta (Nepal): ibid.

Mr. Sarwono, Pitoyo Sudibyo (Indonesia): ibid.

Mr. Le Cong Thanh (Vietnam): ibid.

Mr. Xu Guangxiang (China): ibid.

Mr. Adisak, Suriyavanagul (Thailand): Electricity Generating Authority

Mr. Pham Van Tan (Vietnam): Network Operation Department, Hydrometeorological Service

Mr. Ekanayaka M. Wimalasena (Sri Lanka): Investigation Section, National Water Supply and Drainage Board

Mr. S. Mahmoud Borghei (Iran): Assistant Professor, Department of Civil Engineering, Sharif University of Technology

T2.2. Schedule and Program

Opening lectures were given by the following personnel from the Water Research Institute, Nagoya University:

T. OHATA (Assistant Professor, Laboratory of Hydrospheric Physics): Precipitation and water resources in Asia, part 1.

K. KATO (Assistant Professor, Laboratory of Atmospheric Environments): ibid., part 2.

Y. ISHIZAKA (Associate Professor, Laboratory of Atmospheric Physics) ibid., part 3.

H. TERAI (Associate Professor, Laboratory of Aquatic Ecology): The material cycle and water quality in the hydrosphere.

The Training Course was presented from March 1 to 18, 1993 according to the following schedule.

Mar. 1–2: Water Res. Inst., Nagoya Univ. (Nagoya)

- Lecture and Practice Session on precipitation and water resources in Asia.
- Lecture and Practice Session on the matter cycle and water quality in the hydrosphere.

Technical tour.

Mar. 3–5: Kanto Regional Construction Bureau, Min. of Construction (Nagoya to Tokyo, Kanto Region)
Technical tour of hydrological facilities for river control.

Mar. 6–7 (Sat-Sun): holidays

Mar. 8–9: Environmental Res. Center, Univ. of Tsukuba (Tsukuba)
Observation and data analysis of evapotranspiration.

13.2. First to Sixth- sessions on General Hydrology (1991–1996)

Mar. 10–11: National Res. Inst. for Earth Science & Disaster Prevention, Science & Technology Agency (Tsukuba-Ichihara, Chiba)
Laboratory experiment of rainfall
Technical tour of an experimental hydrological catchment.

Mar. 12–14 (Fri–Sun): holidays

Mar. 15–16: National Res. Inst. of Agricultural Engineering, Min. of Agriculture, Forestry & Fisheries (Tsukuba)
Analysis of irrigation and drainage.
Study of experimental ground water facilities.

Mar. 17: Forecast Dept. & Observation Dept., Japan Meteorological Agency (Tokyo) Lecture and technical tour for short-range precipitation forecasting using radar and the AMeDAS.

Mar. 18: Meteorological Satellite Center, Japan Meteorological Agency (Kiyose) Technical tour of Meteorological Satellite Center.

13.2.3 T3. Third IHP Training Course, 1993

T3.1. Participants

Mr. Kamal, Md. Syeeduzzaman (Bangladesh): Student of the Special Program of Sciences of Atmosphere and Hydrosphere, Graduate School of Science, Nagoya University.

Ms. Sipayung, Sinta Berliana (Indonesia): ibid.

Ms. He Kaiqing (China): ibid.

Mr. Zhu Yan (China): Department of Hydrology, Hohai University

Mr. Wu Yongxiang (China): Nanjing Institute of Hydrology & Water Resources, Ministry of Water Resources

Ms. Suva, Imelda Manalastas (Philippines): Bureau of Research & Standards, Department of Public Works & Highways

Mr. Dwivedi, Ashok Kumar (India): Hydrological Investigations Division, National Institute of Hydrology, Roorkee

Mr. Ahmad, Bashir (Pakistan): Centre of Excellence in Water Resources Engineering, University of Engineering & Technology, Lahore

T3.2. Schedule and Program

Opening lectures were presented by the following specialists from the Institute for Hydrospheric-Atmospheric Sciences, Nagoya University:

K. KATO (Assistant Professor, Division of Water Cycle): Multi-scale cloud distributions in monsoon regions of Asia.

H. TANAKA (Professor, Division of Material Cycle): Cloud physics and chemistry in climate studies.

Y. AGETA (Professor, Division of Water Cycle): Asian cryosphere and changes in water resources.

M. NAKAWO (Associate Professor, Division of Water Cycle): Water cycle and stable isotopes.

The Training Course was presented from August 16 to September 2, 1993 according to the following schedule:

Aug. 16–17: Inst. for Hydrospheric-Atmospheric Sci., Nagoya Univ. (Nagoya)

- Lectures on the International Hydrological Programme.
- Lecture and Practice Session on precipitation and water resources in Asia.
- Lecture and Practice Session on the matter cycle and water quality in the hydrosphere.

13.2. First to Sixth- sessions on General Hydrology (1991–1996)

Aug. 18–20: Chubu Regional Construction Bureau, Min. of Construction (Chubu Region)
Technical tour of hydrological facilities for river control.

Aug. 21–22 (Sat–Sun): holidays

Aug. 23: Water Resources Res. Center, Disaster Prevention Res. Inst., Kyoto Univ.
Lecture on control of run-off water.

Aug. 24: Kiryu Experimental Catchment, Faculty of Agriculture, Kyoto Univ.
Meteorological and hydrological observations at a small catchment in hilly terrain.

Aug. 25: (Kyoto to Tsukuba)

Aug. 26: Forestry & Forest Products Res. Inst., Min. of Agriculture, Forestry & Fisheries (Hitachi-Ohta)
Training on evaporation and soil moisture measurements, and hydrological observation.

Aug. 27: Public Works Res. Inst., Min. of Construction (Tsukuba)
Lectures on hydrological observations and models of water discharge.

Aug. 28–29 (Sat–Sun): holidays

Aug. 30: Public Works Res. Inst., Min. of Construction (Tsukuba)
Lectures on hydrological observations and models of water discharge.

Aug. 31: National Inst. for Environmental Studies, Environment Agency (Tsukuba)
Technical tour of research facilities for water quality conservation.

Sep. 1: Meteorological Satellite Center, Japan Meteorological Agency (Kiyose)
Technical tour of Meteorological Satellite Center.

Sep. 2: Forecast Dept. & Observation Dept., Japan Meteorological Agency (Tokyo)
Lecture and technical tour concerning short-range precipitation forecasting using radar and the AMeDAS.

13.2.4 T4. Fourth IHP Training Course, 1994

T4.1. Participants

Mr. Sunil Adhikary (Nepal): Student of the Special Program of Sciences of Atmosphere and Hydrosphere, Graduate School of Science, Nagoya University

Mr. Zhang Wan Chang (China): ibid.

Mr. Mohammad Rezwanul Islam (Bangladesh): ibid.

Mr. Birbal Rana (Nepal): Student of Sciences of Atmosphere and Hydrosphere, Graduate School of Science, Nagoya University

Ms. Y.K. Handapangoda (Sri Lanka): Teaching Assistant in Civil Engineering, University of Peradeniya, Peradeniya

Ms. Byambaagiin Oyunchimeg (Mongolia): Ministry of Nature and Environment, Institute of Water Problems, Ulaan Baatar

Mr. M. Fakhruddin (Indonesia): Puslitbang Limnology, LIPI, Bogor

Ms. Gadis Sri Haryani Bengen (Indonesia): Research and Development Center for Limnology, Indonesian Institute of Sciences, Bogor

T4.2. Schedule and Program

Opening talks were presented by the following lecturers from the Institute for Hydrospheric-Atmospheric Sciences, Nagoya University:

K. KATO (Assistant Professor, Division of Water Cycle): Asian monsoon and water cycle.

13.2. First to Sixth- sessions on General Hydrology (1991–1996)

N. HANDA (Professor, Division of Material Cycle): Carbon cycling with water cycle.

H. TERAI (Associate Professor, Division of Material Cycle) Aquatic micro-organisms and water quality.

The Training Course was presented from August 15 to September 1, 1994 according to the following schedule:

Aug. 15–16: Inst. Hydrospheric-Atmospheric Sci., Nagoya Univ. (Nagoya)

- Lecture on the International Hydrological Programme.
- Lecture and Practice Session on precipitation and water resources in Asia.
- Lecture and Practice Session on the biogeochemical cycle and water quality in the hydrosphere.

Aug. 17–19: Kanto Regional Construction Bureau, Min. of Construction (Nagoya to Tokyo, Kanto Region)
Technical tour of hydrological facilities for river control.

Aug. 20–21 (Sat–Sun): holidays

Aug. 22–23: Environmental Res. Center, Univ. of Tsukuba (Tsukuba)
Observation and data analysis of evapotranspiration.

Aug. 24–25: National Res. Inst. of Agricultural Engineering, Min. of Agriculture, Forestry & Fisheries (Tsukuba)
Analysis of irrigation and drainage.
Study of experimental facilities for ground water.

Aug. 26: National Inst. for Environmental Studies, Environment Agency (Tsukuba)
Technical tour of research facilities for water quality conservation.

Aug. 27–28 (Sat–Sun): holidays

Aug. 29–30: National Res. Inst. for Earth Science & Disaster Prevention, Science & Technology Agency (Tsukuba-Chiba Pref.)
Large scale rainfall experiment.
Technical tour of an experimental hydrological catchment.

Aug. 31: Forecast Dept. & Observation Dept., Japan Meteorological Agency (Tokyo)
Lecture and technical tour concerning short-range precipitation forecasting using radar and the AMeDAS.

Sep. 1: Meteorological Satellite Center, Japan Meteorological Agency (Kiyose)
Technical tour of Meteorological Satellite Center.

13.2.5 T5. Fifth IHP Training Course, 1995

T5.1. Participants

Ms. Meng Xiao (China): Student of the Special Program of Sciences of Atmosphere and Hydrosphere, Graduate School of Sciences, Nagoya University

Mr. Talukder Abul Bashar MD. Alauddin (Bangladesh): ibid.

Mr. Liu Jing Shi (China): ibid.

Mr. Begkhutod Perapol (Thailand): ibid.

Mr. Bhatt Maya Prakash (Nepal): ibid.

Mr. Ma Xieyao (China): Student of Sciences of Atmosphere and Hydrosphere, Graduate School of Science, Nagoya University

13.2. First to Sixth- sessions on General Hydrology (1991–1996)

T5.2. Schedule and Program

The Training Course was presented in three parts according to the following schedule: Part 1 from December 13 to 15, 1995, Part 2 from February 13 to 16, 1996, and Part 3 from March 11 to 15, 1996.

Part 1: Chubu Region

Dec. 13–15: Chubu Regional Construction Bureau, Min. of Construction (Aichi and Gifu)
Technical tour of hydrological facilities for river control.

Part 2: Kinki Region

Feb. 13: Lake Biwa Res. Inst., Shiga Pref. (Otsu)
Lecture and technical tour for Lake Biwa.

Feb. 14: Branch Office of Kinki District of Public Works, Min. of Construction (Otsu)
Lecture and technical tour for mountain conservation.
Dept. of Forestry, Kyoto Univ. (Otsu)
Lecture and technical tour of an experimental basin.

Feb. 15: Disaster Prevention Res. Inst., Kyoto Univ. (Uji)
Lecture and technical tour on disaster prevention.
Hirakata Operation Center, Min. of Construction (Hirakata)
Lecture on river water control.

Feb. 16: Section of River Management, Kyoto Pref. (Kyoto)
Technical tour concerning river management.

Part 3: Kanto Region

Mar. 11: Inst. for Forestry and Forest Products, Min. of Agriculture, Forestry and Fisheries (Hitachi-Ohta)
Training on evaporation and soil moisture measurement, and on making hydrological observation.

Mar. 12: National Inst. for Environmental Studies, Environment Agency, (Tsukuba)
Technical tour of research facilities for water quality conservation.

Mar. 13: Public Works Res. Inst., Min. of Construction (Tsukuba)
Lecture on hydrological observation and models of water discharge.

Mar. 14: Forecast Dept. & Observation Dept., Japan Meteorological Agency (Tokyo)
Lecture and technical tour concerning short-range precipitation forecasting using radar and the AMeDAS.

Mar. 15: Meteorological Satellite Center, Japan Meteorological Agency (Kiyose)
Technical tour of Meteorological Satellite Center.

13.2.6 T6. Sixth IHP Training Course, 1996

T6.1. Participants

Mr. Zulkefle bin Ghazali (Malaysia): Hydrology Division, Department of Irrigation and Drainage

Mr. Rhoel C. Villa (Philippines): National Hydraulic Research Center, U.P. College of Engineering

Mr. Luong Tuan Anh (Vietnam): Institute of Meteorology and Hydrology, Hanoi Hydrometeorological Service of Vietnam

Mr. Atthaporn Buddhapolit (Thailand): Hydrology Division, Royal Irrigation Department

Ms. Rungkarn Krishnamra (Thailand): Soil and Water Conservation Division, Land Development Department

T6.2. Schedule and Program

Opening lectures were presented at the Institute for Hydrospheric-Atmospheric Sciences, Nagoya University by the following lecturers:

K. KURAJI (Professor, University of Tokyo): Hydrological characteristics of tropical forests.

K. NAKAMURA (Professor, Institute for Hydrospheric-Atmospheric Sciences, Nagoya University): Remote sensing from space.

Y. TACHIKAWA (Professor, Kyoto University): Development of distributed rainfall-runoff model by using digital elevation models.

K. TAKEUCHI (Yamanashi University): The new thrust of IHP activities in Southeast Asia and Pacific, Asian/Pacific FRIEND (Flow Regimes from International Experimental and Network Data).

The Training Course was presented from August 19 to September 5, 1996 according to the following schedule:

Aug. 19–20: Inst. for Hydrospheric-Atmospheric Sciences, Nagoya Univ. (Nagoya)

- Lecture on International Hydrological Programme.
- Lecture concerning forest effects on the hydrological cycle in tropical regions.
- Lecture on precipitation measurement by remote sensing.
- Lecture on hydrological modelling.
- Lecture on Asian FRIEND.

Aug. 21–23: Kanto Regional Construction Bureau, Min. of Construction (Kanto Region) Technical tour of hydrological facilities for river control.

Aug. 24–25 (Sat–Sun): holidays

Aug. 26–27: Environmental Research Center, Tsukuba Univ. (Tsukuba)
Lecture and Practice Session on evapotranspiration measurements.
Lecture on the role of the biosphere for climate systems.

Aug. 28–29: National Res. Inst. of Agricultural Engineering, Min. of Agriculture, Forestry & Fisheries (Tsukuba)
Analysis of irrigation and drainage.
Technical tour to an irrigated paddy field.

Aug. 30: Public Works Res. Inst., Min. of Construction (Tsukuba)
Technical tour of research facilities for water quality conservation.

Aug. 31–Sep. 1 (Sat–Sun): holidays

Sep. 2- 3: National Res. Inst. for Earth Science & Disaster Prevention, Environment Agency (Chiba Pref.)
Large-scale rainfall experiment.
Technical tour to the hydrological catchment basin.

Sep. 4: Forecast Dept. & Observation Dept., Japan Meteorological Agency (Tokyo)
Lecture and technical tour concerning short-range precipitation forecasting using radar and the AMeDAS.

Sep. 5: Meteorological Satellite Center, Japan Meteorological Agency (Kiyose)
Technical tour of Meteorological Satellite Center.

13.3 T7. Seventh IHP Training Course, 1998: Snow Hydrology

Outline of the 7th IHP Training Course on Snow Hydrology Objectives The general aim of the IHP short course is to help participants develop their basic knowledge of hydrological systems and of their sensitivity to climate changes as well as to contribute to solving current global environmental problems. The cryosphere is most vulnerable to the projected global warming trend that has recently become a major concern in many countries. The seventh training course focuses on snow hydrology. The topics covered range from basic knowledge of the role of the cryosphere in the global environment to technical applications, including observations and measurements in snow packs.

13.3.1 T7.1. Participants

D. B. Chettri, Executive Engineer, Meteorology Unit, Div. Power, Ministry of Trade and Industry, Bhutan

Liang, Zhongmin, Teacher, Dept. Hydrology, Hohai University, China

Om Ratna Bajracharya, Senior Hydrologist, Dept. Hydrology and Meteorology, Ministry of Science and Technology, Nepal

Shiva Bhakta Prajapati, Hydrologist, Dept. Hydrology and Meteorology, Ministry of Science and Technology, Nepal

Aurangzeb Khattak, Assistant Director, WRRC, Pakistan

Edvin Aldrian, M2, IHP Student, IHAS Nagoya University, Indonesia

Dang Xuan Phong, M2, IHP Student, IHAS Nagoya University, Vietnam

Li, Jianjun, M2, IHP Student, IHAS Nagoya University, China

Yudi Iman Tauhid, M2, IHP Student, IHAS Nagoya University, Indonesia

Bhuwan Chandra Bhatt, M1, IHP Student, IHAS Nagoya University, Nepal

Zhou Shiqiao, M1, IHP Student, IHAS Nagoya University, China

Kayastha Rijan Bhakta, Research Fellow, IHAS, Nepal

Suresh Chandra Pradhan, Hydrological Assistant, Dept. Hydrology and Meteorology, Ministry of Science and Technology, Nepal

Keshav Raj Sharma, Hydrological Assistant, Dept. Hydrology and Meteorology, Ministry of Science and Technology, Nepal

Chok Bahadur Gurung, Hydrological Assistant, Dept. Hydrology and Meteorology, Ministry of Science and Technology, Nepal

Dorji Wangdu, Head, Division of Geology and Mines, Bhutan

Diraagiin Erdenetsetseg, Expert, Centre for Climate and Environmental Change, Institute of Meteorology and Hydrology, Mongolia

Nozomu Naito D3, Graduate Student, IHAS Nagoya University, Japan

Fumio Nakazawa, Japan

Yosihiro Yoshioka M2, Graduate Student, Nagaoka University of Technology, Japan

13.3.2 T7.2. Schedule and Program

Lecturers

Y. Ageta (Institute for Hydrospheric-Atmospheric Sciences, Nagoya University)

T. Aoki (Meteorological Research Institute)

K. Goto-Azuma (Nagaoka Institute of Snow and Ice Studies, National Research Institute for Earth Science and Disaster Prevention)

N. Hayakawa (Department of Civil and Environmental Engineering, Nagaoka University of Technology)

H. Iida (Sediment Control Division, Department of Civil Engineering, Toyama Prefectural Government)

I. Kamiishi (Centre of Snow and Ice Technology, ARGOS Co. Ltd.)

S. Kobayashi (Research Institute for Hazards in Snowy Areas, Niigata University)

M. Lu (Department of Civil and Environmental Engineering, Nagaoka University of Technology)

H. Mizuno (Meteorological College)

M. Nakawo (Institute for Hydrospheric-Atmospheric Sciences, Nagoya University)

H. Ohno (Japan International Research Centre for Agricultural Sciences)

K. Satow (Civil Engineering, Nagaoka National College of Technology)

T. Takeda (Institute for Hydrospheric-Atmospheric Sciences, Nagoya University)

Y. Takeuchi (Nagaoka Institute of Snow and Ice Studies, National Research Institute for Earth Sciences and Disaster Prevention)

K. Yokoyama (Hokuriku National Agricultural Experiment Station)

Schedule (9 March, 1998 – 22 March, 1998)

Mar. 9 (Monday): Arrival at Nagoya, Japan

Mar. 10 (Tuesday): Guidance
Lecture on Glaciers and the water cycle
Lecture on precipitation process
Lecture on synoptic conditions and snow fall precipitation process
Icebreaker reception in the evening

Mar. 11 (Wednesday): Technical Tour (IHAS, Nagoya University) Move from Nagoya to Myoko (4 hour's train ride)

Mar. 12 (Thursday): Lecture on water circulation over the earth: the roles of snow and ice
Radiation processes and remote sensing of snow
Practice session for spectral albedo observations on a snowfield

Mar. 13 (Friday) Lecture on snowmelt hydrology
Practice session for Hydrographical Observations
Fabrication of the Endo-type snow-water content meter (1)

Mar. 14 (Saturday): Lecture on metamorphism of deposited snow
Lecture on snow changes in snow pack and melt water chemistry during snowmelt
Lecture on heat budget of a snow pack

Mar. 15 (Sunday): Technical bus tour to
• Niigata Experiment Laboratory, Public Works Research Institute
• Tohkamachi Experiment Station, Forestry and Forest Products Research Institute
• Nagaoka Institute of Snow and Ice Studies, National Research Institute for Earth Science and Disaster Prevention
(Stay overnight at a Spa, Yomogihira Hot Spring, in the snowy region)

Mar. 16 (Monday): Technical bus tour continues to

- Myoken Weir, Shinano River
- Facilities for snow removal by melting in Nagaoka City

- Shinano River Work Office, Hokuriku Regional Construction Bureau
- Oukouzu Division Work, Shinano River and the Division Work Museum
- Arai Weir, Shinano River

Fabrication of the Endo-type snow-water content meter (2)

Mar. 17 (Tuesday): Practice session for heat exchange over a snow surface

Mar. 18 (Wednesday): Practice session for snow pit observations

Mar. 19 (Thursday): Data handling exercise (reception in the evening)

Mar. 20 (Friday): Report preparation
Move from Myoko to Nagoya (train ride)

Mar. 21 (Saturday): Closing ceremony

Mar. 22 (Sunday): Departure from Nagoya